Università degli Studi di Palermo

Dottorato di Ricerca in Ingegneria Civile, Ambientale, dei Materiali
Dipartimento di Ingegneria Civile, Ambientale, Aerospaziale, dei Materiali
Settore Scientifico Disciplinare ICAR/08 - Scienza delle Costruzioni

Nonlinear Analysis of Reinforced Concrete Frames: Safety Evaluation and Retrofitting Techniques

Il Dottore
Mohsen Rezaee Hajidehi

Il Coordinatore
Prof. Mario Di Paola

Il Tutor
Prof. Giuseppe Giambanco

Il Co-Tutor
Prof. Stanislaw Stupkiewicz

CICLO XXX
Anno 2018

Mohsen Rezae Hajidehi
Palermo, Febbraio 2018
e-mail:mohsen.rezaeehajidehi@unipa.it
e-mail:mohsen.rock2003@gmail.com
Thesis of the Ph.D. course in *Civil, Environmental, Materials Engineering - Structural and Geotechnical Engineering*
(Ingegneria Civile, Ambientale, dei Materiali - Ingegneria Strutturale e Geotecnica)
Dipartimento di Ingegneria Civile Ambientale, Aerospaziale, dei Materiali
Università degli Studi di Palermo
Scuola Politecnica
Viale delle Scienze, Ed.8 - 90128 Palermo, ITALY
Written in LaTeX
Examples and figures are made by *MATLAB*©, *Mathematica*© *Inkscape*©

Fairness, justice and freedom are more than words, they are perspectives.[1]

[1] Hill, G. (Producer), & McTeigue, J. (Director). (2005). V for Vendetta [Motion Picture]. United Kingdom: Warner Bros.

Contents

List of Figures

List of Tables

Chapter 1

Introduction

1.1 General

Reinforced Concrete (RC) is one of the most commonly used materials for constructions. It has numerous advantages including great compressive strength, suitable rigidity, relative low cost, long service life, and high design flexibility.

A considerable number of existing RC buildings worldwide do not possess sufficient seismic performance, and are prone to serious structural damages. This is particularly evident for those cases where seismic-resistant regulations were not promulgated at the time of construction and, consequently, the buildings were designed and constructed by merely taking into account the vertical dead and live loads (gravity-designed buildings). As a result of this deficiency, under the combination of vertical and horizontal actions, progressive damage occurs in structural elements and thus the stability of the structure is affected, which may lead to structural failure.

The consequences of structural damages range from direct and indirect losses due to repair and disruption of business to social and environmental impacts such as injuries, fatalities, homelessness, and release of hazardous materials, among others [67]. In addition, in many cases these constructions represent an important economic and social patrimony.

To prevent irreversible losses, the existing structures should be opportunely strengthened in order to absorb the expected seismic energies. As a preliminary step before the rehabilitation process, the potential weak areas in the target structure should be identified. Nonlinear analysis is a promising tool that provides insight into the structural performance and reliability, and also the damage distribution in the structural elements. The technique is performed

with the aim to determine the critical points and the degree of deterioration of the structure so that an appropriate rehabilitation strategy can be selected.

Nonlinear static pushover analysis is a quite widespread computational tool that provides an accurate estimation of the seismic demands and capacities of structures. It can be programmed on the basis of concentrated plasticity or distributed plasticity concept. Distributed plasticity models, although more accurate with respect to the concentrated ones, require large computational effort and time. For this reason, many commercial finite element programs are developed in the framework of concentrated plasticity. Concentrated plasticity models, on the other hand, require a predefined knowledge on the position of the plastic sections. Otherwise, they consider the plastic sections at the extreme segments of the structural elements. In the former case, predicting in advance the exact positions of the plastic sections is usually not possible and if inaccurately done, can lead to unreliable and erroneous responses. In the latter case, it is not possible to locate a plastic section along the element span, and thus the suspected element is automatically divided into two segments with a necessary re-meshing procedure, which increases the computational cost.

1.2 Objectives

Considering the aforementioned problems, the main focus of the thesis is devoted to the development of a Finite Element Method (FEM) tool for nonlinear static pushover analysis of RC structures in the framework of concentrated plasticity. With respect to other strategies, the proposed approach overcomes the mesh refinement problem and enables the formation of plastic hinges at any position of the element.

Using this numerical tool, it is also possible to determine the effectiveness and reliability of different retrofitting techniques, which is the second main objective of this thesis. Special attention is given to Fiber Reinforced Polymer (FRP) composites and Shape Memory Alloy (SMA) retrofitting techniques.

1.3 Structure of the Thesis

This thesis is split into five parts. In the first part (Chapter 2), different structural analysis methods and the relevant finite element strategies are introduced. A literature review regarding the static pushover analysis technique and the existing distributed and concentrated plasticity models is presented.

In the second part (Chapter 3), which is the main part of this thesis, the proposed FEM procedure is described, beginning with the theoretical background through the FEM implementation and arriving to numerical applications.

The third part (Chapter 4) deals with the application of FRP composites for retrofitting deficient RC structures. For this purpose, the proposed FEM procedure is modified to account the presence of FRP composites in RC sections.

The forth part (Chapter 5) begins with the introduction of a robust constitutive model for SMA. Then, the model is empowered with a micromorphic term in order to simulate the true behaviour of SMA in tension. Afterwards, the very first model is introduced into the presented FEM procedure to investigate the behaviour of RC structures retrofitted by SMA braces.

In the conclusion part (Chapter 6), the main findings of the thesis is summarized and further developments are indicated.

Chapter 2

State of Art

2.1 Introduction

In order to analyse the structural behaviour of framed structures, different procedures can be implemented based on the demanded accuracy of the responses. Based on the inclusion of nonlinear effects, these procedures are categorized into linear and nonlinear approches. Each of the two categories are then classified into static and dynamic methods (see Fig. 2.1). The desicion of selecting one method over the others lies on specific assumptions that can be considered for a particular structure, thus each of the four methods can be applied for specific engineering or research purposes. A detailed discussion through the features and applications of different structural analysis methods is beyond the scope of this thesis (the reader may refer to e.g. [55, 177]), which is devoted to the nonlinear static analysis method only.

Experimental observations have demonstrated that the behaviour of structural materials as steel and concrete is associated with significant nonlinearity. This, in fact, compels the structural engineers and researchers to carry out nonlinear-type analysis to acquire more reliable and precise results. Nonlinear time-history analysis is a promising tool that provides an accurate simulation of the structural responses under specified ground motion records. The analysis is computationally expensive due to the large number of time steps in the applied ground motions. For this, generally, it is recommended that the use of the nonlinear time-history analysis should be limited to the structures in which the effect of higher modes can be important, e.g. in irregular and tall buildings. As an alternative solution, nonlinear static analysis (pushover) is used to predict the structural performance in a simplified manner with acceptable precision.

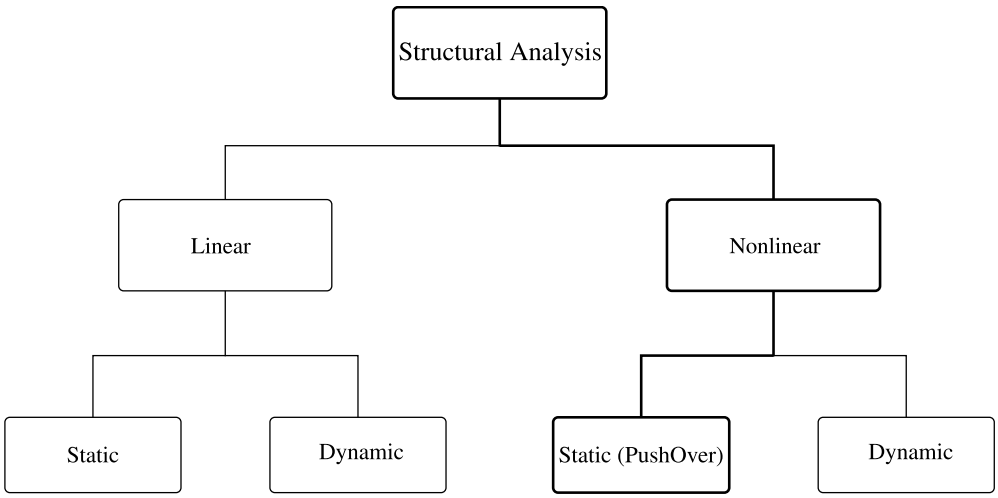

Figure 2.1: Different approaches for the structural analysis of the framed structures.

In general, nonlinear analysis of structures can be performed with different scales of accuracy and complexity. The scale of analysis is determined by the size and the geometry of the model (e.g. a full-scale structure, a structural element or a structural joint), and also the precision of the desired response. Discrete finite elements model is one of the most common and widely-reported methods of modelling in which the structural model is divided into a finite number of interconnected frame elements. Within the scope of finite element discretization, the frame elements are formulated either based on the *displacement* (stiffness) *approach* or *force* (flexibility) *approach*. In the displacement-based approach, the displacement field is assumed as the primary variable, see Fig. 2.2(a), and the displacement shape functions are constructed in order to evaluate the displacements along the element. Subsequently, stiffness matrix and force vector are derived, e.g. using the principle of virtual displacement, and accordingly internal forces and strains are calculated. On the other hand, in the force-based formulation the force-field is at the beginning assumed as unknown, see Fig. 2.2 (b), and internal forces are related to the nodal forces via suitable shape functions by which the equilibrium condition is fulfilled even in the plastic range [163]. The pertinent properties of the displacement-based and force-based elements are demonstrated by Neuenhofer and Filippou through an interesting comparative study [128].

To carry out a pushover analysis in the framework of finite element, two

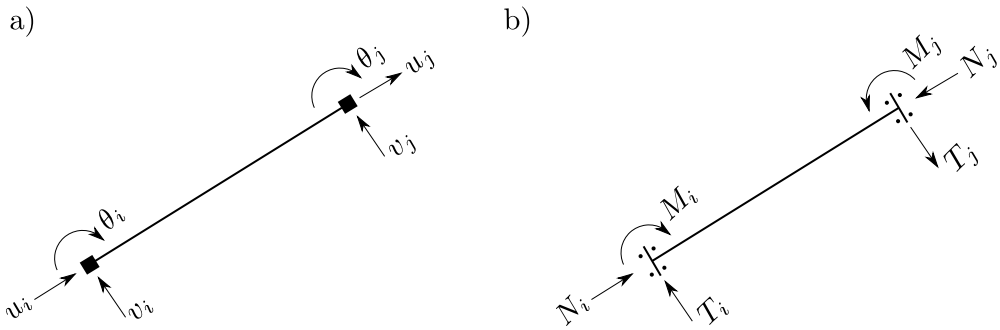

Figure 2.2: Displacement-based element (a) and force-based element (b) showing, respectively, deformation field and force field as the primary unknowns of the problem.

modelling strategies are available for the nonlinear analysis of beam-column elements, namely *distributed plasticity* and *concentrated plasticity*. Distributed plasticity assumes the spread of plasticity along the length of the beam-column element, which is undoubtedly realistic and represents the true nonlinear behaviour of the structural elements. In this strategy, in practice, the behaviour of beam-column elements is obtained by merely monitoring representative sections that are located on the integration points [172], or in a more precise fashion, permitting the localization of plasticity at each point of an element and discretisizing the cross-section in finite regions, each one with its own constitutive characteristics (fiber model). Distributed plasticity models are written following a stiffness or a flexibility method depending if their formulation is displacement-based or force-based, respectively. Concentrated plasticity (lumped plasticity), on the other hand, is based on the assumption that the plasticity is formed at the extremities of beam-column elements while the rest remains elastic. In this context, the plasticity is lumped into zero-length sections for which the mechanical properties are idealized by means of nonlinear rotational springs. Figure 2.3 schematically illustrates the concentrated and distributed plasticity based elements. It should be noted that in the case of concentrated plasticity, the literature is larger and more expansive thanks to the basic advantages of the concentrated plasticity strategy with respect to the distributed plasticity, e.g. simplicity, reduced storage requirement and time of computation.

The main goal of the present thesis is the development of an efficient numerical tool based on lumped plasticity elements to run nonlinear analyses on RC structures in order to simulate the nonlinear behaviour of such structures. This

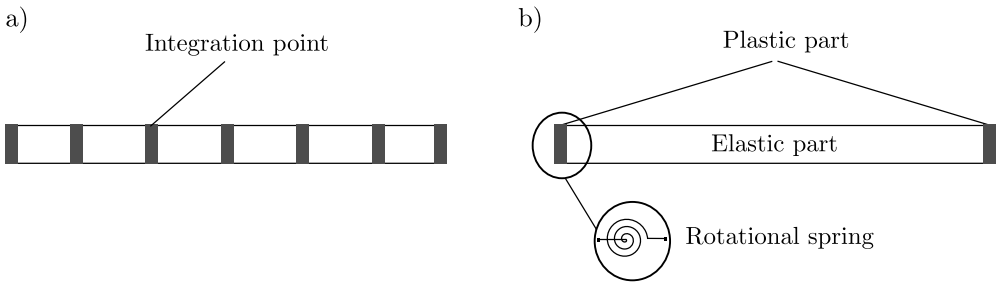

Figure 2.3: Schematic representation of distributed plasticity (a) and concentrated plasticity (b) in the element.

instrument could be therefore exploited to solve part of the nonlinear structural analysis methods, mainly the most diffused static one.

The aim of this Chapter is to provide a brief literature review on the development and applications of pushover analysis (Section 2.2) and also on the implementation of finite element modelling strategies (Section 2.3). Finally, conclusion remarks are discussed in Section 2.4.

2.2 A Literature Survey on the Pushover Analysis

Among the two nonlinear analysis procedures available, pushover analysis has received the majority of attentions due to its simplicity with respect to its dynamic counterpart. It offers information on the limit load, the location of plastic sections, displacement capacity and member ductilities. The procedure consists of applying a progressively increasing set of lateral loads in different steps. In each step, the stiffness matrix is updated and the static equilibrium condition of the structure is imposed. The procedure continues until the formation of a collapse mechanism or achievement of a predetermined displacement [139]. At the end of the procedure, the result is given in the form of a capacity curve, which is the plot of the base-shear of the structure versus the displacement of a control point, which is generally the mass centroid of the highest floor, see Fig. 2.4.

Many studies have been conducted on different scales to show the application of pushover analysis in determining the overall capacity of the structure, the acceptable accuracy of the procedure compared to experimental studies and dynamic analyses, its approximations as well as limitations. Here, the fo-

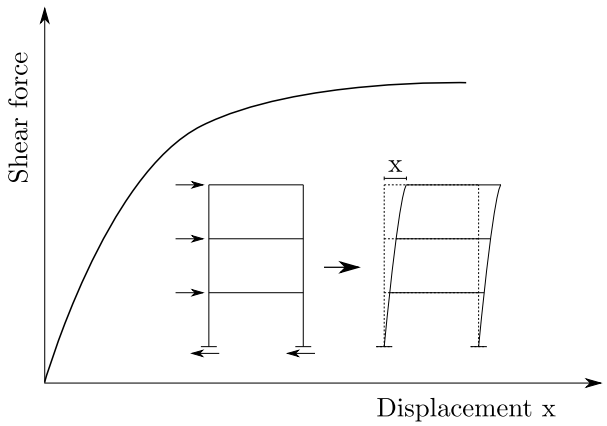

Figure 2.4: The illustration of the capacity curve obtained from pushover analysis.

cus is not to provide an exhaustive review on the pushover analysis procedure. It is rather intended to remark some influential studies and illustrating some applications.

The early developments of the pushover analysis have been reviewed by Elnashai [58]. The accuracy of the pushover analysis is an important aspect that should be properly investigated. Bagheri et al. [15] concluded that the static pushover analysis is not suitable for the evaluation of high-rise buildings and thus the use of dynamic analysis is essential. On the other hand, according to the results of Mwafy and Elnashai [127], the deficiencies of the pushover analysis with respect to the dynamic analysis can be compensated by selecting multiple load patterns. Very recently, a study was performed by Li et al. [106] to assess the applicability of the pushover analysis method. In this study, pushover analysis with three different types of lateral load distribution, namely inverted triangle, uniform and adaptive, in which the distribution of the lateral load changes according to the distribution of the inertia force at any step of the analysis, are implemented and a three-story RC frame was selected as the case study. A shaking table test was conducted and the experimental results were used as a reference to validate the results of pushover and time-history analyses. It was observed by the authors that the accuracy of the pushover analysis is adequate for mid-rise ductile RC frames. However, it was pointed out that the error of the pushover analysis increases as the structural damage evolves in the frame. In Fig. 2.5, the accuracy of adopted analysis methods in the calculation of the top displacement is compared with the ones of the

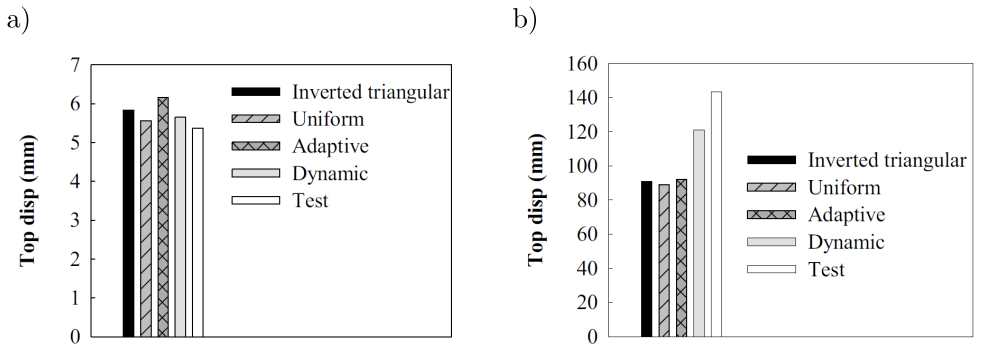

Figure 2.5: Comparison of the top displacements in the study of Li et al. [106] for the structure with no accumulated damage (a) and the structure with sever accumulated damage (b).

shaking table test.

Krawinkler and Seneviratna [91] have discussed the principles of the pushover analysis followed by an identification of the cases where the pushover analysis is satisfactory and the cases where an additional corroboration is needed. Two main outcomes are mentioned by the authors. It was demonstrated, through a pushover analysis on a four-story steel frame structure under nine ground motion records, that for low-rise frame structures, i.e. structures with insignificant higher mode effects, the pushover analysis provides adequate information towards the structural performance. On the other hand, the second outcome articulates that for high-rise buildings, the results of pushover analysis may be imprecise. This is stemmed by investigating a twenty-story structure and a multi-story wall structure that, respectively, demonstrate the underestimation of the maximum story drift and the maximum base shear by pushover analysis. It is clearly stated that the pushover analysis can be performed for the evaluation of all structures; however, for the structures where the higher modes are prone to be dominant, the pushover analysis should be complemented with another sophisticated analysis procedure, e.g. the time-history analysis [91].

An adaptive pushover analysis method was established by Bracci et al. [26]. The method was used to evaluate the response of a 1:3 gravity-designed RC structure before and after the retrofitting procedure, which was performed by means of concrete jacketing of the interior columns. The incremental story shear demands is considered for the derivation of the most suitable lateral load distribution pattern. Experimental results showed that by applying the lateral

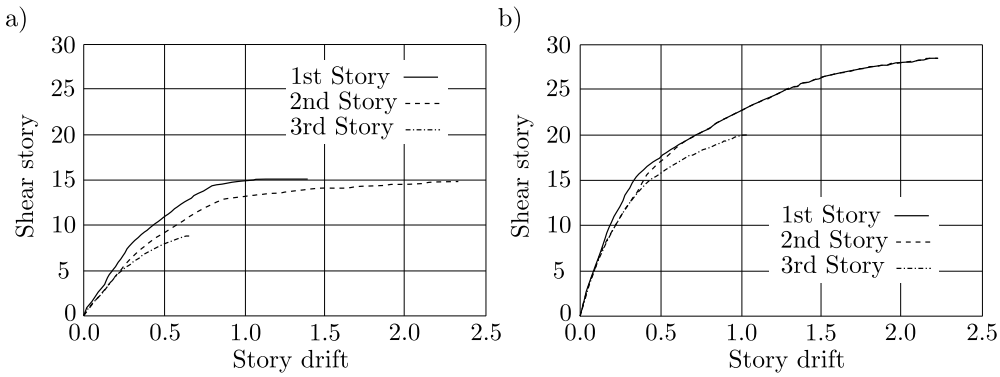

Figure 2.6: The capacity curves of the original model (a) and the retrofitted model (b) in the study of Bracci et al. [26].

load distribution pattern obtained from the adaptive pushover analysis, more consistent responses with respect to the experimental one is provided. Besides, the adaptive pushover analysis successfully predicted the nonductile mechanism of the frame as well as the effect of retrofitting technique. Figure 2.6 depicts the capacity curves of the original and retrofitted models given by the adaptive pushover method.

In the displacement-based framework, Borzi et al. [23] proposed a simplified approach for the pushover analysis of RC structures. The proposed approach assumes an elastic-perfectly-plastic behaviour for the structure. To this end, the capacity curve is defined as a function of the collapse multiplier and the displacement capacity. The displacement points in the pushover curve are then linked to the levels of structural damage, namely light damage, significant damage and collapse (Fig. 2.7). The method is then employed to simulate the behaviour of poorly designed RC structures by considering different collapse mechanisms. To validate the proposed method, a six-story gravity-designed RC structure was evaluated by an FEM program and the results are compared with the results of the proposed method (Fig. 2.8).

The static pushover analysis procedure is extensively used to investigate the effectiveness of different retrofitting techniques of structures. A typical study concerns the effect of different types of infillments on the global capacity and response of RC frames. Particularly, the use of different materials (i.e. hollow clay or masonry brick walls) with different structural arrangement (i.e. fully or partially filled frame) is investigated [5, 6, 37, 59]. Altin et al. [5] employed

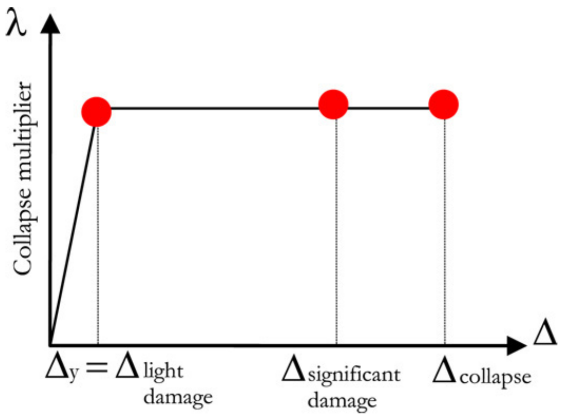

Figure 2.7: An illustration of the capacity curve proposed by Borzi et al. [23].

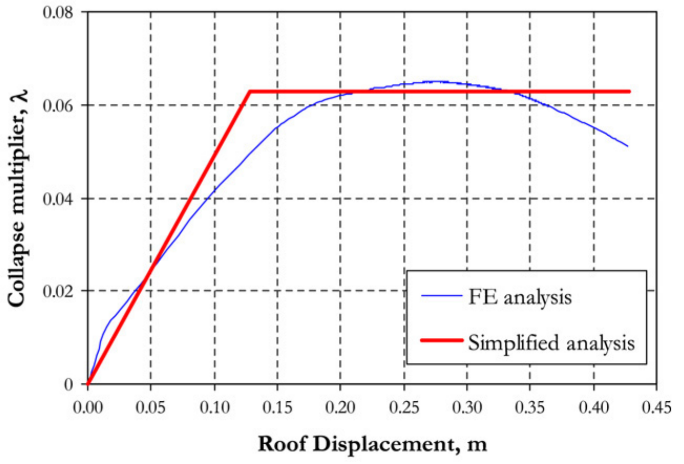

Figure 2.8: The capacity curves of a six-story RC structure in the numerical application performed by Borzi et al. [23].

three different strengthening techniques to rectify the inadequate lap splice length in the columns of nonductile infilled RC frames. The pushover analysis was then carried out and properly predicted the experimental capacity curves of the frames. Nonetheless, there were discrepancies between the analytical and experimental results on the initial stiffness and the post-ultimate load behaviour of the frames. These flaws, as stated by the authors, were due to the difference in the load application method and the shortcoming of the utilized software, respectively.

Moreover, some studies concern the use of pushover analysis procedure on the evaluation of the efficiency of other typical retrofitting techniques such as FRP-reinforcement [60, 99, 112, 175], steel bracing [154, 167], shear wall [17], shape memory alloys [20, 173] and base isolators [144]. Here, it is not intended to describe the retrofitting techniques in detail. A brief literature review is given in Chapter 4 and 5 on the seismic assessment of FRP reinforced and SMA reinforced structures, respectively.

2.3 Existing Finite Element Strategies

2.3.1 Distributed Plasticity

The idea of the distributed plasticity goes back to the model developed by Takizawa [170] for the dynamic analysis of RC buildings with high inelasticity. The model suggested a parabolic distribution of the flexural and shear stiffnesses along the element length. Its application on low-rise RC building was accomplished by the author in [169]. Soleimani et al. [161] developed a diffused plasticity model with a floating plasticity zone that starts from the end sections and spreads out to the mid-span as a function of loading level. In their model, the mid-part of the beam always remains elastic and the plasticity is limited to a finite length. Point hinges at the ends of the element simulate the rotations of the beam/column interfaces. The main drawbacks of this model was the lack of an independent hysteresis behaviour for the point hinges located at the beam/column interfaces plus the problem of element state determination, i.e. the determination of element resisting forces. The extension of the model is carried out by Mulas and Filippou [126], where the nonlinear beam element of Soleimani et al. is equipped with two nonlinear rotational springs that describe the fixed end rotations following a hysteretic relation. The proposed FEM strategy solves the problems that arise in the model of Soleimani et al. such as the element state determination. A similar study was also conducted by Meyer

et al. [124] on damaged concrete frames, where a mathematical model was presented to simulate the behaviour of RC members against severe cyclic loads. A finite length of distributed plasticity was taken into account for unloading and reloading. The advantage of the model with respect to already existing models was that only the material data and geometry of the section were the inputs of the model and no data calibration was required.

The distributed plasticity approach for more advanced proposed models, involves the evaluation of the behaviour at fixed points along the element span. These points are coincident with the quadrature points and depend on the adopted integration rule. In order to obtain accurate results in the framework of distributed plasticity, the use of finer meshes, higher order shape functions, or more quadrature points along the element is required, which inevitably leads to high computational complexity and time requirements. This issue is addressed in the pioneering work of Izzudin and Elnashai [78], who proposed an adaptive analysis approach as an alternative to the traditional elasto-plastic analysis of structural frames. The material nonlinearity is modelled through an elasto-plastic cubic formulation on the basis of the "plane section remains plane after deforming" hypothesis and also the neglection of shear and non-uniform torsional strains. As the analysis starts, all the structural members are modelled by elastic two-node quartic elements. In every loading step, the plasticity condition is checked in a selected number of monitoring points. If the plasticity condition is verified in a specific zone, an elasto-plastic cubic element is inserted in the plastic zone while the rest remains elastic, see Fig. 2.9. The main advantage of this mesh refinement process is that it consumes much less computational time with respect to the traditional method where a fine mesh is constructed for all the elements since the begining of the evaluation. The authors later admitted, in [81], the necessity of adopting the layered approach in the proposed adaptive analysis technique. The layered approach includes the breakdown of the RC cross-section into steel layers and concrete rectangular blocks, see Fig. 2.10. For the concrete, the confinement effect induced by steel stirrups is taken into account by setting a confinement factor. They also demonstrated that in order to obtain a preferable balance between the numerical accuracy and computational efficiency, the need to use quartic elastic elements, which allow representing a whole structural member with one element, is essential. The application of the proposed adaptive technique in nonlinear analysis of RC frames is performed in [85].

While the formulation of the distributed plasticity models are, in general, either based on the displacement-based element [182, 183] or force-based element

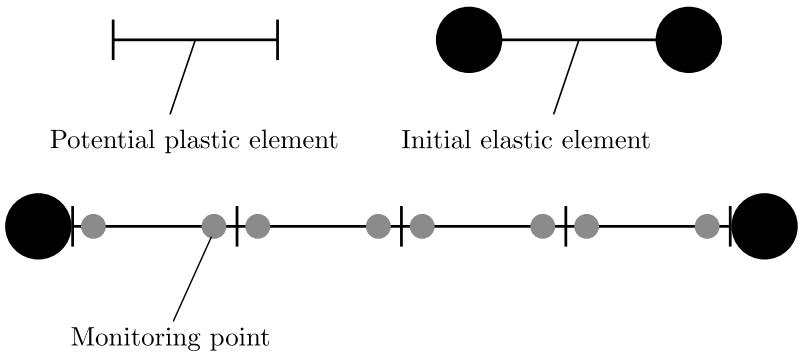

Figure 2.9: The adaptive model proposed by Izzudin and Elnashai [78].

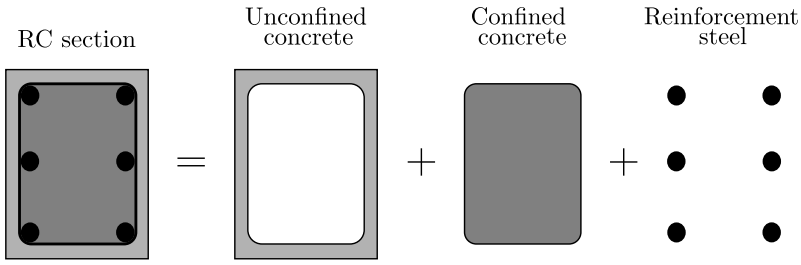

Figure 2.10: RC cross-section decomposition in layered approach.

[35, 36, 172], some studies concern the implementation of a two-field mixed formulation, catching the advantages of both formulations [3, 163]. Numerical issues regarding the implementation of displacement-based and force-based distributed plasticity models are tackled by Calabrese et al. [31] who demonstrated the exactness of the force-based formulation even in the presence of softening and the impotence of displacement-based formulation for the inelastic analysis (see also [178]). The latter has led to element mesh refinement in the application of displacement-based elements. However, updatable shape functions, as proposed by Pantó et al. [134], where displacement shape functions are automatically updated based on the degree of degradation of the element's stiffness, are able to improve the accuracy without element discretization.

To accurately describe the inelastic behaviour of the structural members under different loading conditions in the framework of distributed plasticity, the constitutive relations of the cross-sections are formulated based on the classical plasticity theory, i.e. resultant of stresses and strains, or by using fiber model. In the latter, which is indeed the most powerful approach, the responses of the elements are obtained through integration of the responses of traced cross-sections. The number of cross-sections depends on the number of quadrature points. Each cross-section is discretized into a finite number of fibers, each of which following the stress-strain constitutive law of a particular material, e.g. in RC structures, steel reinforcement, unconfined or confined concrete (Fig. 2.11). Contrary to the classical models that are mainly developed for rectangular sections, fiber models are able to capture the material and reinforcement details of any arbitrary-shaped cross-section. The stiffness matrix and resisting force vector of a generic cross-section are then determined by integrating the responses of the fibers. An optimum number of fibers should be employed for each cross-section from a balance between the accuracy and computational efficiency [164]. In fiber models, concrete cracking and steel buckling are accounted for. The plane sections assumption is considered by means of adopting an Euler-Bernoulli beam theory. The fiber models are capable in accounting the interaction between the axial force and bending moment, plus the coupling effect of biaxial bending moments.

A force-based fiber model was proposed in the early study of Spacone and Filippou [164]. The presented model was a refinement of an early version developed by Ciampi and Carlesimo [41] and enables the analysis of RC members subjected to cyclic biaxial bending moments under varying axial load. The model could also circumvent the numerical instabiities of the previous version, which were induced by the material softening behaviour. Petrangeli et al. [141]

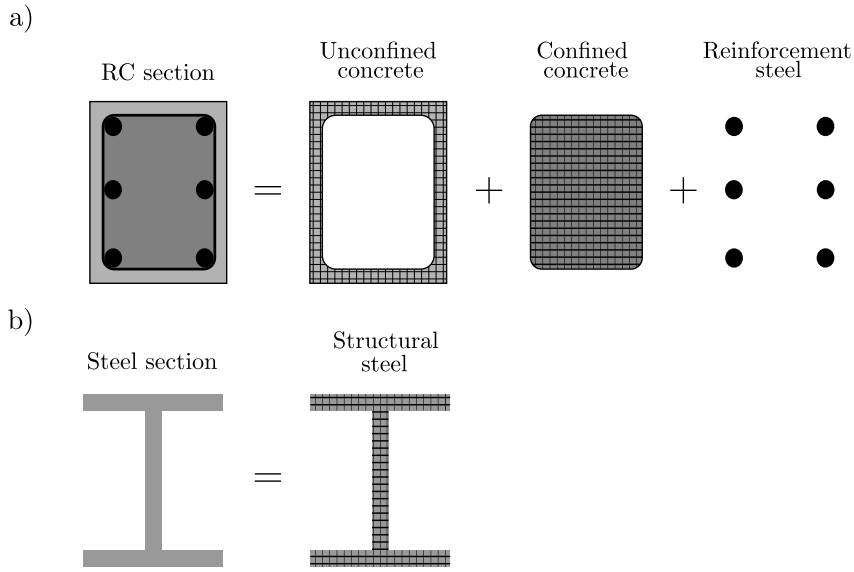

Figure 2.11: The discretization of (a) an RC section and (b) a steel cross section in the fiber approach.

incorporated the shear behaviour and its interaction with axial force and bending moment into a displacement-based fiber model. More studies on the fiber models have been carried out by Izzudin et al. [82] and Dömenz [54] on the combination of the fiber model with adaptive nonlinear approach, by Rosati et al. [153] on the limit state analysis of arbitrary shaped RC sections and more recently by Zubydan and ElSabbagh [185] on the evaluation of Concrete-Filled Steel-Tube (CFST) elements under axial and lateral loads.

In the sectional analysis of structures, the coupling between the biaxial bending moments and axial force is of great importance, since the variation of one (axial or flexure) may affect the performance of the other. While this interaction was totally ignored in the earlier studies, e.g. in [124, 132, 161], more recent studies have considered the effect of axial force on the ultimate moment capacity of the sections. In the framework of classical plasticity, Attalla et al. [10] developed a distributed plasticity model for steel frames that considers the combination of bending moment and axial force for the construction of the initial and full-plastic yield surfaces. For RC structures, Bousias et al. [24] proposed a bounding surface that accounts the coupling between the bending moments of the two directions and the axial force. In addition, the effect of

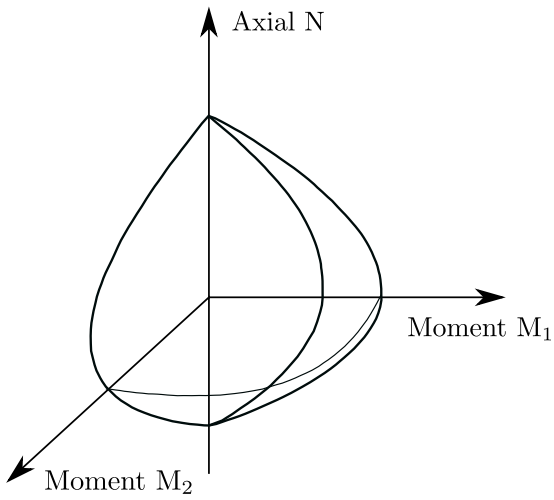

Figure 2.12: A bounding surface of RC section depending on biaxial bending moments and axial force.

bond slip and shear force are included by appropriately calibrating the model parameters that depend on geometry and details of steel reinforcement. A schematic representation of a bounding surface in the space of biaxial bending moments and axial force is shown in Fig. 2.12.

More recently, Mazza [118] proposed a distributed plasticity model, which is a generalization of a concentrated plasticity model, that exhibits the plasticity evolution by means of the degradation of the flexural stiffness along the beam element. The activation domain is defined in terms of axial force and biaxial bending moments for the elastic part (central region) and plastic parts (end regions with varying lengths of plasticity). The model is constructed by making two hypotheses: (1) the plastic sections that are in the same plastic zone behave identically and this behaviour is governed by the end sections; and (2) the stiffness of a plastic zone is equal to the stiffness of the related end section. The author verified the efficiency of the proposed model by comparing the results of the numerical examples with the results of a fiber analysis. Figure 2.13 describes the distributed model of Mazza as well as the result of one of its numerical applications.

In addition to the above-mentioned examples, many other analytical models based on different modelling strategies have been established in the literature, e.g. hysteresis modelling [151] or Mroz multisurface plasticity [66], to address

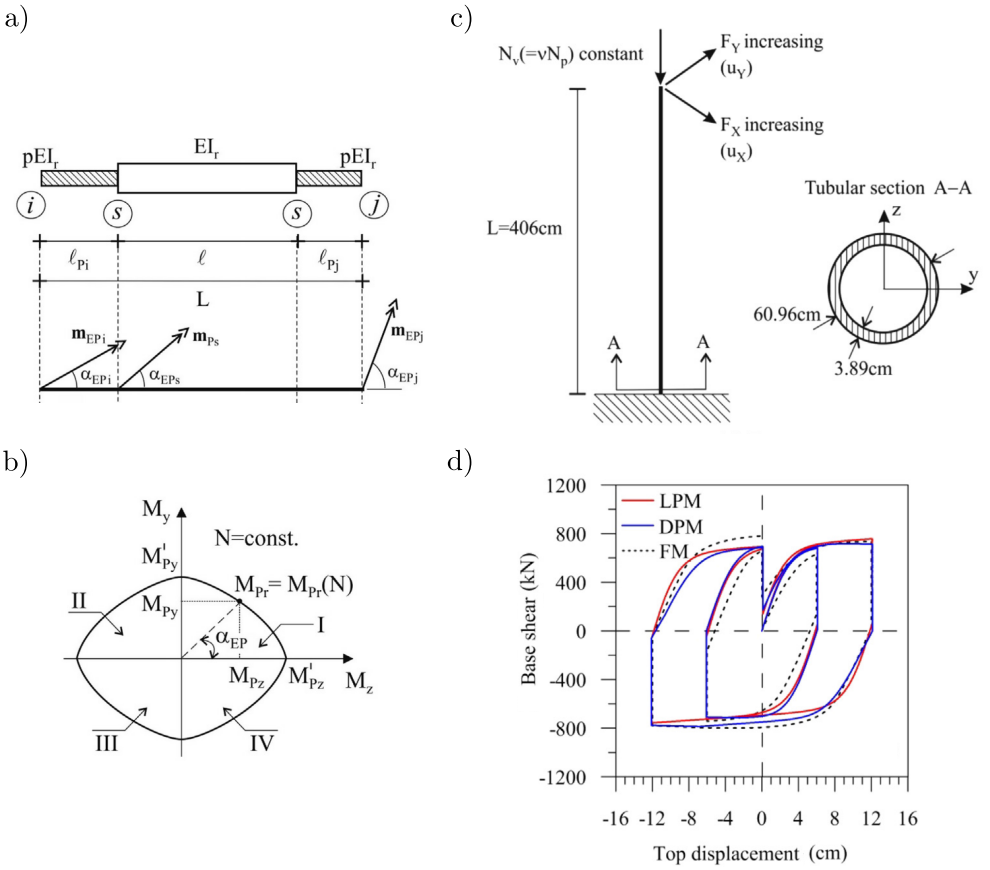

Figure 2.13: The distributed plasticity model of Mazza [118]: (a) the element with finite plastic zone, (b) the activation domain in the space of biaxial bending, (c) the illustration of the numerical example, and (d) the comparison of the results (LPM, DPM and FM, respectively, stand for Lumped Plasticity Model, Distributed Plasticity Model and Fiber Model).

the plasticity activation domain with particular emphasis on the interaction between axial force and bending moments.

2.3.2 Concentrated Plasticity

Unlike the distributed plasticity models, the concentrated plasticity (lumped plasticity) models presume that the inelasticity is limited to the end regions of the structural elements. This presumption is invoked by the fact that under lateral excitation (e.g. earthquake or wind), the structural elements experience larger values of bending moments at end regions. It should be noted here that the term "plastic hinge", which is usually referred in the literature of concentrated plasticity models, is used to describe a section of structural element in which a plastic bending occurs.

The concentrated plasticity models are constructed as a combination of either parallel or series subelements. These models originate from the two-component model of Clough and Johnston [43] characterized by a bilinear moment-curvature relation. The model is constructed by connecting two beams in parallel (Fig. 2.14(a)), one with elasto-plastic behaviour with plastic rotational springs at extreme nodes, and the other with elastic behaviour. The rotational springs are activated upon the excess of the end bending moments over the yield moment. The stiffness of the element is additively composed of the stiffness contribution of each beam. The multicomponent extention of the model was also developed by Aoyama and Sugano [7]. The model, as depicted in Fig. 2.14(b), consists of three elastic elements and two unique elasto-plastic rotational springs with trilinear hysteresis behaviour. The unique characteristic of the two rotational springs allows different level of concrete cracking and reinforcement steel yielding at the two ends of the element. Due to the lack of versatility in the hysteresis loop of the multicomponent beam models, Giberson [68] developed a one-component beam element with rotational springs attached to its ends in series (Fig. 2.14(c)). As shown by the author, the one-component beam element is able to describe curvilinear hysteresis loop, hence more appropriate for the hysteretic behaviour of RC members.

Many authors focused on the nonlinear constitutive behaviour of the hinge, usually furnishing directly an explicit formulation in its hysteretic stress-strain or load-deformation curve. Takeda et al. [168] suggested a complex hysteresis load-deformation curve for the inelastic rotational springs of RC element. The proposed hysteresis curve is defined in accordance with a trilinear primary curve and follows a set of different loading-unloading-reloading conditions in-

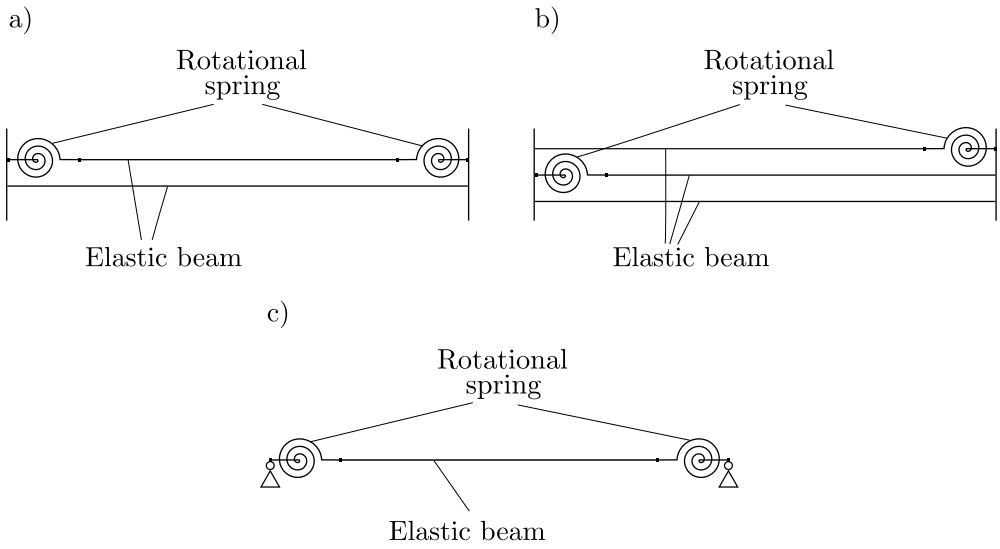

Figure 2.14: The early models of concentrated plasticity beam: (a) The two-component model of Clough and Johnston, (b) the multicomponent model of Aoyama and Sugano, and (c) the one-component model of Giberson.

cluding stiffness degradation in flexure, see Fig. 2.15. A similar study was also carried out by Brancaleoni et al. [27]. On the basis of fixed-end rotations of RC beam-column joints, Filippou et al. [63] formulated an analytical model for the hysteretic behaviour of RC members accounting the degree of deterioration of the bonding between concrete and steel, which may become significant under lateral load reversals.

Many studies are specifically concerned with using plastic hinge method in elasto-plastic analysis of steel frames [50, 79, 92, 93, 107, 143, 174, 176] and some others address the steel-concrete composite structures [69, 70, 77, 97]. Within the context of steel frames and under the hypothesis of small strains, Powell and Chen [143] developed a three-dimensional element, for the first time, with generalized plastic hinges accounting the interaction of axial force, biaxial bending moments and torsion. The element exhibits strain hardening while stiffness degradation and rate dependence are ignored. The stiffness matrix of the element is obtained by adding the stiffness of the elastic element and the plastic hinges. The elasto-plastic stiffness matrix of the hinge is derived

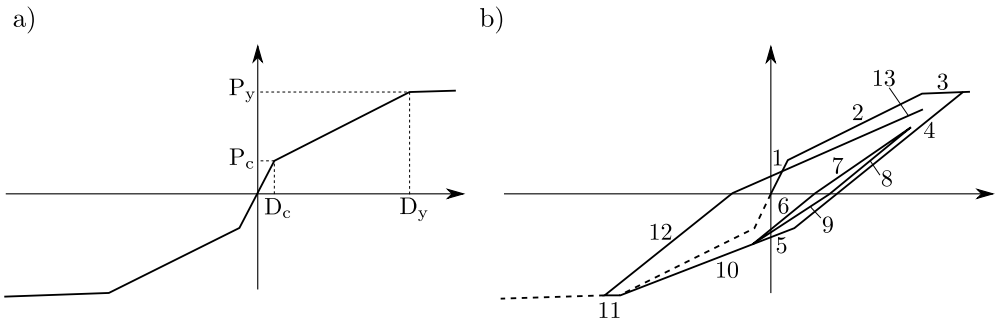

Figure 2.15: The primary load-deflection curve (a) and the hysteretic load-deflection curve (b) in the model of Takeda et al. [168]. The points (P_c, D_c) and (P_y and D_y), respectively, refer to cracking and yielding loads. Numbers identify different branches of loading and unloading in the hysteretic curve.

intuitively based on the overall work done by the plastic hinge as

$$\boldsymbol{k}_{ep} = \boldsymbol{k}_e - \frac{\boldsymbol{k}_e \boldsymbol{g}\boldsymbol{g}^T \boldsymbol{k}_e}{\boldsymbol{g}^T(\boldsymbol{k}_e + \boldsymbol{k}_p)\boldsymbol{g}}, \tag{2.1}$$

where $\boldsymbol{k}_e$ and $\boldsymbol{k}_p$ are the matrices of initial stiffness and plastic stiffness of the hinge, respectively, and $\boldsymbol{g}$ is a vector defining the direction of the plastic increment on the yield surface. The yield surfaces follow the Mroz plasticity theory for metals and are formed by taking into consideration the interaction of axial force and bending moments plus the effect of torsion as

$$f = \left[(\frac{M_y}{M_{yu}})^2 + (\frac{M_z}{M_{zu}})^2 + (\frac{T}{T_u})^2\right]^{1/2} + (\frac{F}{F_u})^2, \tag{2.2}$$

where M_y, M_z are bending moments about z and y axes respectively, T is torsion and F is axial force. Symbols with u subscript represent the yield strengths of each component.

A similar study is reported by Hilmy and Abel [73] for the dynamic analysis of steel frames.

To overcome the problem of lack of axial force-bending moment coupling, Lai et al. [96] developed a fiber plastic hinge model that simulates the stiffness degradation and varying axial force. The model consists of one elastic element and two inelastic elements at end regions. The latter is simulated using five inelastic springs, four located at corners and one in the center of the section, which is purely responsible for the compressive behaviour, see Fig. 2.16. The

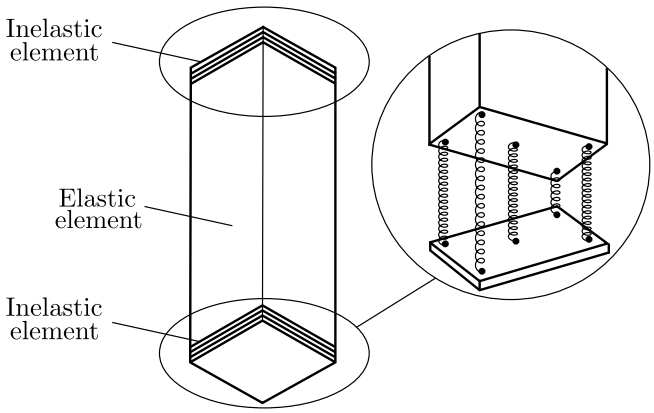

Figure 2.16: The inelastic RC member proposed by Lai et al. [96].

five springs model simulated, in a more sophisticated manner with respect to the classical plasticity, the interaction domain of axial force and bending moment. Other efforts include the interaction between shear and torque in the evaluation of asymmetric structures [46] and also the inclusion of hardening effect in bi-dimensional hinges for the analysis of steel structures under earthquake motions [87]. Some studies have considered the effect of involvement of geometric nonlinearities in the plastic hinge models. White [176] investigated the efficiency of different plastic hinge approaches contemplating the second-order effects caused by geometric nonlinearities. In braced steel structures, a number of plastic hinges may occur in the mid-span of braces due to buckling. In the conventional analysis method, since the position of the plastic hinges formed in the braces are not known in advance, through an inaccurate simplification the position of plastic hinges were fixed exactly at the middle of braces. This issue has been dealt with by Izzuddin and Elnashai [79]. They proposed an elastic perfectly plastic model of hinges integrated in an adaptive analysis FEM tool, which offers significant computational savings. The method follows the same procedure of adaptive analysis for distributed plasticity in [78], as described in Section 2.3.1, and includes the geometric nonlinearities caused by buckling. Initially, the analysis begins with one element per member. When the plastic hinge is detected in an element, the element is automatically subdivided into two subelements in which finer mesh is implemented (see Section 2.3.3 for a detailed discussion of the model). Although the capability of the proposed plastic hinge method was confirmed by numerical examples, it was stated by

the authors that the proposed method is only justifiable for the cases where the material exhibits no plastic hardening and also the spread of plasticity along the height and length of the elements is not considerable.

One major limitation of the concentrated plasticity models that needs to be attended is the effect of zero inelastic length zone that may lead to an overestimation of the ultimate strength of structures. A quasi-plastic-hinge approach was developed by Attalla et al. [10] that accounts the spread of inelasticity without the member discretization along the length and over the cross-section in the space of combined bending moments and axial force. The gradual plastification, as referred by the author, over the cross-section is performed by calibrating the parameters of the inelastic strain models, i.e. the models of inelastic axial strain and inelastic curvature, using a fiber analysis program. The inelastic axial strain and curvature are determined by dividing the element into the elastic and elasto-plastic regions (Fig. 2.17) and thus integrating the response of different regions. Based on the values of end bending moments, the length of the plastic part is calculated as

$$L_p^{(i)} = \frac{(M_i - M_{rc})}{M_i + M_j} L, \tag{2.3}$$

and

$$L_p^{(j)} = \frac{(M_j - M_{rc})}{M_i + M_j} L, \tag{2.4}$$

where M_{rc} is the initial yield moment, which is a function of axial force.

Following the latter study, many studies have been carried out to implement the quasi-plastic-hinge approach for the analysis of steel frames [104] and RC frames [103] and also to improve its efficiency [19, 105].

A more favourable solution to the above limitation is to extend the zero length plastic hinge to a finite inelastic region. The aim in this case is to combine the accuracy of the distributed plasticity method with the computational efficiency of the concentrated plasticity method. Many experimental and theoretical studies [13, 44, 138, 150, 158] have been reported to estimate the effective length of plastic hinges. Paulay and Priestley [138] suggested

$$L_p = 0.08z + 0.022 d_b f_y, \tag{2.5}$$

where d_b and f_y, respectively, represent the diameter and the yield strength of the longitudinal steel reinforcement, and z is the height of the section, as the

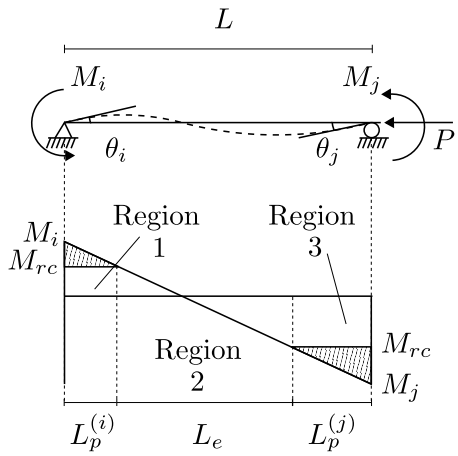

Figure 2.17: The spread of inelasticity at the ends of a simply supported beam, as illustrated by Attalla et al. [10].

effective plastic hinge length of RC beams and columns. Sheikh and Khoury [158] estimated the length of plastic hinge of columns to be roughly equal to the section depth. Bae and Bayrak [13] derived the following expression for the plastic hinge length of RC columns

$$L_p = h\big[(0.3(\frac{P}{P_0}) + 3(\frac{A_s}{A_g}) - 0.1)(\frac{z}{\lambda}) + 0.25\big] \geq 0.25, \tag{2.6}$$

where h is the depth of the section, λ is the distance from the critical section to the contraflexure point, $\frac{P}{P_0}$ is the level of axial force and $\frac{A_s}{A_g}$ is the ratio of longitudinal steel reinforcement in the section. An extended review on the plastic hinge length is provided by Zhao et al. in [180]. Moreover, it has been observed in the experimental studies of RC structures subjected to cyclic loadings that due to irreversible plastic strain in the reinforcing bars, the plastic hinges evolved in RC beams elongate about 2-4% of the section depth [61, 62]. Analytical solutions have predicted the plastic hinge elongation based on different parameters such as longitudinal axial strain [100] and the variation of interstory drift [115].

The generalized plastic hinge model of Alhasawi et al. [4] is an example of plastic hinge models with the ability to elongate (or shorten) along the beam axis. In this model, the plastic hinges are simulated using axial and rotational springs to couple the axial force and bending moment in the plasticity evolution

of the element. Material and geometry nonlinearities are included using a co-rotational coordinate transformation technique. See [4, 16] for a detailed description of co-rotating elements.

2.3.3 Improved Concentrated Plasticity Models

In the earlier models of beams with concentrated plasticity, the plastic hinges are only allowed to evolve at the ends of the elements. However, in some circumstances, the structure subjected to lateral excitation may experience plastic hinges forming not only at the ends of its structural elements but along its length. Conventionally, this case is addressed by adding internal nodes in the mid-span of the element to divide it into several sub-elements so that the presence of internal hinges is also accounted for [88, 108, 109]. Although this treatment propounds the possibility of internal plastic hinges, the location of internal plastic hinges should be specified a priori, which undoubtedly is a controversial assumption. Moreover, additional nodes increase the number of degrees of freedom (DOF) and, consequently, decreases the computational efficiency. Here, two different models developed in the literature are discussed, which are able to consider the presence of internal plastic hinges that are not necessarily formed at the mid-span of the elements.

2.3.3.1 The adaptive plastic hinge model of Izzuddin and Elnashai [79]

Izzuddin and Elnashai [79] proposed a plastic hinge model for steel beam that includes geometric nonlinearities caused by buckling and neglects the effect of strain hardening. The model is based on an elastic quartic formulation, which allows representing a whole structural member with one element, possessing eight local DOFs (Fig. 2.18). An extra DOF is provided in the mid-span of the element that, as stated by the author in [80], improves the accuracy of the solution to a large extent. The proposed plastic hinge, when activated, obeys the rigid-perfectly plastic constitutive rule and its formation is merely governed by the interaction between axial force and bending moment.

Initially, the analysis starts with all the elements modelled using one elastic quartic element. In every step of the analysis, the plasticity is checked along the element and if it is verified in a point, the element will be divided in two sub-elements, with the intersection node located at the plastic point (Fig. 2.19), and also a finer mesh will be assigned to it for the rest of the analysis. The main advantages of this process with respect to the non-adaptive models

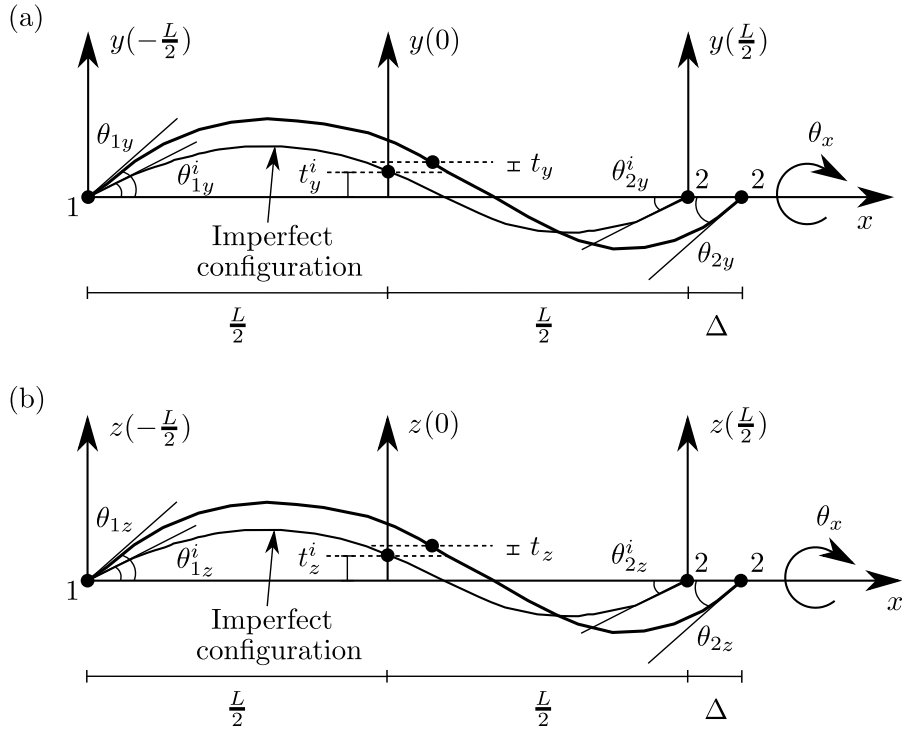

Figure 2.18: The local DOFs in the elastic quartic element of Izzuddin and Elnashai [79]: (a) in the $x-y$ axis and (b) in the $x-z$ axis. The variables with i superscript are related to the initial imperfection, see [80].

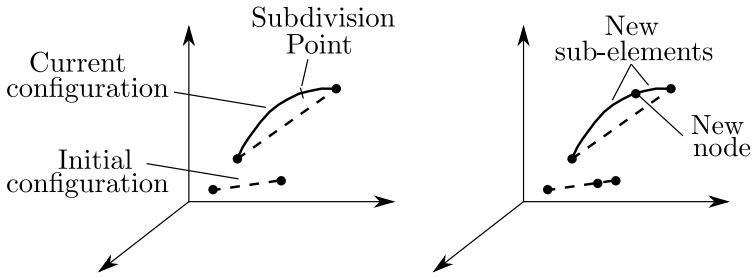

Figure 2.19: The element subdivision in the model of Izzuddin and Elnashai [80].

are high computational savings as well as the positions of the internal plastic hinges that are specified through the analysis procedure and are not based on a primary elastic analysis.

2.3.3.2 The refined plastic hinge model of Liu and Li [111]

This model is another plastic hinge model developed for steel structures that is able to catch internal plastic hinges. The model considers geometric and material nonlinearities by including the spread of plasticity over the cross-section, the second-order effect of axial force, shear deformation, and also the initial imperfection of the structural elements.

With reference to Fig. 2.20, an internal node C is inserted along the element to divide it into part a and part b, respectively, with the lengths L_a and L_b. The incremental force-displacement relationship of part a and part b are, respectively, expressed as

$$\begin{bmatrix} \mathrm{dQ}_1 \\ \mathrm{dM}_1 \\ \mathrm{dQ}_{1\mathrm{c}} \\ \mathrm{dM}_{1\mathrm{c}} \end{bmatrix} = \left[\boldsymbol{K}_{pa}\right] \begin{bmatrix} \mathrm{d}\delta_1 \\ \mathrm{d}\theta_1 \\ \mathrm{d}\delta_{1\mathrm{c}} \\ \mathrm{d}\theta_{1\mathrm{c}} \end{bmatrix}, \tag{2.7}$$

and

$$\begin{bmatrix} \mathrm{dQ}_{2\mathrm{c}} \\ \mathrm{dM}_{2\mathrm{c}} \\ \mathrm{dQ}_2 \\ \mathrm{dM}_2 \end{bmatrix} = \left[\boldsymbol{K}_{pb}\right] \begin{bmatrix} \mathrm{d}\delta_{2\mathrm{c}} \\ \mathrm{d}\theta_{2\mathrm{c}} \\ \mathrm{d}\delta_2 \\ \mathrm{d}\theta_2 \end{bmatrix}, \tag{2.8}$$

where $\boldsymbol{K}_{pa}$ and $\boldsymbol{K}_{pb}$ are the elasto-plastic stiffness matrices of part a and part b, respectively.

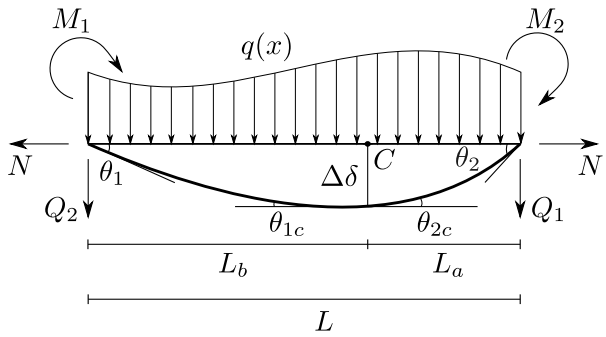

Figure 2.20: The beam element with mid-node C as the location of the internal plastic hinge (the model of Liu and Li [111]).

Then, the two equations (2.7) and (2.8) are assembled to give the global force-displacement relationship of the element as

$$\begin{bmatrix} \mathrm{dQ_1} \\ \mathrm{dM_1} \\ \mathrm{dQ_2} \\ \mathrm{dM_2} \\ \mathrm{dQ_{1c}} + \mathrm{dQ_{2c}} \\ \mathrm{dM_{1c}} + \mathrm{dM_{2c}} \end{bmatrix} = \left[\boldsymbol{K}_p\right] \begin{bmatrix} \mathrm{d}\delta_1 \\ \mathrm{d}\theta_1 \\ \mathrm{d}\delta_2 \\ \mathrm{d}\theta_2 \\ \mathrm{d}\delta_\mathrm{c} \\ \mathrm{d}\theta_\mathrm{c} \end{bmatrix} . \tag{2.9}$$

Equation (2.9) can be partitioned into external and internal parts

$$\begin{bmatrix} \mathrm{d}\mathbf{f}_\mathrm{e} \\ \mathrm{d}\mathbf{f}_\mathrm{i} \end{bmatrix} = \begin{bmatrix} \boldsymbol{K}_{ee} & \boldsymbol{K}_{ei} \\ \boldsymbol{K}_{ei}^T & \boldsymbol{K}_{ii} \end{bmatrix} \begin{bmatrix} \mathrm{d}\boldsymbol{\delta}_\mathrm{e} \\ \mathrm{d}\boldsymbol{\theta}_\mathrm{i} \end{bmatrix} , \tag{2.10}$$

with $\mathrm{d}\mathbf{f}_\mathrm{e} = [\mathrm{dQ_1} \quad \mathrm{dM_1} \quad \mathrm{dQ_2} \quad \mathrm{dM_2}]^\mathrm{T}$, $\mathrm{d}\mathbf{f}_\mathrm{i} = [\mathrm{dQ_{1c}} + \mathrm{dQ_{2c}} \quad \mathrm{dM_{1c}} + \mathrm{dM_{2c}}]^\mathrm{T}$, $\mathrm{d}\boldsymbol{\delta}_\mathrm{e} = [\mathrm{d}\delta_1 \quad \mathrm{d}\boldsymbol{\theta}_1 \quad \mathrm{d}\delta_2 \quad \mathrm{d}\theta_2]^\mathrm{T}$ and $\mathrm{d}\boldsymbol{\theta}_\mathrm{t} = [\mathrm{d}\delta_\mathrm{c} \quad \mathrm{d}\theta_\mathrm{c}]^\mathrm{T}$.

Through the static condensation approach, since no external force is acting at point C, i.e. $\left[\mathrm{d}\mathbf{f}_\mathrm{i}\right] = \left[0\right]$, Eq. (2.10) is condensed as

$$(\boldsymbol{K}_{ee} - \boldsymbol{K}_{ei}\boldsymbol{K}_{ii}^{-1}\boldsymbol{K}_{ei}^T)\left[\mathrm{d}\boldsymbol{\delta}_\mathrm{e}\right] = \left[\mathrm{d}\mathbf{f}_\mathrm{e}\right] . \tag{2.11}$$

In this method, the position of the mid-node C is set in accordance with the position of the maximum bending moment along the element. Two typical cases are investigated, beam with concentrated load acting on it, and beam

with constant distributed load. In the case of beam with concentrated load, the mid-node C is placed at the position of the concentrated load. In the case of beam with constant distributed load, the position of the mid-node C is not fixed and is estimated by equating the equation of shear force to zero as

$$\frac{\mathrm{dM(x)}}{\mathrm{dx}} = 0 \rightarrow x = \frac{M_1 - M_2}{q\,L} + \frac{1}{2}L, \tag{2.12}$$

where M_1 and M_2 are the values of bending moment at the two ends and q is the magnitude of the constant distributed load.

For a mixed case, where a beam is subjected to both concentrated and constant distributed loads, the beam is firstly divided into two parts with the mid-node located at the point of the concentrated load. Afterwards, each part is treated as a single beam with distributed loads and thus the positions of the maximum bending moments are indicated by Eq. (2.12).

Similarly, Liu et al. [110] developed a curved beam-column element for steel structures that follows the same static condensation approach of [111] and is enriched with the feature of capturing any arbitrary located plastic hinge. In this model also, the position of the internal plastic hinge should be estimated, in advance, by means of an elastic analysis based on the maximum value of the bending moment.

2.4 Conclusions

This chapter was devoted to an overview of the pushover analysis technique and the existing plasticity models for beams. Due to the applicability of the pushover analysis technique, it has received vast theoretical and even empirical attentions by different researchers. Despite its approximate nature, since it does not suffer from huge computational cost and complexity of its dynamic counterpart, it presents a convenient analysis method in which novel plasticity model can be readily incorporated.

Many distributed and concentrated plasticity models have been developed through different mathematical expressions to capture the inelastic response of structures subjected to severe loading conditions. While distributed plasticity models are more appreciated in the literature thanks to their ability to catch the material inelasticity rigorously, concentrated plasticity models have attracted more applicants due to their simplicity and computational efficiency. On the other hand, some studies have reported the overestimation of the ultimate structural strength provided by the concentrated plasticity models. The

inclusion of internal plastic hinges is a possible solution to overcome the inaccuracy of the concentrated plasticity models. Although different models are suggested in the literature that are able to capture internal plastic hinges, most of them, to the knowledge of the writer, are formulated for steel structures. In addition, in many cases, the location of the internal plastic hinge is based on the maximum value of the bending moment. Even if this might be considered adequate for steel and RC elements with uniform characteristics of the cross-sections, however, it does not compass the cases showing non-uniformity, e.g. RC beam with different longitudinal steel reinforcement distribution.

Consequently, albeit many plasticity models have been suggested in the literature to balance between the response precision and computability, i.e. complexity and computation time, the need to adopt an efficient and applicable plasticity model that evokes the advantages of both distributed and concentrated plasticity models and which can be easily incorporated into an FEM procedure is still required.

Chapter 3

Proposed FEM Procedure for Nonlinear Analysis of RC Framed Structures

3.1 Introduction

Based on the classical theory of structures, when in a ductile beam the maximum moment capacity of a section is reached, a sudden change in the slope of the member occurs at that section through the formation of a plastic hinge. As a result, slope discontinuity implies in the location of the plastic hinge. Henceforward, the section develops plastic rotation and its behaviour is characterized in terms of moment-plastic rotation relation of the plastic hinge.

The integration of the static governing differential equation of the uniform Euler-Bernoulli beam in the presence of slope discontinuities has been carried out by Biondi and Caddemi [21, 22]. The authors demonstrated that the slope discontinuity modelled through a Dirac's delta distribution of the flexural stiffness corresponds to the presence of an internal hinge with rotational spring. The proposed closed form expression of the beam can offer the basis for efficient treatment of lumped plasticity models.

In this Chapter, the closed form expression of the beam proposed by Biondi and Caddemi [22] is implemented in an original FEM beam element where plastic hinges can appear at any arbitrary position. The constitutive equations of the beam are generated based on the associated elasto-plastic theory. The yield function defining the section failure is of Bresler's type [28], formulated

considering the interaction of axial force and biaxial bending moments. More specifically, the procedure presented by Fossetti and Papia is followed [65].

In this chapter, the work is devoted to the implementation of Biondi and Caddemi's basic idea in a finite element environment, adding a thermodynamic counterpart for elasto-plastic materials and managing consistently and in an efficient way the numerical evolution of plastic variables. Special attention is directed to RC structures and a more appropriate activation domain for plasticity evolution in such structures is coupled. In this sense, the work can be interpreted as an extension and completion of Biondi and Caddemi's one [22].

With respect to other strategies available in the literature, the proposed approach overcomes the problems linked with a mesh refinement and recovers the computational time connected with the increase of DOFs or the use of higher order shape functions. It also doesn't need any static condensation of internal DOFs. The model includes the possibility to overcome geometric limitations, permitting to assign specific geometry and reinforcing steel bars distribution to each section of an element. The proposed numerical examples, showing the formation of internal plastic hinges in RC structures (to the best of author's knowledge, no such study is reported in the literature) can be considered as novelty points as well.

The writer indicates that this chapter of the thesis is mostly taken from the paper by Rezaee Hajidehi et al. [147].

3.2 The Theoretical Framework

3.2.1 Beam with Slope Discontinuities

Let us consider an Euler-Bernoulli beam with multiple slope discontinuities as in Fig. 3.1. For the sake of simplicity, a two-dimensional beam is considered in x-z plane. The flexural stiffness of the beam is defined by a constant value $E_0 I_0$ with the superimposition of Dirac's delta distribution as follows (see [21] or [22]),

$$E(x)I(x) = E_0 I_0 \Big(1 - \sum_{i=1}^{n} \gamma_i \delta(x - x_i)\Big), \tag{3.1}$$

where γ_i represent the singularity intensities, x_i are the relevant singularity positions and δ is the Dirac's delta function. As reported in [29], according to

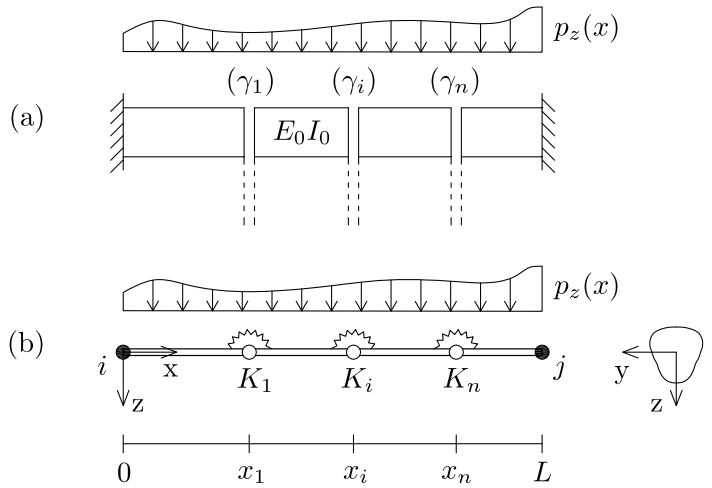

Figure 3.1: Euler-Bernoulli beam with Dirac's delta singularities in the flexural stiffness and (b) its equivalent beam with rotational springs and internal hinges.

the distribution theory, $I(x)$ is not defined at x_i. Instead, its properties are defined by integration after multiplication by test function. Thus, the inertia moment does not take negative values at x_i. In addition, as it will be shown later, the γ_i parameters do not take on values greater or equal to 1.

According to the Euler-Bernoulli beam theory, the static governing differential equation of a uniform beam is written as

$$V_z'(x) = -p_z(x); \qquad M_y'(x) = V_z(x), \tag{3.2a}$$

$$\kappa_z(x) = \frac{M_y(x)}{E(x)I(x)}, \tag{3.2b}$$

$$\kappa_z(x) = \varphi_y'(x); \qquad \varphi_y(x) = -u_z'(x), \tag{3.2c}$$

representing, respectively, the equilibrium, constitutive and compatibility equations. In the set of differential Eqs. (3.2), $V_z(x)$ and $M_y(x)$ represent the shear force and bending moment, respectively, $\kappa_z(x)$, $\varphi_y(x)$, and $u_z(x)$ represent the curvature, slope and deflection functions, respectively, and the prime sign denotes the derivative with respect to coordinate x.

The fourth-order differential equation of the Euler-Bernoulli beam, showing multiple slope discontinuities, in terms of deflection can be immediately derived by combining Eq. (3.1) and the set of Eqs. (3.2) as

$$[E_0 I_0 \Big(1 - \sum_{i=1}^{n} \gamma_i \delta(x - x_i)\Big) u_z''(x)]'' = p_z(x). \tag{3.3}$$

The full integration of Eq. (3.3) leads to the following closed form expression of the deflection $u_z(x)$ as

$$u_z(x) = c_1 + c_2 x + c_3 g_1(x) + c_4 g_2(x) + \frac{p_z^{[4]}(x)}{E_0 I_0} + \sum_{i=1}^{n} \frac{\gamma_i}{1 - \gamma_i A} \frac{p_z^{[2]}(x_i)}{E_0 I_0} (x - x_i) U(x - x_i), \tag{3.4}$$

where $U(x - x_i)$ represents the unit step function at x_i, $p_z^{[k]}(x)$ indicates a primitive order of k of the external load function $p_z(x)$, c_i are the integration constants, and

$$g_1(x) = x^2 + 2 \sum_{i=1}^{n} \frac{\gamma_i}{1 - \gamma_i A} (x - x_i) U(x - x_i), \tag{3.5a}$$

$$g_2(x) = x^3 + 6 \sum_{i=1}^{n} \frac{\gamma_i}{1 - \gamma_i A} x_i (x - x_i) U(x - x_i). \tag{3.5b}$$

With reference to Eqs. (3.2), the first and second derivatives of the deflection function in Eq. (3.4), respectively expressed as

$$\varphi_y(x) = -c_2 - 2c_3 \Big(x + \sum_{i=1}^{n} \frac{\gamma_i}{1 - \gamma_i A} U(x - x_i)\Big) - 3c_4 \Big(x^2 + 2 \sum_{i=1}^{n} \frac{\gamma_i}{1 - \gamma_i A} x_i U(x - x_i)\Big) - \frac{p_z^{[3]}(x)}{E_0 I_0} - \sum_{i=1}^{n} \frac{\gamma_i}{1 - \gamma_i A} \frac{p_z^{[2]}(x_i)}{E_0 I_0} U(x - x_i), \tag{3.6}$$

and

$$\kappa_z(x) = -\Big(2c_3 + 6c_4 x + \frac{p_z^{[2]}(x)}{E_0 I_0}\Big) - \sum_{i=1}^{n} \Big(2c_3 + 6c_4 x_i + \frac{p_z^{[2]}(x_i)}{E_0 I_0}\Big) \frac{\gamma_i}{1-\gamma_i A} \delta(x - x_i), \quad (3.7)$$

provide the complete kinematical outline of the element.

It can be demonstrated that the slope function $\varphi_y(x)$ has jump discontinuities at x_i, whose values correspond to those obtained in presence of internal hinges and rotational springs having stiffness equal to

$$k_{\varphi,i} = \frac{1-\gamma_i A}{\gamma_i} E_0 I_0. \quad (3.8)$$

The parameter A, which appears in Eqs. (3.4) to (3.8), is a constant, having the unit of 1/length, that comes out in the case of a product of two Dirac's deltas both centered at x_i, as defined by Bagarello [14]. Its value is always 2.013 independently on the element dimensions, and with the same unit as the Dirac's delta distribution, according to the physical meaning for what the distribution is applied. It is immediate to understand from Eq. (3.8) that the Dirac's delta has the unit of the inverse of a length, while the γ_i parameters are measured as a length. The parameter γ_i can range from 0 to $\frac{1}{A}$, with $\gamma_i = 0$ and $\gamma_i = \frac{1}{A}$ providing continuous beam without slope discontinuity and beam with a pure hinge respectively.

3.2.2 Thermodynamics

The constitutive relation at a generic section x can be written in the classical way as

$$\boldsymbol{Q} = \boldsymbol{\Phi}_0 \boldsymbol{q}^e, \quad (3.9)$$

where $\boldsymbol{Q} = [N\ M_x\ M_y\ M_z]^T$ is the vector of internal forces with N representing the axial force and M_x, M_y and M_z representing the moments about the three axes of the local reference system, $\boldsymbol{\Phi}_0$ is the sectional stiffness matrix at the virgin state, and $\boldsymbol{q}^e$ is the associated elastic strain vector.

The total strain vector $\boldsymbol{q}$ is assumed as the sum of the elastic part $\boldsymbol{q^e}$ and the plastic part $\boldsymbol{q^p}$,

$$\boldsymbol{q} = \boldsymbol{q}^e + \boldsymbol{q}^p. \quad (3.10)$$

Since the inelastic flexural curvatures are only considered here, the inelastic strain vector is expressed as

$$\boldsymbol{q}^p = [0\ 0\ \kappa_y^p\ \kappa_z^p]^T, \tag{3.11}$$

where κ_y^p and κ_z^p are the plastic curvatures in x-y and x-z planes respectively.

Following the method of local state [101], it is possible to define a thermodynamic potential from which the state laws can be derived. Considering an isothermal purely mechanical process without the inclusion of hardening or softening effects, the specific Helmholtz free energy of an elasto-plastic section is

$$\Psi(\boldsymbol{q}^e) = \frac{1}{2}\boldsymbol{q}^{e^T}\boldsymbol{\Phi}_0\boldsymbol{q}^e. \tag{3.12}$$

The instantaneous dissipation, expressed in the form of the Clausius-Duhem inequality, reads

$$D := \boldsymbol{Q}^T\dot{\boldsymbol{q}} - \dot{\Psi} = \boldsymbol{Q}^T\dot{\boldsymbol{q}}^p \geq 0, \tag{3.13}$$

where additive decomposition (3.10) has been used. The dissipative mechanism is driven by an activation function defined in the space of static variables.

A plastic condition is reached in the section when the following condition holds,

$$\phi^p(\boldsymbol{Q}) \geq 0, \tag{3.14}$$

with $\phi^p(\boldsymbol{Q})$ representing the limit function, which is explicitly defined in sub-Section 3.2.3.

Assuming that the model belongs to the class of generalized standard materials [18], the theorem of maximum dissipation [101] provides the complete set of evolution equations, by maximizing the dissipation function (3.13) with respect to the static variables. Adopting the Lagrangian multiplier method, the constrained maximization problem is equivalent to the following unconstrained saddle-point problem,

$$\min_{\dot{\lambda}^p}\max_{\boldsymbol{Q}} L(\boldsymbol{Q}) = \boldsymbol{Q}^T\dot{\boldsymbol{q}}^p - \dot{\lambda}^p\phi^p, \tag{3.15}$$

where λ^p is the Lagrangian multiplier.

The Kuhn-Tucker conditions of the problem (3.15) provide the flow rule for the plastic strain vector,

$$\frac{\partial L}{\partial \boldsymbol{Q}} = \boldsymbol{0} \Rightarrow \dot{\boldsymbol{q}}^p = \dot{\lambda}^p\frac{\partial \phi^p}{\partial \boldsymbol{Q}}, \tag{3.16}$$

under the following loading-unloading conditions,

$$\phi^p \leq 0,\ \dot{\lambda}^p \geq 0,\ \dot{\lambda}^p \phi^p = 0. \tag{3.17}$$

3.2.3 Elasto-plastic Failure Surface

The evaluation of the ultimate capacity of reinforced concrete members subjected to combined axial force and biaxial bending moments and the construction of a suitable activation domain have been extensively investigated [33, 45, 49, 94, 98, 156]. In order to verify a section under the actions of axial force N and biaxial bending moments M_y and M_z, the following expression is used for constructing the three-dimensional failure surface of the RC section [28],

$$\left(\frac{M_y}{M_{uy}}\right)^{\beta} + \left(\frac{M_z}{M_{uz}}\right)^{\beta} = 1, \tag{3.18}$$

where M_{uy} and M_{uz} represent the ultimate moment capacities of the cross-section, which are associated with the axial force N acting on the section. The values of M_{uy} and M_{uz} are calculated based on the Theory of Limit States [135] for an Euler-Bernoulli beam, under the following assumptions:

- plane sections before bending remain plane after bending,
- perfect bond exists between steel bars and concrete, i.e. there is no slip at the interface between steel bars and concrete,
- stress-strain curves of the materials are adopted as those in Fig. 3.2,
- tensile strength of concrete is neglected,
- at ultimate strength, the maximum strain of the extreme compression fiber is assumed equal to 0.35%, as suggested by Italian Building Code [75].

For a detailed description of the procedure of calculating M_{uy} and M_{uz} the reader is referred to [145].

In Eq. (3.18), the exponent β is a function of the cross-section's characteristics as well as the level of compression. The expression adopted here for the evaluation of β has been taken from the work of Fossetti and Papia [65],

$$\beta = \beta_1 \beta_2, \quad \text{with} \begin{cases} \beta_1 = 1.2 + 0.2(\frac{h}{b} - 1) \leq 1.3 \\ \beta_2 = 1 + 0.5\,|n - 0.45| \end{cases} \tag{3.19}$$

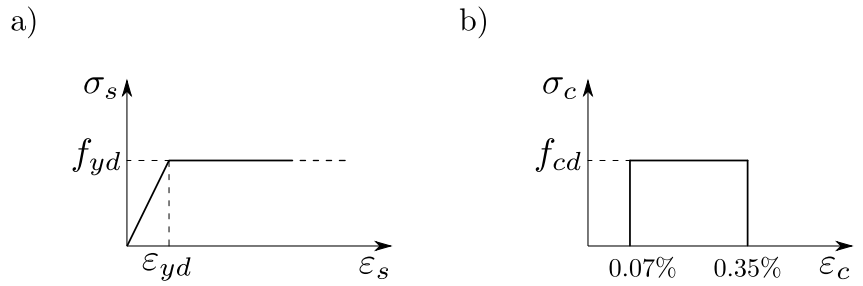

Figure 3.2: The adopted stress-strain laws for steel reinforcement bars (a) and concrete (b) in the evaluation of ultimate moment capacities.

where h and b are the height and the width of the rectangular cross-section respectively, and $n = \frac{N}{bhf_{ck}}$ is the level of compression of the section, with f_{ck} as the nominal compressive strength of concrete.

The resulting failure surface is a convex hull, whose characteristic points in the $N - M_z$ plane are defined as follows, see Fig. 3.3(a-b),

- point $[N_0, M_0]$, maximum positive axial force on the section,
- point $[N_1, M_1]$, failure of the section in pure bending,
- point $[N_2, M_2]$, balance point, in which the top fiber of the concrete reaches its maximum strain and the tensile steel bars reach the yielding strain,
- point $[N_3, M_3]$, maximum compressive axial force on the section, i.e. yielding of all steel bars in compression and crushing of concrete.

Along the loading process, when internal forces at a specific section furnish a point inside the activation domain, then the behaviour is elastic. Otherwise, plastic curvatures develop following the elasto-plastic flow rule (3.2.2). The axial force plays the role of static variable in specifying the plastic resistance of the section, see [145]. The activation domain is obtained by cutting the failure surface with a plane orthogonal to the N axis. The correspondent two-dimensional domain in the $M_y - M_z$ plane is qualitatively shown in Fig. 3.3(c) for different values of β. In this plane, plasticity is treated as associative.

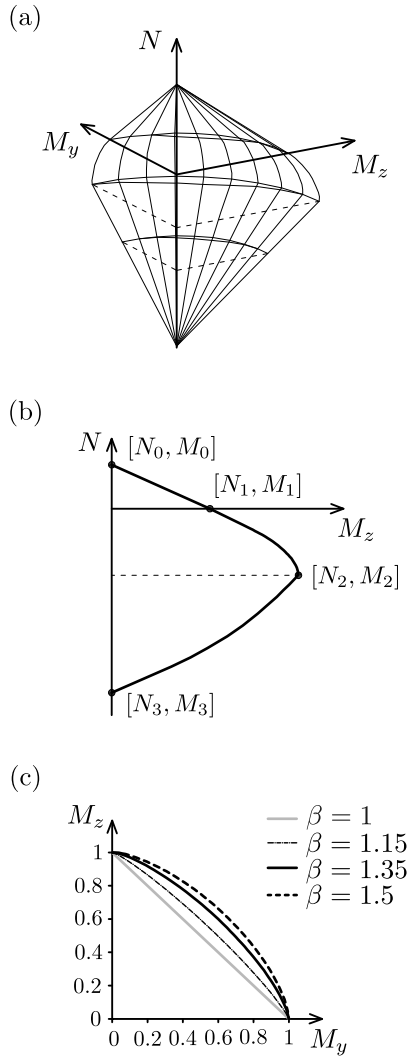

Figure 3.3: The axial force-biaxial bending interaction surface: (a) typical Bresler's surface [28], (b) activation domain in the $N - M_z$ plane, and (c) normalized activation domain in the $M_y - M_z$ plane for varying values of the exponent β.

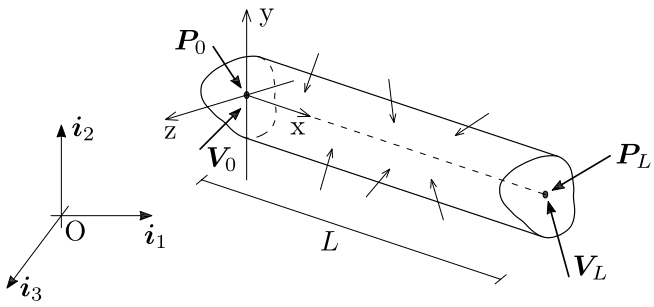

Figure 3.4: A beam subjected to external forces.

3.2.4 Weak Form of Beam Equilibrium

Let us consider, in the Euclidean space $\Re^3$ referred to the orthonormal frame (O , $\boldsymbol{i}_1$, $\boldsymbol{i}_2$, $\boldsymbol{i}_3$), a framed structure composed by straight Euler-Bernoulli beams geometrically modelled by their axes. We denote by x $\in [0, L]$ the local coordinate along the beam's axis of length L and introduce the local coordinate y and z to orient the cross-section, see Fig. 3.4.

Assuming the hypothesis of small displacements, the beam configuration is determined by the displacement vector $\hat{\boldsymbol{u}} = [u_x\ u_y\ u_z\ \varphi_x\ \varphi_y\ \varphi_z]^T$, whose components are the displacements and rotations along the three axes respectively.

Based on the Euler-Bernoulli beam theory, since the shear strains are neglected, the flexural rotations are defined as

$$\varphi_y = -u_z'(x), \qquad \varphi_z = u_y'(x). \tag{3.20}$$

With reference to Eqs. (3.20), the displacement vector $\hat{\boldsymbol{u}}$ can be rewritten as

$$\hat{\boldsymbol{u}} = \hat{\boldsymbol{B}}\boldsymbol{u}, \tag{3.21}$$

where $\boldsymbol{u} = [u_x\ u_y\ u_z\ \varphi_x]^T$ is the vector of independent displacements and

$$\hat{\boldsymbol{B}} = \begin{bmatrix} 1 & 0 & 0 & 0 \\ 0 & 1 & 0 & 0 \\ 0 & 0 & 1 & 0 \\ 0 & 0 & 0 & 1 \\ 0 & 0 & -\frac{\mathrm{d}}{\mathrm{dx}} & 0 \\ 0 & \frac{\mathrm{d}}{\mathrm{dx}} & 0 & 0 \end{bmatrix} \tag{3.22}$$

is the constraint operator.

The kinematic compatibility relations can be expressed in a compact form as

$$\boldsymbol{q} = \boldsymbol{C}\boldsymbol{u}, \tag{3.23}$$

where $\boldsymbol{q} = [e_x\ \kappa_x\ \kappa_y\ \kappa_z]^T$ is the vector of strains and

$$\boldsymbol{C} = \begin{bmatrix} \frac{\mathrm{d}}{\mathrm{dx}} & 0 & 0 & 0 \\ 0 & 0 & 0 & \frac{\mathrm{d}}{\mathrm{dx}} \\ 0 & 0 & \frac{-\mathrm{d}^2}{\mathrm{dx}^2} & 0 \\ 0 & \frac{\mathrm{d}^2}{\mathrm{dx}^2} & 0 & 0 \end{bmatrix} \tag{3.24}$$

is the kinematic compatibility operator.

The beam is subjected to the distributed loads $\boldsymbol{p} = [p_x\ p_y\ p_z\ m_x\ m_y\ m_z]^T$ and concentrated loads $(\boldsymbol{P}_0, \boldsymbol{P}_L)$ applied at the initial and final sections. As a consequence, the constraint forces $(\boldsymbol{V}_0, \boldsymbol{V}_L)$ are also acting on the initial and final sections.

The principle of virtual displacement (PVD) states that for a body to be in equilibrium, the total virtual work done by the external forces is equal to the total work done by the internal forces for any kinematically admissible configuration, i.e.

$$\int_0^L \boldsymbol{p}^T \delta\hat{\boldsymbol{u}}\, dx + (\boldsymbol{V}_0 + \boldsymbol{P}_0)^T \delta\hat{\boldsymbol{u}}_0 + (\boldsymbol{V}_L + \boldsymbol{P}_L)^T \delta\hat{\boldsymbol{u}}_L = \int_0^L \boldsymbol{Q}^T \delta\boldsymbol{q}\, dx. \tag{3.25}$$

Substituting Eqs. (3.21) and (3.23) in Eq. (3.25) yields

$$\int_0^L \boldsymbol{p}^T \hat{\boldsymbol{B}} \delta\boldsymbol{u}\, dx + (\boldsymbol{V}_0 + \boldsymbol{P}_0)^T \hat{\boldsymbol{B}} \delta\boldsymbol{u}_0 + (\boldsymbol{V}_L + \boldsymbol{P}_L)^T \hat{\boldsymbol{B}} \delta\boldsymbol{u}_L = \int_0^L \boldsymbol{Q}^T \boldsymbol{C} \delta\boldsymbol{u}\, dx. \tag{3.26}$$

Applying the additive decomposition of constraint matrix $\hat{\boldsymbol{B}}$ and compatibility matrix $\boldsymbol{C}$,

$$\hat{\boldsymbol{B}} = \hat{\boldsymbol{B}}_1 + \hat{\boldsymbol{B}}_2 = \begin{bmatrix} 1 & 0 & 0 & 0 \\ 0 & 1 & 0 & 0 \\ 0 & 0 & 1 & 0 \\ 0 & 0 & 0 & 1 \\ 0 & 0 & 0 & 0 \\ 0 & 0 & 0 & 0 \end{bmatrix} + \begin{bmatrix} 0 & 0 & 0 & 0 \\ 0 & 0 & 0 & 0 \\ 0 & 0 & 0 & 0 \\ 0 & 0 & 0 & 0 \\ 0 & 0 & -\frac{d}{dx} & 0 \\ 0 & \frac{d}{dx} & 0 & 0 \end{bmatrix}, \tag{3.27}$$

$$\boldsymbol{C} = \boldsymbol{C}_1 + \boldsymbol{C}_2 = \begin{bmatrix} \frac{d}{dx} & 0 & 0 & 0 \\ 0 & 0 & 0 & \frac{d}{dx} \\ 0 & 0 & 0 & 0 \\ 0 & 0 & 0 & 0 \end{bmatrix} + \begin{bmatrix} 0 & 0 & 0 & 0 \\ 0 & 0 & 0 & 0 \\ 0 & 0 & -\frac{d^2}{dx^2} & 0 \\ 0 & \frac{d^2}{dx^2} & 0 & 0 \end{bmatrix}, \tag{3.28}$$

to Eq. (3.26) and subsequently integrating by parts, the indefinite and boundary equilibrium equations of the Euler-Bernoulli beam are obtained as

$$(\boldsymbol{C}_2 - \boldsymbol{C}_1)^T \boldsymbol{Q} + (\hat{\boldsymbol{B}}_2 - \hat{\boldsymbol{B}}_1)^T \boldsymbol{p} = \boldsymbol{0} \quad \text{in } x \in]0, L[, \tag{3.29}$$

$$\begin{cases} \hat{\boldsymbol{B}}_1^T (\boldsymbol{V}_0 + \boldsymbol{P}_0) - \hat{\boldsymbol{B}}_2^{[1]^T} \boldsymbol{p}(0) + (\boldsymbol{C}_1^{[1]} - \boldsymbol{C}_2^{[1]})^T \boldsymbol{Q}(0) = \boldsymbol{0} \\ \hat{\boldsymbol{B}}_2^{[1]^T} (\boldsymbol{V}_0 + \boldsymbol{P}_0) + \boldsymbol{C}_2^{[2]^T} \boldsymbol{Q}(0) = \boldsymbol{0} \end{cases} \quad \text{in } x = 0, \tag{3.30}$$

$$\begin{cases} \hat{\boldsymbol{B}}_1^T (\boldsymbol{V}_L + \boldsymbol{P}_L) + \hat{\boldsymbol{B}}_2^{[1]^T} \boldsymbol{p}(L) - (\boldsymbol{C}_1^{[1]} - \boldsymbol{C}_2^{[1]})^T \boldsymbol{Q}(L) = \boldsymbol{0} \\ \hat{\boldsymbol{B}}_2^{[1]^T} (\boldsymbol{V}_L + \boldsymbol{P}_L) - \boldsymbol{C}_2^{[2]^T} \boldsymbol{Q}(L) = \boldsymbol{0} \end{cases} \quad \text{in } x = L, \tag{3.31}$$

where apex $[k]$ means k-order integration of the relative matrix.

3.3 Finite Element Formulation of the Beam

3.3.1 The Shape Functions

The closed form expression of the beam's deflection (3.4) contains integration constants c_i (with $i = 1, 2, 3, 4$) that have to be calculated by applying the boundary conditions of the beam. The following boundary conditions can be defined by assuming known values for nodal displacements u_{z_1} and u_{z_2} and nodal rotations φ_{y_1} and φ_{y_2} for the initial and final nodes,

$$u_z(0) = u_{z_1}, \quad u_z'(0) = -\varphi_{y_1}, \quad u_z(L) = u_{z_2}, \quad u_z'(L) = -\varphi_{y_2}. \tag{3.32}$$

In the absence of external load $p_z(x)$, by imposing the boundary conditions (3.32), the deflection function of the beam in Eq. (3.4) can be rewritten as

$$u_z(x) = N_{z_1}(x) u_{z_1} + N_{z_2}(x) \varphi_{y_1} + N_{z_3}(x) u_{z_2} + N_{z_4}(x) \varphi_{y_2}, \tag{3.33}$$

where N_{z_i} represent the non-standard shape functions and are explicitly given as, see [22],

$$N_{z_1}(x) = 1 - \frac{2 f_1 g_2(x) - 3L f_2 g_1(x)}{2 f_1 g_2(L) - 3L f_2 g_1(L)}, \tag{3.34a}$$

$$N_{z_2}(x) = x - L\frac{f_2 g_2(x) - 2Lf_3 g1(x)}{2f_1 g_2(L) - 3Lf_2 g_1(L)}, \tag{3.34b}$$

$$N_{z_3}(x) = \frac{2f_1 g_2(x) - 3Lf_2 g_1(x)}{2f_1 g_2(L) - 3Lf_2 g_1(L)}, \tag{3.34c}$$

$$N_{z_4}(x) = L\frac{(f_2 - 2f_1)g_2(x) - L(2f_3 - 3f_2)g_1(x)}{2f_1 g_2(L) - 3Lf_2 g_1(L)}, \tag{3.34d}$$

where f_j are defined as:

$$f_j = 1 + \frac{j}{L}\sum_{i=1}^{n}\frac{\gamma_i}{1-\gamma_i A}\Big(\frac{x_i}{L}\Big)^{j-1}, \qquad j = 1, 2, 3. \tag{3.35}$$

To exemplify, the plots of non-standard shape functions in Eqs. (3.34) are illustrated in Figs. 3.5 and 3.6 for a 500 cm long beam possessing, respectively, one and three slope discontinuities. For the sake of comparison, the Hermitian shape functions of the analogous sound beam are also included in Figs. 3.5 and 3.6.

On the basis of the assumption made for the inelastic strain vector (only plastic curvatures are considered), the axial displacement and torsion are not subjected to discontinuity and are interpolated using standard shape functions,

$$N_{x_1}(x) = 1 - \frac{x}{L}, \quad N_{x_2}(x) = \frac{x}{L}. \tag{3.36}$$

Finally, by collecting the displacements of the element nodes in the vector $\boldsymbol{d} = [\boldsymbol{d}_1\ \boldsymbol{d}_2]^T$, with $\boldsymbol{d}_1 = [u_{x_1}\ u_{y_1}\ u_{z_1}\ \varphi_{x_1}\ \varphi_{y_1}\ \varphi_{z_1}]^T$ and $\boldsymbol{d}_2 = [u_{x_2}\ u_{y_2}\ u_{z_2}\ \varphi_{x_2}\ \varphi_{y_2}\ \varphi_{z_2}]^T$, the displacement function of the beam is obtained in the form

$$\boldsymbol{u}(x) = \boldsymbol{N}(x)\boldsymbol{d}, \tag{3.37}$$

where $\boldsymbol{N}(x)$ is the total shape function matrix of the beam, which is a collection of non-standard and standard shape functions, and takes

$$\boldsymbol{N}(x) = [\boldsymbol{N}_1(x)\ \boldsymbol{N}_2(x)], \tag{3.38}$$

with

$$\boldsymbol{N}_j(x) = \begin{bmatrix} N_{x_j} & 0 & 0 & 0 & 0 & 0 \\ 0 & N_{y_{2j-1}} & 0 & 0 & 0 & N_{y_{2j}} \\ 0 & 0 & N_{z_{2j-1}} & 0 & N_{z_{2j}} & 0 \\ 0 & 0 & 0 & N_{x_j} & 0 & 0 \end{bmatrix}, \tag{3.39}$$

where $j = 1, 2$ represents the number of initial and final nodes, respectively.

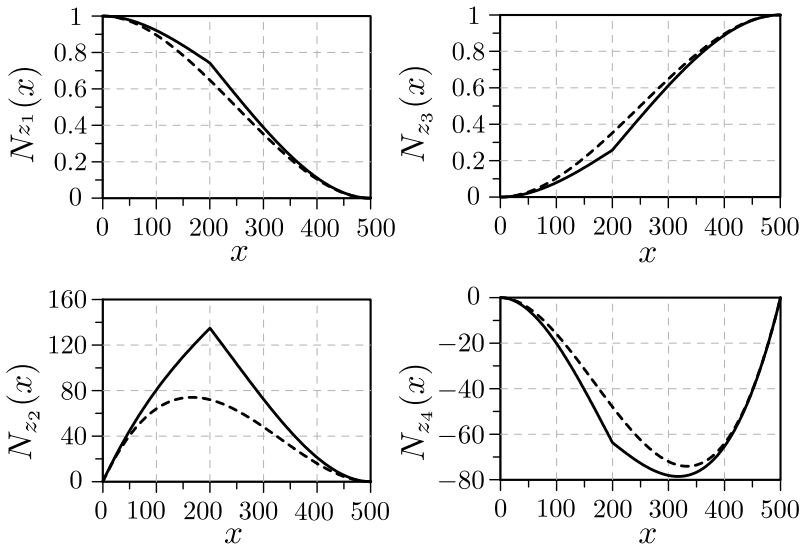

Figure 3.5: Comparison between the shape functions of a sound beam (dashed line) and the non-standard shape functions of a beam with one slope discontinuity (continuous line) with $x_1 = 200$ cm associated with $\gamma_1 = 0.4966$.

3.3.2 Stiffness Matrix and Nodal Force Vector

Let us start by recalling the PVD expression in Eq. (3.25) in the absence of boundary constraints,

$$\int_0^L \boldsymbol{p}^T \delta\hat{\boldsymbol{u}}\, dx + \boldsymbol{P}_0^T \delta\hat{\boldsymbol{u}}_0 + \boldsymbol{P}_L^T \delta\hat{\boldsymbol{u}}_L = \int_0^L \boldsymbol{Q}^T \delta\boldsymbol{q}\, dx. \tag{3.40}$$

The constitutive law (3.9) can be rewritten to include inelasticity as,

$$\boldsymbol{Q} = \boldsymbol{\Phi}\boldsymbol{q}, \tag{3.41}$$

with $\boldsymbol{\Phi} = diag[E(x)S \quad G(x)I_x(x) \quad E(x)I_y(x) \quad E(x)I_z(x)]$ in which S and $G(x)$ are defined as the area of the section and the shear stiffness respectively. Introducing it together with the kinematic constraint (3.21) in (3.40), the PVD expression takes the following form

$$\int_0^L \boldsymbol{p}^T \hat{\boldsymbol{B}} \delta\boldsymbol{u}\, dx + \boldsymbol{P}_0^T\, \hat{\boldsymbol{B}}\, \delta\boldsymbol{u}_0 + \boldsymbol{P}_L^T\, \hat{\boldsymbol{B}}\, \delta\boldsymbol{u}_L = \int_0^L \boldsymbol{q}^T \boldsymbol{\Phi} \delta\boldsymbol{q}\, dx. \tag{3.42}$$

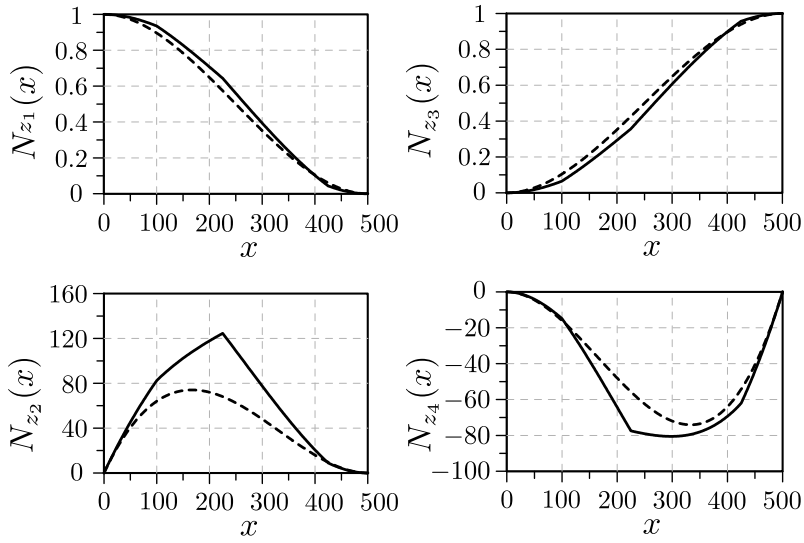

Figure 3.6: Comparison between the shape functions of a sound beam (dashed line) and the non-standard shape functions of a beam with three slope discontinuities (continuous line) with $x_1 = 100$ cm, $x_2 = 225$ cm and $x_3 = 425$ cm, associated with, respectively, $\gamma_1 = 0.4940$, $\gamma_2 = 0.4960$ and $\gamma_3 = 0.4940$.

Linking Eq. (3.37) to Eq. (3.23), the strain vector can be written as

$$\boldsymbol{q} = \boldsymbol{B}\boldsymbol{d}, \tag{3.43}$$

with

$$\boldsymbol{B} = \boldsymbol{C}\boldsymbol{N}(x). \tag{3.44}$$

Substituting the kinematic relations (3.37) and (3.43) into the PVD equation (3.40) yields

$$\delta\boldsymbol{d}^T\Big[\int_0^L \boldsymbol{B}^T\boldsymbol{\Phi}\boldsymbol{B}\boldsymbol{d}\,dx - \int_0^L \boldsymbol{N}^T\hat{\boldsymbol{B}}^T\boldsymbol{p}\,dx - \boldsymbol{P}\Big] = 0, \tag{3.45}$$

with

$$\boldsymbol{P} = \boldsymbol{N}(0)\hat{\boldsymbol{B}}\boldsymbol{P}_0 + \boldsymbol{N}(L)\hat{\boldsymbol{B}}\boldsymbol{P}_L. \tag{3.46}$$

It should be noted from Eq. (3.45) that the nodal force vector $\boldsymbol{P}$ maintains the equilibrium with the distributed load $\boldsymbol{p}$ when $\boldsymbol{d} = \boldsymbol{0}$.

The beam element equilibrium equation in the classical form is easily obtained from Eq. (3.45) as

$$\boldsymbol{k}\boldsymbol{d} = \boldsymbol{f} + \boldsymbol{P}, \tag{3.47}$$

where $\boldsymbol{k}$ and $\boldsymbol{f}$ are the stiffness matrix and equivalent nodal force vector respectively, owning the following expressions

$$\boldsymbol{k} = \int_0^L \boldsymbol{B}^T\boldsymbol{\Phi}\boldsymbol{B}\,dx, \tag{3.48a}$$

$$\boldsymbol{f} = \int_0^L \boldsymbol{N}^T\hat{\boldsymbol{B}}^T\boldsymbol{p}\,dx. \tag{3.48b}$$

The stiffness matrix of the beam element in presence of slope discontinuities can be derived in closed from, see [22]. In the case of a two-dimensional beam in the x-z plane, the stiffness matrix of the beam is formulated as

$$\boldsymbol{k} = \frac{E_0 I_0}{L^3 f_0} \begin{bmatrix} \frac{f_a L^2 S}{I_0} & 0 & 0 & -\frac{f_a L^2 S}{I_0} & 0 & 0 \\ 0 & 12f_1 & 6Lf_2 & 0 & -12f_1 & 6Lf_b \\ 0 & 6Lf_2 & 4L^2 f_3 & 0 & -6Lf_2 & 2L^2 f_c \\ -\frac{f_a L^2 S}{I_0} & 0 & 0 & \frac{f_a L^2 S}{I_0} & 0 & 0 \\ 0 & -12f_1 & -6Lf_2 & 0 & 12f_1 & -6Lf_b \\ 0 & 6Lf_b & 2L^2 f_c & 0 & -6Lf_b & 4L^2[3(f_1 - f_2) + f_3] \end{bmatrix}, \tag{3.49}$$

where

$$f_a = 4f_1f_2, \quad f_b = 2f_1 - f_2, \quad f_c = 3f_2 - 2f_3, \quad f_0 = 4f_1f_3 - 3f_2^2. \tag{3.50}$$

It is worth showing the vector of nodal forces $\boldsymbol{f}$ for the case where the vector of distributed loads $\boldsymbol{p}$ is constant. By adopting the following substitutions

$$H_i = \prod_{\substack{j=1 \\ j\neq i}}^{n}(-1 + A\gamma_j)(L - x_i)\gamma_i U(L - x_i), \tag{3.51}$$

$$\Pi_i = \prod_{i=1}^{n}(-1 + A\gamma_i), \tag{3.52}$$

and

$$D = 12\left[\frac{1}{6}\Pi_i(2f_1 - 3f_2)L^3 + \sum_{i=1}^{n} H_i(f_2L - 2f_1x_i)\right], \tag{3.53}$$

the force vector $\boldsymbol{f}$ is obtained as

$$\boldsymbol{f} = \left[p_x\frac{L}{2} \quad p_z(L - h_1) + m_y \quad p_z(\frac{L^2}{2} - h_2) + m_y(-L + h_3) \right.$$
$$\left. p_x\frac{L}{2} \quad p_zh_1 - m_y \quad p_zh_4 - m_yh_5\right]^T, \tag{3.54}$$

where

$$h_1 = \frac{6}{D}\left[\frac{1}{6}\Pi_i(f_1 - 2f_2)L^4 + \sum_{i=1}^{n} H_i(L - x_i)(f_2L - 2f_1x_i)\right], \tag{3.55a}$$

$$h_2 = \frac{2L}{D}\left[\frac{1}{12}\Pi_i(3f_2 - 8f_3)L^4 + \sum_{i=1}^{n} H_i(L - x_i)(2f_3L - 3f_2x_i)\right], \tag{3.55b}$$

$$h_3 = \frac{4L}{D}\left[\frac{1}{2}\Pi_i(f_2 - 2f_3)L^3 + \sum_{i=1}^{n} H_i(2f_3L - 3f_2x_i)\right], \tag{3.55c}$$

$$h_4 = \frac{2L}{D}\Bigg[-\frac{1}{12}\Pi_i(6f_1 - 15f_2 + 8f_3)L^4 + \sum_{i=1}^{n} H_i(L - x_i)\Big(2f_3L + 6f_1x_i - 3f_2(L + x_i)\Big)\Bigg], \quad (3.55d)$$

$$h_5 = \frac{4L}{D}\Bigg[\Pi_i(f_1 - 2f_2 + f_3)L^3 + \sum_{i=1}^{n} H_i\Big(2f_3L + 6f_1x_i - 3f_2(L + x_i)\Big)\Bigg]. \quad (3.55e)$$

The explicit expressions of $\boldsymbol{k}$ and $\boldsymbol{f}$ can be simply expanded for three-dimensional case by adding the components of x-y plane without any additional requirement.

3.4 FEM Procedure

To investigate the nonlinear response of reinforced concrete frames, the new beam element has been inserted in a FE analysis program written in MATLAB code. The complete FEM procedure involves mainly three stages: data-gathering stage, incremental elastic stage, and incremental plastic stage. In the data-gathering stage, information is collected about the geometry of the structure, material properties, reinforcement configuration of the sections, and FEM meshing. The stiffness matrices and force vectors of all elements are assembled to construct the global ones. A static load pattern, e.g. distributed load or nodal force, is set to run the pushover analysis. In the elastic stage of the analysis, the load is applied to the model and incrementally increased until the formation of the first plastic sections, for which the stresses are above the yielding limit. At this point, the plastic stage of the FEM procedure, which follows a Newton-Raphson scheme, begins. This stage constitutes the main part of the FEM procedure and is illustrated in the flow chart of Fig. (3.7).

In the FEM procedure presented here, the full external load is applied at each step rather than its increment. Once the load increment is assigned, the global force vector $\boldsymbol{F}_{n+1}$ is updated, while the global stiffness matrix $\boldsymbol{K}_{n+1}$ is set to the converged one from the previous step $\boldsymbol{K}_n$. At this point, the global equilibrium equation at iteration $j = 1$ of step $n + 1$,

$$\boldsymbol{K}^1_{n+1}\boldsymbol{U}^1_{n+1} = \boldsymbol{F}^1_{n+1}, \quad (3.56)$$

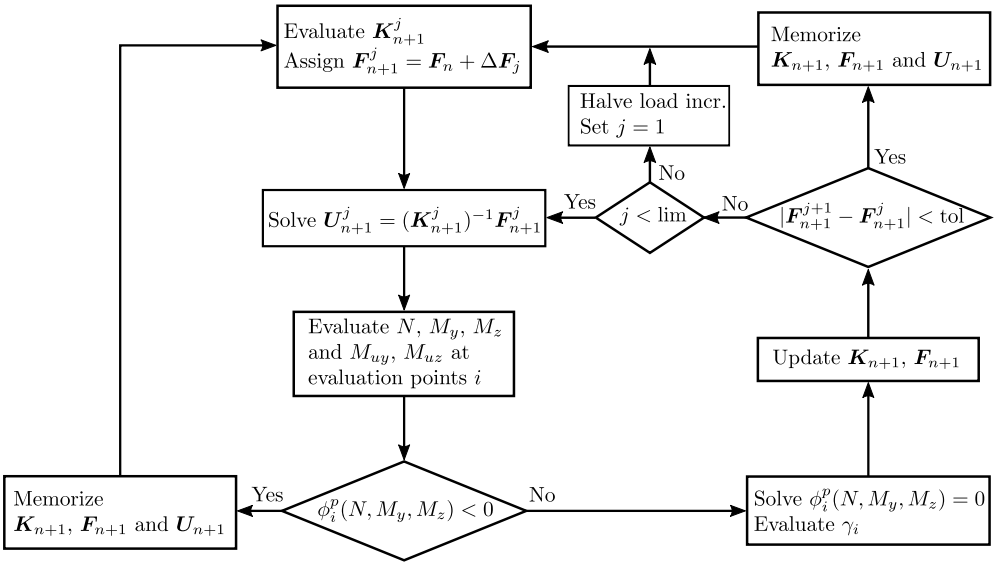

Figure 3.7: Flowchart of the plastic stage in the FEM procedure.

is solved for the global vector of nodal displacements $\boldsymbol{U}^1_{n+1}$, by prescribing the displacements and rotations of constrained nodes. It is necessary to note here that since the presented FEM procedure is conditionally convergent, the numerical accuracy and stability of the procedure are guaranteed by choosing a sufficiently small load increment, which can also provide a good computational efficiency.

A post-processing phase permits to calculate internal forces and displacements of the structure. The model requires the assignment, for each structural element, of a fixed number of evolution points. This choice depends on the user's preference based on the accuracy of the numerical results as well as the time of evaluation. It should be remarked that the proposed numerical tool, when just two evaluation points are fixed at the ends of the members, represents the classic lumped plasticity model, which is only able to capture the end plastic hinges.

According to the level of axial force, dimensions of the cross-section and the material properties, the moment capacities of the sections are evaluated and condition (3.14), rewritten in the form of (3.18), is checked. If plasticity is detected in a particular section, the closest point projection algorithm, as described in Section 3.4.1, is used to calculate the "corrected" values of bending

moments and plastic multiplier that makes the loading-unloading conditions (3.17) again satisfied at the section level. The values of bending moments at the plastic sections are corrected by calibrating the γ_i parameters, which represent singularity intensities in Eq. (3.1).

The evaluation of γ_i parameters involves the solution of a nonlinear system of equations, which is provided in sub-Section 3.4.2. This system is numerically solved by means of the classic iterative Newton-Raphson method. Having the calibrated γ_i parameters, the global stiffness matrix and the global force vector of the structure are updated and used to calculate the global nodal displacement vector $\boldsymbol{U}_{n+1}^{j}$ if the global convergence condition

$$\left| \boldsymbol{F}_{n+1}^{j+1} - \boldsymbol{F}_{n+1}^{j} \right| < \text{tol}, \tag{3.57}$$

is not reached.

During the iterations, the plastic hinges positions are not memorized as long as the condition (3.57) is not holding. When the model reaches a converged state, plastic hinges become permanent. In this case, the global stiffness matrix and global force and displacement vectors are memorized. In particular, the global stiffness matrix is assigned for the first iteration of the next step. If the number of iterations exceeds a limit value, the load increment is halved for and the evaluation restarts for the same step. The procedure continues over subsequent load increments; more plastic sections are found and the RC model is modified to incorporate new formed hinges. The procedure stops when a collapse mechanism occurs or when the target displacement is reached.

3.4.1 Closest Point Projection

The closest point projection method [159] is employed as the stress return algorithm to rectify the state variables, so as to satisfy the loading-unloading conditions. In the case of detecting a plastic section, the stress vector identifies a point outside the activation domain. This point must be corrected back to the limit surface to produce a null value for the activation function. Here, the implicit Backward Euler scheme is adopted. Assuming that the state of the section is known at step n of the analysis, the constitutive relation (3.9), including the decomposition of strains (3.10), can be written in a discretized form as

$$\boldsymbol{Q}_{n+1} = \boldsymbol{\Phi}_0(\boldsymbol{q}_n + \Delta\boldsymbol{q} - \boldsymbol{q}_n^p - \Delta\boldsymbol{q}^p). \tag{3.58}$$

Defining the trial internal forces as

$$\boldsymbol{Q}_{n+1}^{\text{trial}} = \boldsymbol{\Phi}_0(\boldsymbol{q}_n + \Delta\boldsymbol{q} - \boldsymbol{q}_n^p), \tag{3.59}$$

and substituting the discrete counterpart of the flow rules (3.2.2),

$$\Delta\boldsymbol{q}^p = \Delta\lambda^p \frac{\partial\phi^p}{\partial\boldsymbol{Q}}, \tag{3.60}$$

Eq. (3.58) can be rewritten as

$$\boldsymbol{Q}_{n+1} = \boldsymbol{Q}_{n+1}^{\text{trial}} - \Delta\lambda^p\boldsymbol{\Phi}_0\frac{\partial\phi^p}{\partial\boldsymbol{Q}}. \tag{3.61}$$

When the trial internal force vector makes the activation function positive, the correction phase comes into the action and the following system is solved

$$\begin{cases} \boldsymbol{Q}_{n+1}^{\text{trial}} = \boldsymbol{Q}_{n+1} + \Delta\lambda^p\boldsymbol{\Phi}_0\frac{\partial\phi^p}{\partial\boldsymbol{Q}} \\ \phi^p(\boldsymbol{Q}_{n+1}) = 0 \end{cases}. \tag{3.62}$$

Linearizing the system of equations (3.62) around the solutions $\boldsymbol{Q}_{n+1}$ and $\Delta\lambda^p$ gives

$$\begin{cases} \boldsymbol{Q}_{n+1}^{\text{trial}} = \boldsymbol{Q}_{n+1}^i + \delta\boldsymbol{Q} + (\delta\lambda + \Delta\lambda^{p,i})\boldsymbol{\Phi}_0\frac{\partial\phi^p}{\partial\boldsymbol{Q}} + \Delta\lambda^{p,i}\boldsymbol{\Phi}_0\frac{\partial^2\phi^p}{\partial\boldsymbol{Q}^2}\delta\boldsymbol{Q} \\ \phi^p(\boldsymbol{Q}_{n+1}^i) + \frac{\partial\phi^p}{\partial\boldsymbol{Q}}\delta\boldsymbol{Q} = 0 \end{cases}, \tag{3.63}$$

where $\delta\boldsymbol{Q}$ and $\delta\lambda$ indicate the variation of the vector $\boldsymbol{Q}$ and the plastic multiplier $\Delta\lambda^p$ between two subsequent iterations and superscript i refers to the iteration number.

Expressing Eq. (3.63) in matrix form, one obtains

$$\begin{bmatrix} \boldsymbol{\Phi}_0^{-1} + \Delta\lambda^{p,i}\frac{\partial^2\phi^p}{\partial\boldsymbol{Q}^2} & \frac{\partial\phi^p}{\partial\boldsymbol{Q}} \\ \frac{\partial\phi^p}{\partial\boldsymbol{Q}} & 0 \end{bmatrix} \begin{bmatrix} \delta\boldsymbol{Q} \\ \delta\lambda \end{bmatrix} = \begin{bmatrix} \boldsymbol{\Phi}_0^{-1}(\boldsymbol{Q}_{n+1}^{\text{trial}} - \boldsymbol{Q}_{n+1}^i) - \Delta\lambda^{p,i}\frac{\partial\phi^p}{\lambda\boldsymbol{Q}} \\ -\phi^p(\boldsymbol{Q}_{n+1}^i) \end{bmatrix}. \tag{3.64}$$

Solving Eq. (3.64) for $\delta\boldsymbol{Q}$ and $\delta\lambda$, the updated approximations of the above unknowns in iteration $i+1$ are evaluated as

$$\boldsymbol{Q}_{n+1}^{i+1} = \boldsymbol{Q}_{n+1}^i + \delta\boldsymbol{Q} \tag{3.65a}$$

$$\Delta\lambda^{p,i+1} = \Delta\lambda^{p,i} + \delta\lambda, \tag{3.65b}$$

3.4.2 Calibration of γ_i Parameters

Calibration of γ_i parameters is an important part in the proposed FEM procedure. γ_i parameters play a significant role in updating the global stiffness matrix and global force vector during the iterative process. In addition, they are responsible for keeping the values of bending moments of the plastic sections inside the admissible range.

The calibration of γ_i parameters can be performed after the identification of plastic sections and the correspondent bending moments. The general expression of the bending moment $M_y(x)$ in the case of two-dimensional problem in x-z local reference system is obtained by substituting (3.7) into (3.2),

$$M_y(x) = -E_0 I_0 \Big(2c_3(\gamma_i) + 6c_4(\gamma_i) + \frac{p_z^{[x]}(x)}{E_0 I_0} \Big). \tag{3.66}$$

where c_3 and c_4 are functions of γ_i parameters and are determined after the imposition of the boundary conditions (3.32), using the known values of nodal displacements. After some mathematical manipulation, c_3 and c_4 are obtained as

$$c_3(\gamma_i) = \frac{-a_1 g_2(L) + a_2 g_2'(L)}{g_1(L) g_2'(L) - g_2(L) g_1'(L)}, \tag{3.67a}$$

$$c_4(\gamma_i) = \frac{a_1 g_1(L) - a_2 g_1'(L)}{g_1(L) g_2'(L) - g_2(L) g_1'(L)}, \tag{3.67b}$$

where

$$a_1 = (\varphi_{y1} - \varphi_{y2}) + \frac{p_z^{[3]}(0) - p_z^{[3]}(L)}{E_0 I_0} - \sum_{i=1}^{n} \frac{\gamma_i}{1 - \gamma_i A} \frac{p_z^{[2]}(x_i)}{E_0 I_0} U(L - x_i), \tag{3.68a}$$

and

$$a_2 = (u_{z2} - u_{z1}) + \frac{p_z^{[4]}(0) - p_z^{[4]}(L)}{E_0 I_0} + \varphi_{y1} L + L \frac{p_z^{[3]}(0)}{E_0 I_0} + \\ - \sum_{i=1}^{n} \frac{\gamma_i}{1 - \gamma_i A} \frac{p_z^{[2]}(x_i)}{E_0 I_0} (L - x_i) U(L - x_i). \tag{3.68b}$$

When a plastic section is detected at x_0, the following function is built

$$\Gamma_0(x_0, \gamma) = M_y(x_0) + E_0 I_0 \Big(2c_3(\gamma) + 6c_4(\gamma) x_0 + \frac{p_z^{[2]}(x_0)}{E_0 I_0} \Big) = 0, \tag{3.69}$$

where $M_y(x_0)$ is a known value.

In the case of formation of n plastic sections, Eq. (3.69) constitutes a nonlinear system $\mathbf{\Gamma} = 0$ of n equations with n unknowns γ_i, which is solved by means of a local iterative Newton-Raphson scheme where at iteration $k+1$ the updated vector of γ_i parameters is calculated as

$$\gamma_{i_{k+1}} = \gamma_{i_k} + \Delta\gamma_i, \tag{3.70}$$

where

$$\Delta\gamma_i = -\boldsymbol{J}^{-1}(\gamma_{i_k})\mathbf{\Gamma}(\gamma_{i_k}), \tag{3.71}$$

with

$$\boldsymbol{J} = \frac{\mathrm{d}\Gamma}{\mathrm{d}\gamma_\mathrm{i}}. \tag{3.72}$$

3.5 Numerical Applications

Three two-dimensional numerical applications are included herein to show the capabilities of the proposed FEM procedure. The aim of carrying out the numerical applications is to reflect the following aspects:

- Validation of the program with an experimental test performed on an RC frame.
- The geometry of the structure and the incremental load pattern can affect the position of the plastic hinges.
- The variation of steel reinforcement configurations in a beam changes the capacity of the sections and consequently affects the position of the plastic hinges. This is likely to happen for the buildings that have been designed based on old building provisions, by merely considering vertical loads.

In the first example, an experimental two-dimensional portal frame is simulated. For the second and third examples, respectively, a portal frame with an inclined column, and a 2-story frame under horizontal seismic action is considered. In the latter cases, the cross-sections dimensions and steel reinforcements have been designed in such a way to reproduce possible real cases.

Material	E_0 [MPa]	f_{ck} [MPa]	f_{yd} [MPa]	ν
Concrete	22400	22	–	0.15
Steel	210000	–	450	0.30

Table 3.1: Material mechanical properties adopted for the numerical applications 2 and 3.

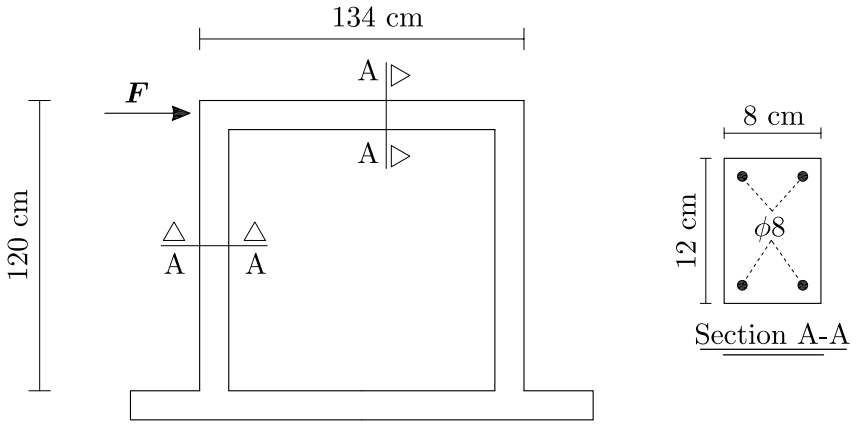

Figure 3.8: Geometry and reinforcement details of the experimental test of Paul and Agrawal [137].

All the structures have been meshed considering each structural element, beam or column, as a single finite element with a fixed number of evaluation points. The mechanical properties of concrete and steel reinforcements in the second and third examples are reported in Table 3.1. All the analyses have been performed under load control until the formation of a failure mechanism.

3.5.1 Simulation of an Experimental Test

In this example, the proposed numerical tool is validated by reproducing the pushover experimental curve reported by Paul and Agrawal [137] for an RC frame with geometry and reinforcement details as illustrated in Fig. 3.8. Mechanical properties of concrete and reinforcement steels are according to the Indian Standard [74]. The concrete is of grade M20 with an elastic modulus equal to 22400 MPa. FE-415 grade steel bars are used as the reinforcements.

The frame is pushed by a horizontal in-plane load applied through a hy-

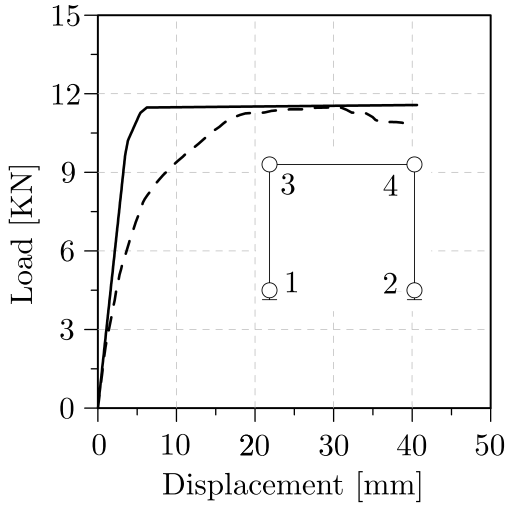

Figure 3.9: The comparison of pushover curves of the numerical (dashed line) and experimental of Paul and Agrawal [137] (solid line).

draulic displacement controlled actuator on its top-left corner. The experimental load-displacement curve is plotted as a dashed line in Fig. 3.9.

The numerical model consists of three elements. Because of the simplicity of the structure, the uniformity of the sections, and also the nature of the applied incremental load, only two sample points are chosen at the ends of each element.

The numerical load-displacement curve is plotted in Fig. 3.9 and is compared with the experimental one. The model successfully predicts the initial stiffness and ultimate load capacity of the experimental outcome. Obviously, as it commonly happens for the lumped plasticity models, the model is not able to reproduce the entire load-displacement curve as a fiber model does. The evolution of the plastic hinges at corners is also demonstrated in Fig. 3.9.

3.5.2 RC Portal with One Inclined Column

The case under study consists in a two-dimensional RC frame, as depicted in Fig. 3.10(a). In order to demonstrate the influence of structural geometry on the evolution of plastic hinges, one column is inclined at 45 degrees. The geometry and reinforcement details of the cross-sections are shown in Fig. 3.10(b). The activation domains of the beam columns are provided in Fig. 3.11. For

conducting the nonlinear analysis, the frame is subjected to incremental vertical loads on its beam element. 25 evaluation points are fixed for the beam, while two evaluation points are chosen for the columns, located at their ends.

Figure 3.12 shows the load-displacement curve of the nonlinear analysis. The load levels, at which the plastic hinges are formed, are indicated on the curve. At the end of the elastic branch, the first plastic hinge appears on the leftmost section of the beam. The second hinge takes place again on the beam, but 208 cm away from its right end. The last two hinges evolve at the base of the columns, first on the left column and then on the right column. As soon as the fourth plastic hinge appears in the structure, the collapse mechanism is reached and the structure becomes unstable.

The diagrams of axial force and bending moment at the formation of the first plastic hinges are shown in Fig. 3.13, where the positions of hinges are also specified on the frame. The correspondent deformed shapes of the frame are given in Fig. 3.14. Figure 3.15 shows the evolution of γ_i parameters as a function of the incremental distributed load p. As it is evident, after an initiation, the values of γ_i tend to the limit value $1/A$.

3.5.3 2-Story Gravity-Designed Frame

This numerical example concerns a 2-story RC frame with one bay. Figure 3.16(a) shows the layout of the frame together with the applied loads. Constant vertical loads are uniformly distributed over the beam elements. Monotonically increasing horizontal loads are considered at the beam levels, having increasing intensity with height. In the bottom story, the structural elements have 35×35 cm^2 sections, while in the top story, 30×30 cm^2 sections are assigned to structural elements. Figure 3.16(b) displays the details of the cross-sections. Steel reinforcements are designed considering the structure subjected to vertical static loads only, to simulate the general case of existing structures built without seismic provisions. 33 evaluation points are mapped on the beams, whereas 2 evaluation points are considered for the columns at the extreme nodes.

The aim of the current numerical application is to demonstrate that the structural elements may end up with a bending moment diagram for which their sections are not designed. As a result, the critical points of the structure do not necessarily locate at expected sections and unanticipated plastic hinges affect the stability of the structure.

The analysis is performed with increments of the force $\Delta F = 100$ N, starting from a zero horizontal force up to the force wherein the collapse mechanism is

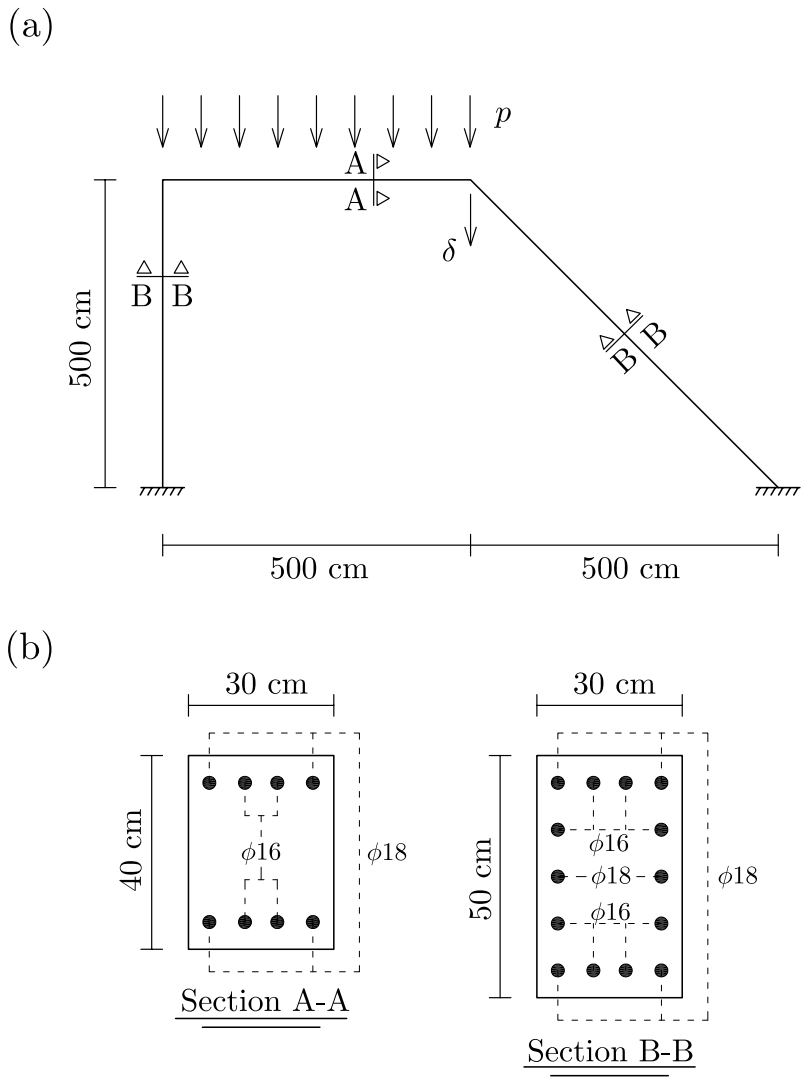

Figure 3.10: The RC frame of numerical example 2: (a) geometry and (b) cross-sections.

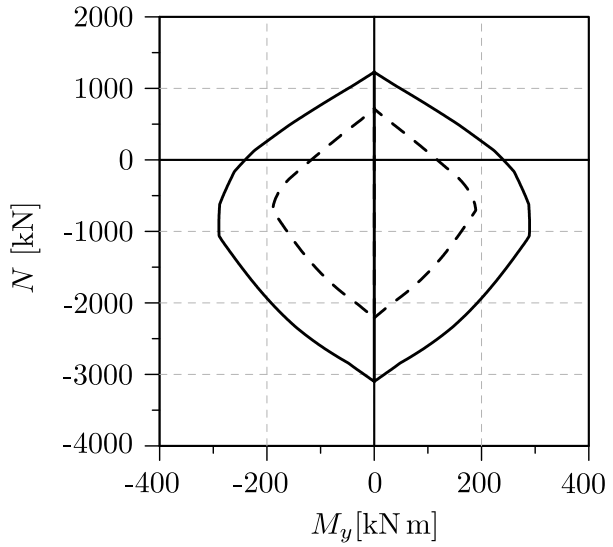

Figure 3.11: The activation domain of the beam (dashed line) and columns (solid line) in numerical example 2.

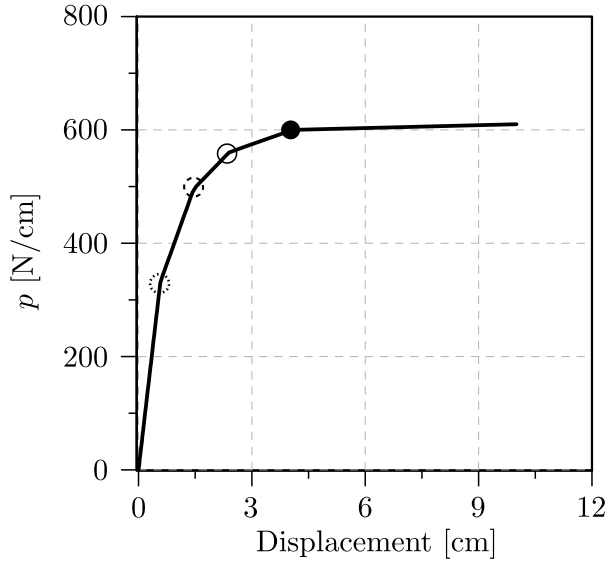

Figure 3.12: The load-displacement curve of numerical example 2.

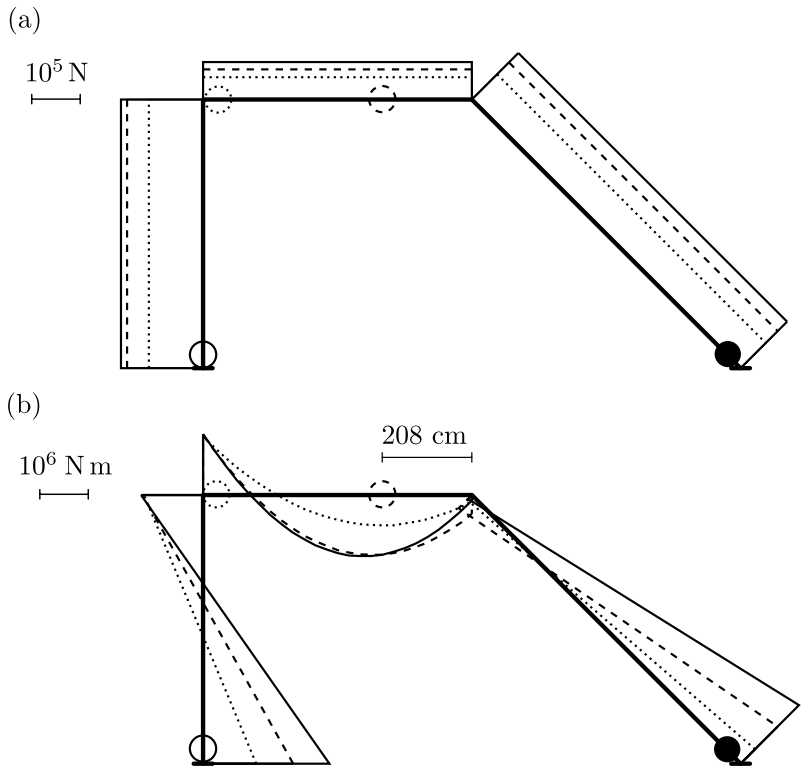

Figure 3.13: The diagrams of (a) axial force and (b) bending moment for numerical example 2.

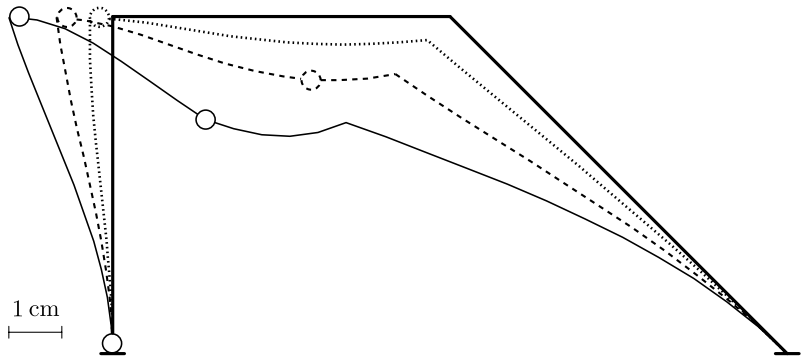

Figure 3.14: The deformed shapes of the frame in numerical example 2.

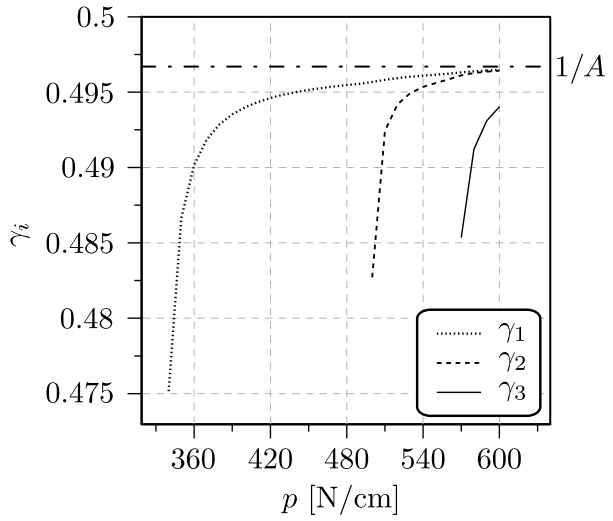

Figure 3.15: The evolution of γ_i parameters in numerical example 2.

formed. In the ultimate step of the analysis, 6 plastic hinges are generated in the model, among which two are located inside the span of the beams. This is due to the non-uniformity of the reinforcement distribution in the sections that follows the old building regulations and leads to smaller activation domain in the contraflexure points of the beams. In Fig. 3.17, the plastic hinge pattern of the proposed model is compared with the results of a conventional analysis. The conventional analysis is carried out employing a classic lumped plasticity model. In this case, as it is shown in Fig. 3.17(b), the hinges are only allowed to evolve at the ends of the elements, which has also influenced the evolution pattern of plastic hinges. The load-displacement curves of both analyses are plotted in Fig. 3.18, where also the results of an adaptive plastic hinge approach and a force-based fiber model approach are given.

The result of the adaptive approach in Fig. 3.18 is obtained by modifying the proposed FE procedure in order to include the adaptive mesh refinement method proposed by Izzuddin and Elnashai in [79], see Section 2.3.3.1 for a brief description of the adaptive approach. The adaptive approach, in the framework of the proposed formulation, brings up more complexities to the model. The latter is due to the fact that in the adaptive approach once the plasticity is detected, the element is divided in two parts, which not only offers more degrees of freedom to the model but also increases the number of evaluation points. This

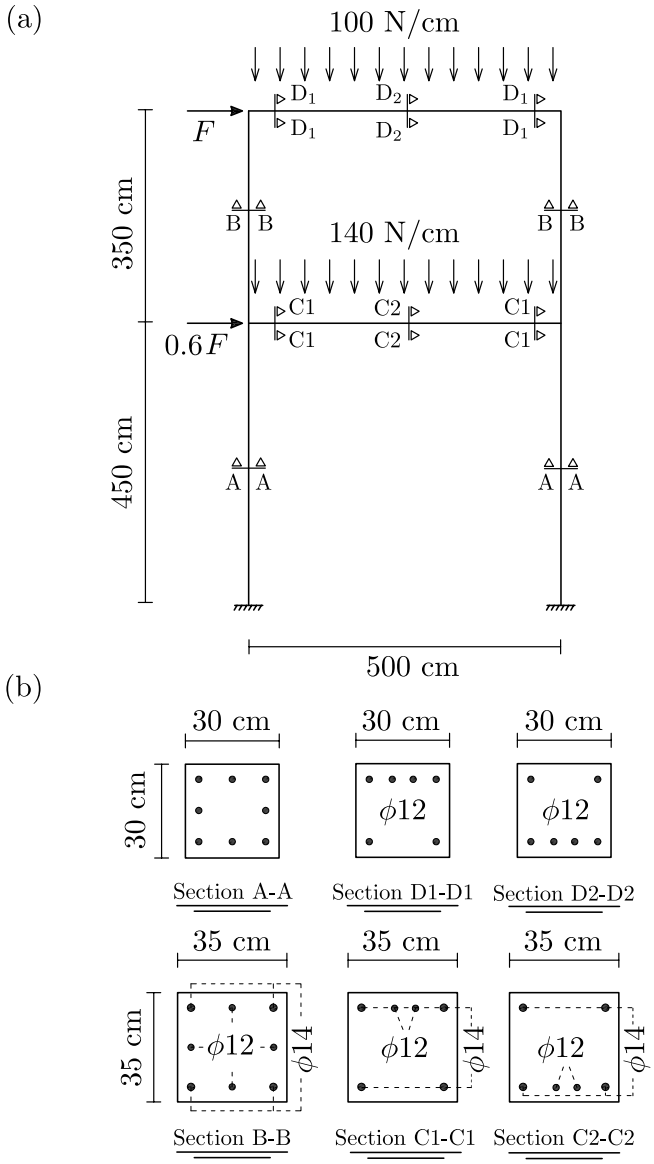

Figure 3.16: 2-story frame of numerical example 3: (a) geometry and (b) cross-sections.

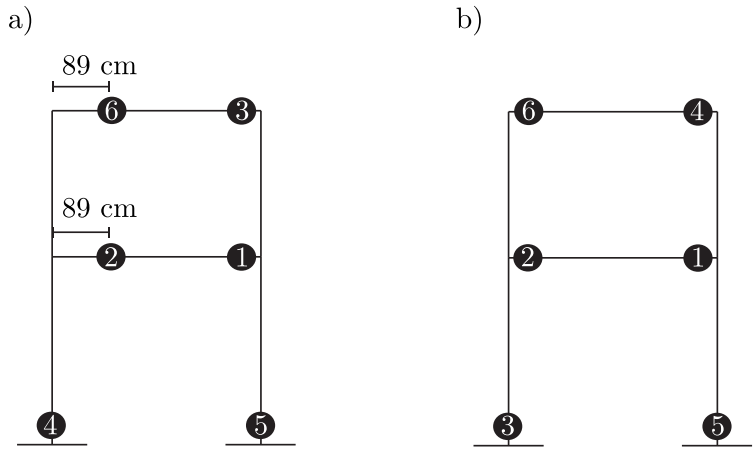

Figure 3.17: The plastic hinge pattern of numerical example 3 for the proposed FE model (a) and a conventional FE model (b).

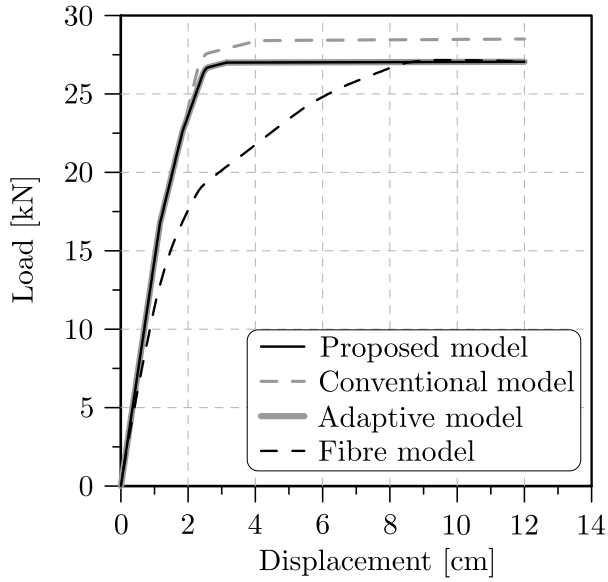

Figure 3.18: Comparison between the load-displacement curve of the proposed model and other models in numerical example 3.

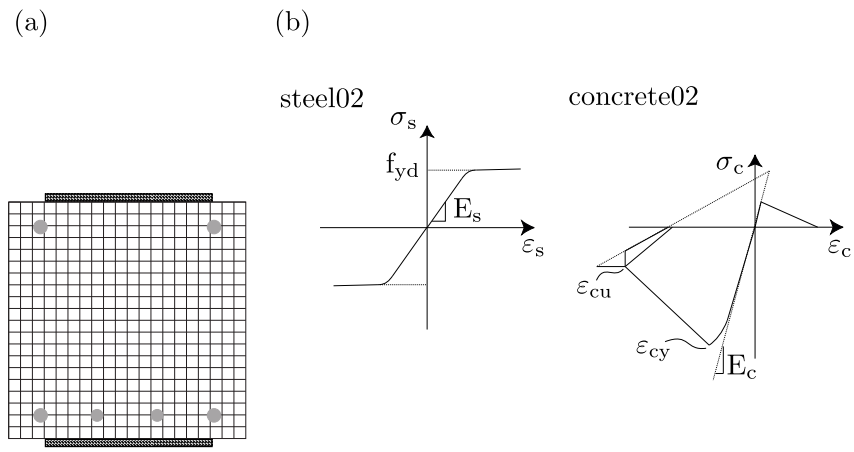

Figure 3.19: Details of the fiber section built in OpenSees, including (a) the cross-sections' discretization and (b) the stress-strain constitutive law of the materials.

fact is confirmed in this numerical example as the adaptive approach is 33% more computationally expensive with respect to the proposed approach.

The result of the force-based fiber model approach in Fig. 3.18 is obtained through an analysis in the OpenSess code [119], which performs nonlinear analysis based on different plasticity frameworks using fiber sections. The cross-sections of the elements are descritized into 400 rectangular fibers, see Fig. 3.19(a). Concrete and steel are modelled using the material models available in the OpenSess library. More specifically, concrete is modelled by Concrete02 material model, which considers the Kent-Scott-Park [86] behaviour in compression and an elastic with linear softening behaviour in tension. Steel reinforcements are modelled by Steel02 material, which uses the Giuffre-Menegetto-Pinto model [123], implementing an elasto-plastic law with hardening in both tension and compression. The constitutive behaviour of the models are shown in Fig. 3.19(b).

It is clear from Fig. 3.18 that the proposed model provides the same initial stiffness and ultimate load of the force-based fiber model. The same is also true for the adaptive approach. This confirms the efficiency of the proposed model. On the other hand, the conventional analysis overestimates the overall capacity of the structure and may not lead to an optimal retrofitting strategy for the seismic assessment of existing structures. The comparison of the results of numerical example 3 with the results of fiber model with different elements,

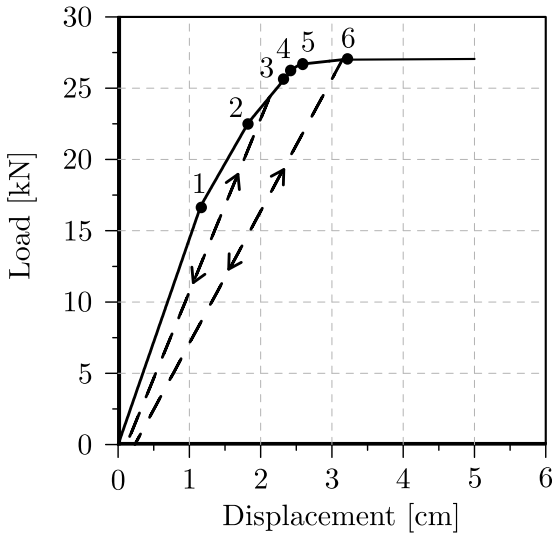

Figure 3.20: Load-displacement curve of numerical example 3 including unloading branches.

i.e. Force-Based Element, Displacement-Based Element and Beam With Hinges is made in Chapter 4.

Numerical example 3 was re-run by using the proposed approach only to show the behaviour of the model in unloading. Two unloading stations are considered, one after the formation of the second plastic hinge and the other before the formation of the sixth plastic hinge. The load-displacement curve including the unloading branches is shown in Fig. 3.20. The slope of the two unloading-reloading branches furnishes information about the accumulated damage in the structure concentrated at plastic sections. It is important to note that the effect of crack closure, i.e. plastic hinge in relaxed condition, is not necessary to be taken into consideration in this numerical example, because the signs of the bending moments associated with plastic sections remain unchanged during the loading-unloading cycle. This possible effect is discussed later in Section 5.4.

The evolution of γ_i parameters is depicted in Fig. 3.21. It is immediate that the hinges possessing growing values of γ_i parameters are disposed to become perfect hinges as the analysis proceeds.

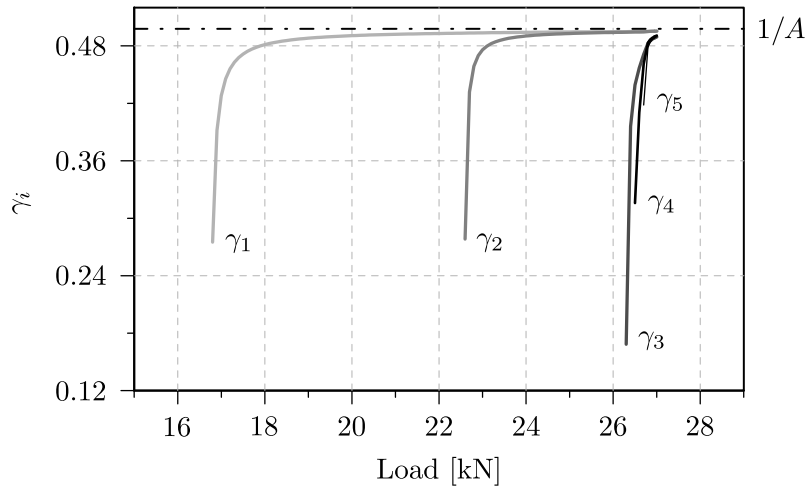

Figure 3.21: Evolution of γ_i parameters in numerical example 3.

3.6 Conclusions

The implementation of the Euler-Bernoulli beam element endowed with multiple slope discontinuities in a FE code is presented in this chapter. The enhanced beam has been developed on the base of non-standard shape functions derived from the closed form solutions suggested by Biondi and Caddemi [22].

The new Euler-Bernoulli beam element has been formulated in the framework of lumped plasticity model and has been used to predict the structural performance of RC structures where internal plastic hinges appear. Flow rules are postulated on the basis of a thermodynamical approach considering an associated plasticity theory. A Bresler's type failure surface with a correction of the exponent has been defined to control the development of plasticity. Inelastic curvatures have been derived imposing the classic loading-unloading conditions. For each step of the analysis, an elastic predictor-plastic corrector procedure is followed. In the plastic steps, the latter is done using the closest point projection algorithm.

The model is validated by comparing its outputs with those obtained from experimental test on a real RC frame. Other two numerical applications are carried out to demonstrate how the evolution pattern of plastic hinges can change in a structure depending on its geometry, the nature of the incremental load, and the steel reinforcement distribution of the cross-sections.

It is demonstrated that the proposed FEM permits the formation of plastic hinges in any position of the beam, without suffering from the problem of mesh refinement, as in the case of most diffused commercial softwares. It is also observed that a conventional lumped plasticity model may overestimate the overall capacity of the structure. The proposed model, instead, gives the same results of an adaptive mesh refinement approach in a less computational time and, moreover, achieves equal stiffness and ultimate load capacity of a force-based fiber model.

The model can be interpreted as an example of Smart Displacement Based (SDB) beam element, as originally proposed by by Pantó et al. [134].

Chapter 4

Nonlinear Analysis of RC Frames Retrofitted by FRP Composites

4.1 Introduction

The application of Externally Bonded Fiber Reinforced Polymer (EB-FRP) composites to RC structural members is nowadays a quite common retrofitting technique that offers unique advantages compared to traditional techniques, such as good immunity to corrosion, low weight, excellent mechanical properties and easy adaptability to the shape of the element.

The EB-FRP technique has been proved to be capable in enhancing the structural performance of RC structures, as it has found many different applications for strengthening various structural elements, such as beams, columns, slabs and shear walls. The continuous increasing development of the EB-FRP applications have drawn the attention to the study of the mechanical contribution provided by FRP reinforcement for different failure mechanisms. In the following, a brief literature review is presented addressing the use of EB-FRP composite as a retrofitting technique for RC structures.

One of the first pilot studies on this topic was carried out by Mayo et al. [116], who studied the application of EB-FRP composites for retrofitting full-scale RC bridges. In the literature, particular attention is devoted to the experimental investigation of RC flexural members externally strengthened using FRP composites. Kachlakev and McCurry [84] studied the effect of Carbon

FRP (CFRP) and Glass FRP (GFRP) for, respectively, compensating flexural and shear deficiencies of RC beams. Camata et al. [32] investigated the brittle mechanism of RC beams and slabs flexurally strengthened with FRP composites. Both studies have shown that while higher load capacities are obtained through the use of EB-FRP composite, lower ductilities are observed. This observation, nevertheless, was not verified in the early study of Chajes et al. [38], who investigated the effect of EB-FRP composites on the flexural capacity of RC beams. To this end, RC beams externally bonded with FRP composites were four-point flexurally loaded up to the failure level and the results were compared with the beams with additional steel reinforcements. It was shown by the authors that higher flexural stiffness and capacity were obtained through the use of FRP composites without any loss of ductility. In addition to the study by Chajes et al. [38], Mahini and Ronagh [113] showed that a suitable configuration of FRP composites is able to improve the ductility of a brittle RC structure by means of modifying the plastic hinge pattern in a ductile manner.

As a complementary part of the experimental works, many numerical and analytical studies are available in this field, while few of them have reported the effect of EB-FRP composites on the behaviour of seismically deficient RC structures. Zou et al. [184] studied a three-story gravity-designed RC frame retrofitted by means of FRP wrapping of the columns. It was highlighted that the FRP confinement is able to change the mode of failure of the structure by allowing the formation of plastic hinges in the beams and increasing the strength of the columns. Niroomandi et al. [129] performed nonlinear static pushover analysis on EB-FRP retrofitted RC structure, which was primarily reinforced by steel bracing. In their model, the moment-rotation relations of the joints, before and after EB-FRP retrofitting, were obtained using FE analysis. The pushover capacity curve of the analysis was then compared to the experimental one of Mahini and Ronagh [114]. It was shown that the application of the EB-FRP composite increases the structural ductility in a more efficient manner with respect to steel bracing technique. A recent application of EB-FRP can also be found in the work of Ronagh and Eslami [152], where an eight-story frame whose beams and columns were flexurally strengthened by CFRP composites was modelled. The results demonstrated the efficiency of EB-FRP retrofitting in improving the lateral strength of the frame.

This Chapter is devoted to the modelling of RC frame flexurally retrofitted by EB-FRP composites. The model is an extension of the FEM procedure presented in Chapter 3. The FEM procedure is modified here to account the presence of EB-FRP composites in RC sections.

The case study regards the two-story gravity-designed RC frame presented in Section 3.5.3. The frame is flexurally retrofitted by EB-FRP composites with the aim to evaluate the efficiency of the EB-FRP retrofitting technique. It is to be pointed out that the EB-FRP retrofitting here only concerns the flexural strengthening of the beams, while retrofitting the joints or columns is not the intention of the current study.

The strength domains of the EB-FRP retrofitted sections are defined according to Italian Guideline CNR-DT 200 R1 [76], which was the reference of many studies in the literature (see e.g. Ombres [131] or Mohamed and Khattab [125]).

To summarize, the novelty of this chapter of the thesis lies in the modification of the RC failure domain of the model presented in Chapter 3 by taking into consideration the effect of FRP composites using the method proposed by CNR-DT 200 R1 [76].

The results achieved by the proposed FEM procedure are then compared with those obtained using OpenSees code [119]. In particular, comparisons are made with different element formulations available in OpenSees (e.g. Force-Based Element, Displacement-Based Element and Beam With Hinges Element), showing the sensitivity of these formulations to different parameters and the efficacy of the proposed FEM procedure in assessing the lateral behaviour of EB-FRP strengthened structures.

4.2 Analysis of EB-FRP Retrofitted RC Section

Past studies have demonstrated that in addition to the classic failure mechanism of RC section, the following mechanisms (see e.g. Meier [122], Camata et al. [32], El-Mihilmy and Tedesco [57]) should be considered for the EB-FRP retrofitted RC beam:

- rupture of the FRP composite,
- interfacial debonding of the EB-FRP composite,
- debonding of the EB-FRP composite at the extreme sections.

These mechanisms, which are called the non-classic mechanisms, must be incorporated into the definition of the failure surface of the cross-section in order to correctly predict the ultimate load designed for the element. For this to be achieved, the analysis of the EB-FRP retrofitted RC section is performed by

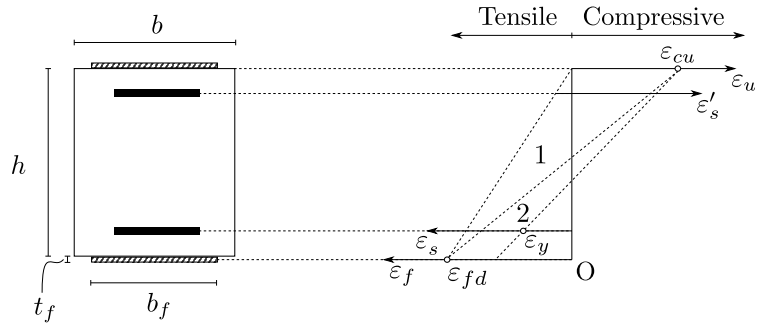

Figure 4.1: Strain distribution of the EB-FRP retrofitted RC section.

setting the ultimate strain of the FRP composite ε_{fd} equal to the strain value given by the dominant failure case.

4.2.1 The Failure Surface

In an EB-FRP retrofitted RC section, the strain distribution diagram is mainly divided into two regions, see Fig. 4.1. Based on the level of axial force N acting on the section, the region of neutral axis is determined, following by the calculation of the exact location of the neutral axis, in an iterative procedure, using the force equilibrium equation of the section. If the neutral axis falls in region 1, the analysis continues by fixing the strain of the FRP composite bonded to the tensile side of the section to the ultimate FRP strain. Since strain compatibility is assumed between the adjacent components of the composite section, the strain state of the other components can be calculated adopting a linear distribution, see Fig. 4.1. On the other hand, if the neutral axis falls in region 2, the analysis continues assuming the top fibers strain of the concrete to be equal to the ultimate compressive strain, 0.35% as suggested by Italian Building Code [75]. Hence the strain of the other components are calculated. Afterwards, the ultimate resisting bending moment of the section M_{uy}, in the x-z plane, is computed by setting the moment equilibrium of the section around the position of the neutral axis (for a more detailed discussion, the reader is referred to the study of Rafiq and Southcombe [145]). At this point, the generation of the failure surface follows the same procedure as described in Section 3.2.3.

4.2.2 The Ultimate Strain of FRP

As stated above, the ultimate strain of the FRP composite ε_{fd} depends on the dominant failure mechanism. Here, the procedure presented by Italian Guideline CNR-DT 200 R1 [76] is adopted for the calculation of ε_{fd}. If the section under analysis is located in the EB-FRP effective bond zone l_{ed} (see Eq. (4.1)), FRP rupture and end debonding of EB-FRP composite are the existing failure mechanisms. While if the sections does not fall in l_{ed}, FRP rupture and EB-FRP composite interfacial debonding should be considered.

The effective bond zone of EB-FRP is calculated as

$$l_{ed} = \min\Big\{\frac{s_u}{2\gamma_{RD}\sqrt{\Gamma_{fd}}}\sqrt{\frac{\pi^2}{2}E_f t_f}\ ,\ 200(mm)\Big\}, \tag{4.1}$$

where $s_u = 0.25$ mm is the ultimate slip, E_f is the modulus of elasticity of FRP, t_f is the FRP thickness, $\gamma_{RD} = 1.25$ is a correction factor, and Γ_{fd}, which is called the fracture energy, takes the form

$$\Gamma_{fd} = \frac{k_b k_G}{FC}\sqrt{f_{cm} f_{ctm}}, \tag{4.2}$$

where FC is the confidence factor of the concrete, k_G is the correction factor obtained from experimental results, f_{cm} and f_{ctm} are, respectively, the mean values of the concrete compressive and tensile strength, and k_b is a geometrical coefficient that is calculated as (see Chen and Teng [40])

$$k_b = \sqrt{\frac{2 - \frac{b_f}{b}}{1 + \frac{b_f}{b}}} \geq 1, \tag{4.3}$$

where b_f is the width of the EB-FRP composite.

Depending on the position of the section, the ultimate strain of FRP is obtained as

$$\varepsilon_{fd} = \min\Big(\frac{\varepsilon_{fk}}{\gamma_f}\eta_a\ ,\ \varepsilon_{fdd} = \frac{f_{dd}}{E_f}\Big), \quad \text{(if section falls in } l_{ed}\text{)} \tag{4.4a}$$

$$\varepsilon_{fd} = \min\Big(\frac{\varepsilon_{fk}}{\gamma_f}\eta_a\ ,\ \varepsilon_{fdd_2} = \frac{f_{dd_2}}{E_f}\Big), \quad \text{(if section does not fall in } l_{ed}\text{)} \tag{4.4b}$$

where ε_{fk} is the ultimate nominal strain of FRP for rupture, γ_f and η_a are the material coefficient and environmental factor respectively, and f_{dd} and f_{dd_2} are defined as

$$f_{dd} = \frac{1}{\gamma_{f,d}} \sqrt{\frac{2E_f \Gamma_{fd}}{t_f}}, \tag{4.5a}$$

$$f_{dd_2} = \frac{k_q}{\gamma_{f,d}} \sqrt{\frac{E_f}{t_f} \frac{2k_b k_{G,2}}{FC} \sqrt{f_{cm} f_{ctm}}}, \tag{4.5b}$$

where $\gamma_{f,d}$ represents a partial safety factor, k_q represents a load distribution coefficient and $k_{G,2}$ represents a correction factor.

4.3 Numerical Application

The case under study is the two-story gravity-designed RC frame presented in Section 3.5.3. In order to retrofit the frame, CFRP composites are selected and applied to the top and bottom sides of the beam elements, see Fig. 4.2. It should be noted that in this numerical application, only the mid-span of the beams are retrofitted, i.e. the implementation of the FRP composites are done in such a way to eliminate the possibility of hinge formation along the mid-span of the beams by transferring them to beam/column joints. The stress-strain constitutive behaviour and the mechanical properties of concrete and steel are assumed as in numerical example 3.5.3, see Fig. 3.2 and Table 3.1. The constitutive behaviour and material characteristics of FRP composites are shown in Fig. 4.3.

To evaluate the lateral capacity of the EB-FRP retrofitted frame as well as the effectiveness of the retrofitting technique, the proposed FEM procedure of the previous Chapter is extended to analyse the EB-FRP retrofitted RC sections. The rest of the FEM procedure is the same as described in Section 3.4.

4.3.1 Results of the Numerical Application

Figure 4.4 shows the evolution of plastic hinges in both bare and retrofitted frames. In the case of retrofitted frame, the plastic hinges, as was expected, do not evolve along the mid-span of the elements and are shifted to the beam/column

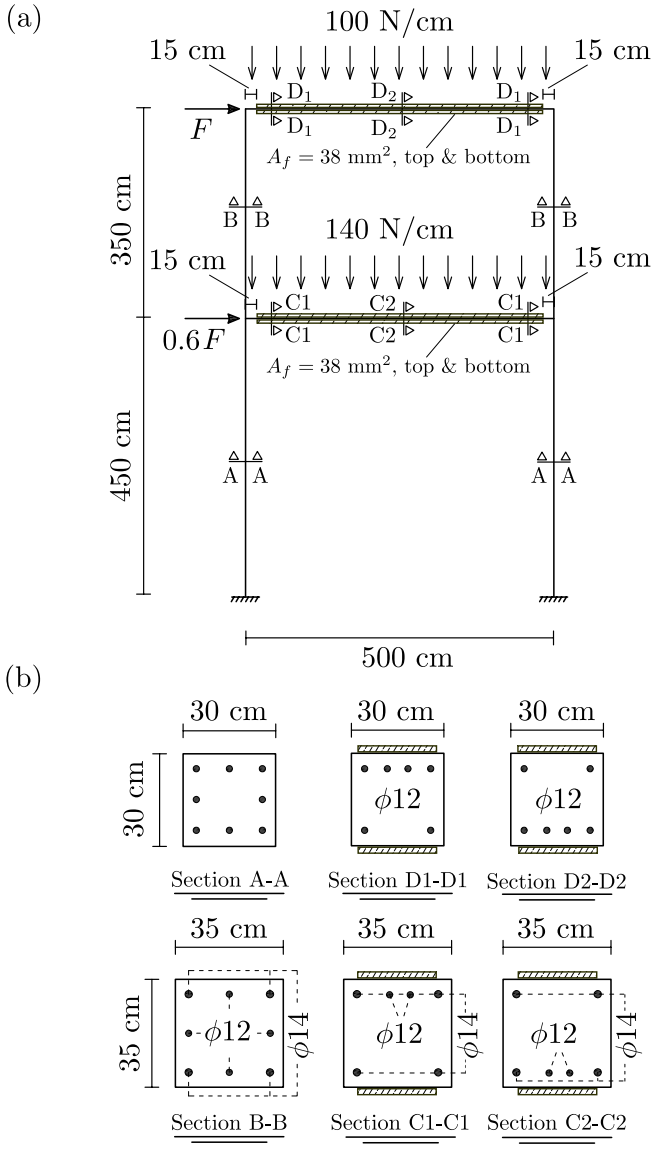

Figure 4.2: EB-FRP retrofitted RC frame: (a) geometry and (b) cross-sections.

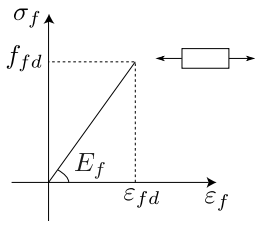

$E_f = 245000$ MPa
$f_{fd} = 3560$ MPa

Figure 4.3: Stress-strain constitutive behaviour and the mechanical properties of the FRP composite in the EB-FRP retrofitted RC frame.

joints, leading to an overall increment of the lateral load capacity. The load-displacement curves of the frames are depicted in Fig. 4.5. Since the first plastic hinge forms at the right-end of the first floor beam, the load-displacement curves of the frames are overlapped up to the load level where the second plastic hinge, which is located along the mid-span (0.89 m from the left-end) of the first floor beam, appears in the bare frame. On the other hand, for the EB-FRP retrofitted frame, the second plastic hinge evolves at the left-end of the first floor beam. This transference of the plastic hinges, which also occurs for the second floor beam, not only increases the overall capacity of the EB-FRP retrofitted frame, but also influences the pattern of the plastic hinge evolution, see Figs. 4.4 and 4.6.

It is also important to observe the trend of γ_i parameters as a function of the lateral load F. As Fig. 4.6 demonstrates, the values of γ_i, as the analysis proceeds, tend to the limit values of $1/A$.

4.3.2 Verification of the Results with OpenSees

The validation of the analyses results are carried out using OpenSees code. In order to test the applicability of the proposed model, the comparisons are made using different types of elements that are available in the OpenSees library. Force-Based Element (FBE) and Displacement-Based Element (DBE) are implemented to spread the inelasticity along the elements. In the former, the formulation is exact and is based on the equilibrium equations, the section forces are calculated by interpolating the element basic forces, the precision of the solutions mainly depends on the number of integration points, and con-

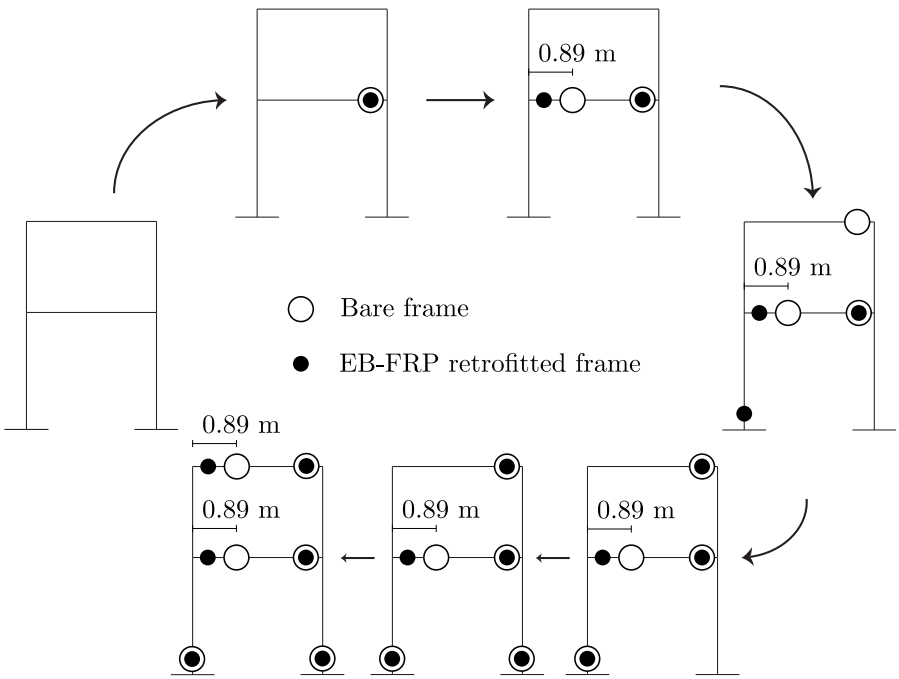

Figure 4.4: The evolution pattern of plastic hinges in the bare and EB-FRP retrofitted frames.

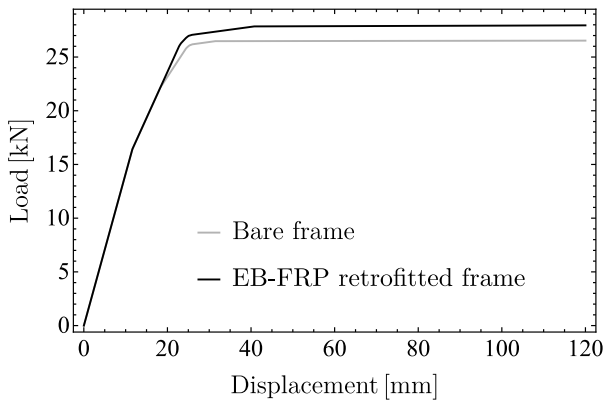

Figure 4.5: Load-displacement curves of the bare and EB-FRP retrofitted frames.

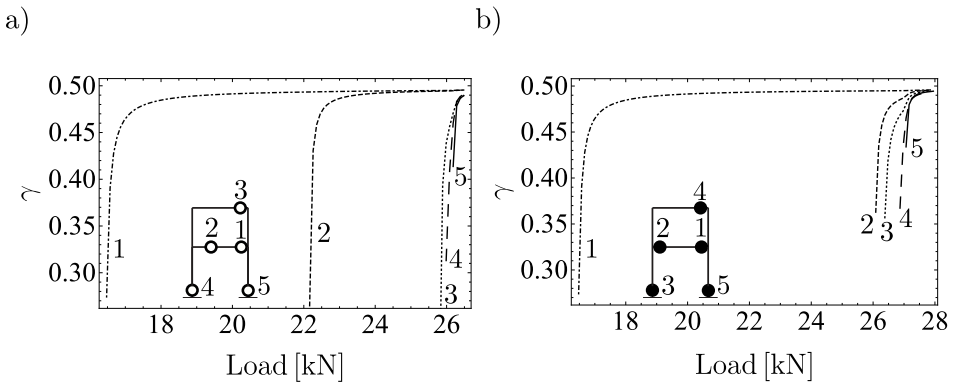

Figure 4.6: Evolution of γ_i parameters for bare frame (a) and EB-FRP retrofitted frame (b).

sequently the local and global responses converge fast. While in the latter, displacement shape functions are constructed in order to interpolate the displacement along the element. Subsequently, stiffness matrix and force vector are derived. In this case, the precision of the solution greatly depends on the number of element's mesh, which increases the computational cost and, as a result, entails slower convergence to the exact solutions. The pertinent properties of FBE and DBE are demonstrated by Neuenhofer and Filippou [128] through a comparative study. Beam With Hinges element, on the contrary, enforces the inelasticity, in a finite length, at the extreme sections of the element. This element is utilized to compare the results of the proposed model with a fiber model in which inelasticity is limited to end segments.

In all OpenSees simulations performed here, the cross-sections of the elements are discretized into 400 rectangular fibers. Concrete is modelled by Concrete02 material model and steel reinforcements are modelled by Steel02 material, see Fig. 3.19. Lastly, the FRP composite material is modelled with a linear pure brittle material in tension.

To begin the comparison, the activation domains of the first floor beam for the bare and EB-FRP retrofitted frames are built in OpenSees code and the domains are compared with those of the proposed model, see Fig. 4.7. The objective of this comparison is twofold: 1) to exhibit the effect of EB-FRP retrofitting on the overall capacity of the sections and 2) to determine the validity of the activation domains given by the proposed model. The comparison shows a good agreement for bare and EB-FRP retrofitted sections. It should

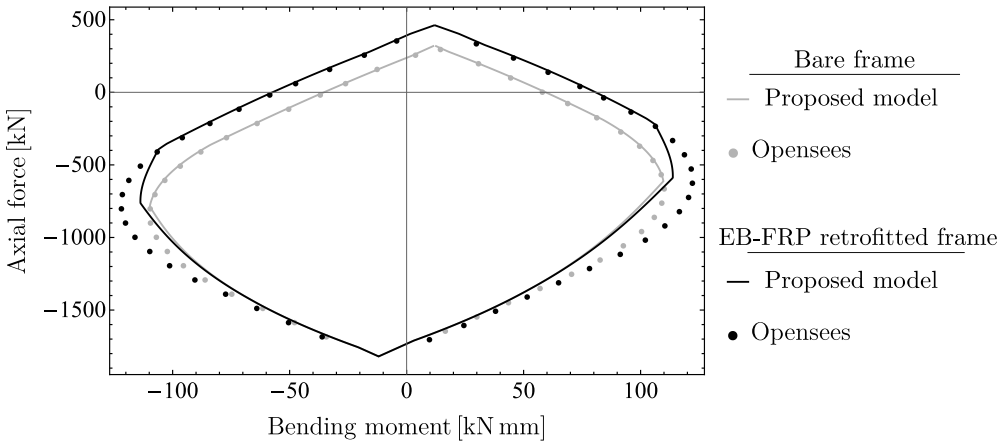

Figure 4.7: The activation domains of the first floor beam in the numerical application.

be noted that for those values of axial force for which the concrete nonlinearity plays a significant role in the ultimate resisting bending moment, a discrepancy exists between the results of the proposed model and OpenSees simulation. This discrepancy is due to the difference in the constitutive behaviour of the concrete used in the proposed model and OpenSees simulations.

For the verification of the pushover analyses results, three different models are built and simulated in OpenSees, each with a different type of element, i.e. FBE, DBE and Beam With Hinges. The results plotted in Fig. 4.8 indicate that the load-displacement curves of the proposed models are in good agreements with those of OpenSees with distributed plasticity. In case of the OpenSees model with Beam With Hinges elements, since plasticity is only concentrated at extreme segments of the elements, the results of bare and EB-FRP retrofitted frames are identical. This is because the model does not take into account the different steel reinforcement distribution along the beam span, and the effect of EB-FRP retrofitting. The comparisons in Fig. 4.8 reveals that the proposed model, despite being based on the concentrated plasticity framework, is capable of predicting the lateral capacity of RC frames, bare and EB-FRP retrofitted, as well as the efficiency of the EB-FRP retrofitting technique. These, in general, are only achievable by running fiber analysis with high computational cost.

Figures 4.9 and 4.10 depict the accuracy of the load-displacement curves generated by FBE and DBE OpenSees models with different number of inte-

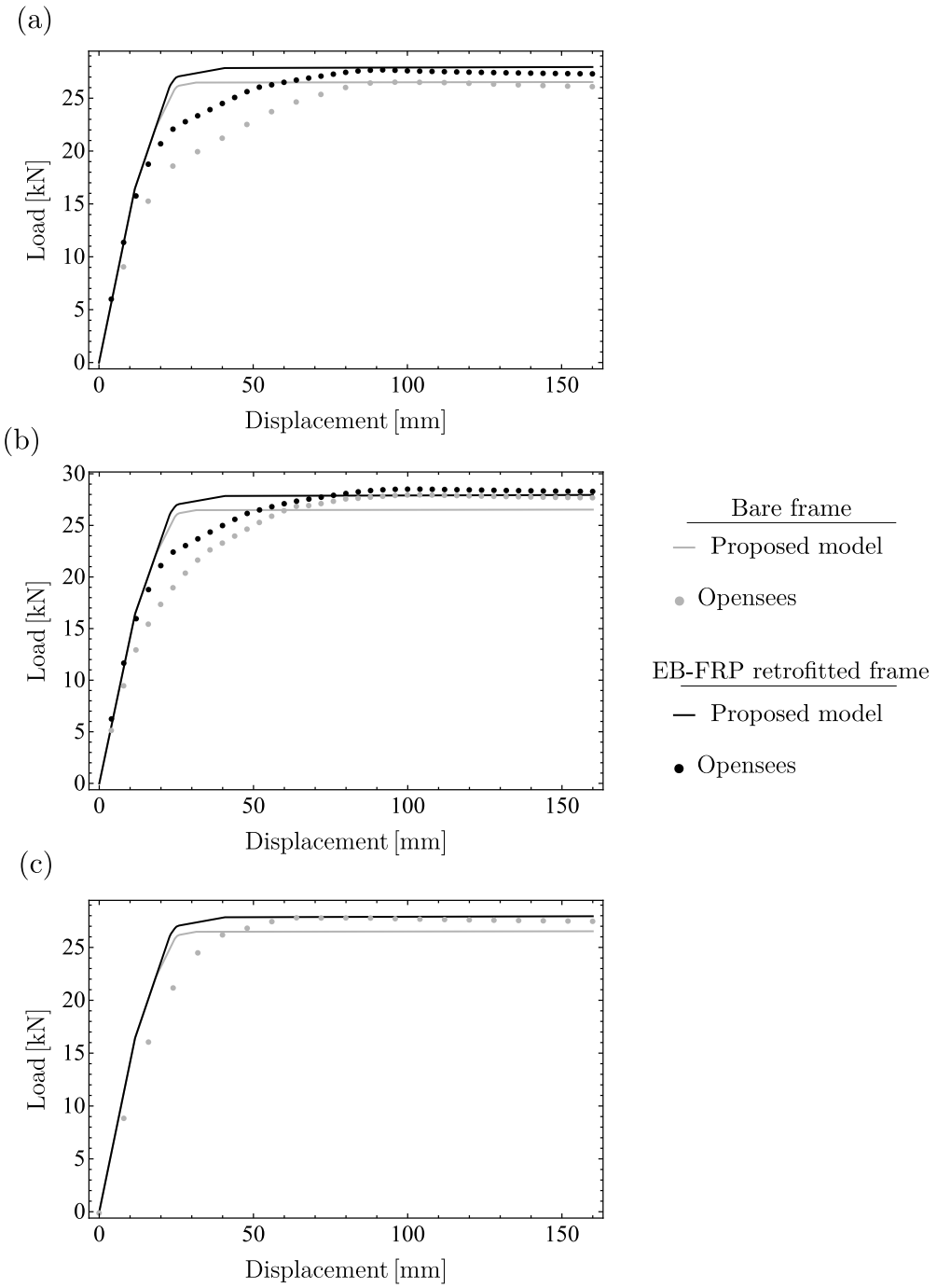

Figure 4.8: The comparison of the load-displacement curves of the proposed model with those of OpenSees with (a) FBE, (b) DBE and (c) Beam With Hinges elements.

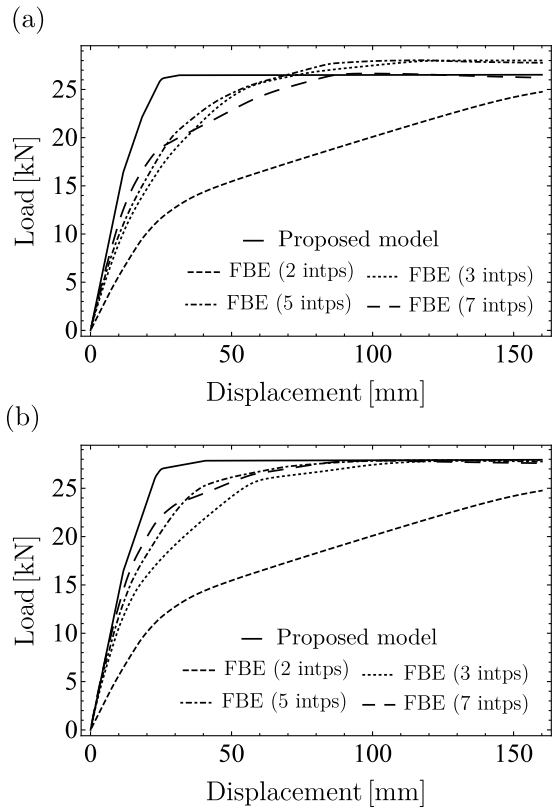

Figure 4.9: The load-displacement curves of FBE models with different number of integration points for (a) bare and (b) EB-FRP retrofitted frames.

gration points (intps) and different number of sub-elements (elts), respectively. The accuracy of the FBE models can be ameliorated by increasing the number of integration points, while in case of DBE models, acceptable accuracy is indeed reachable by dividing the elements into a sufficient number of sub-elements.

To better understand the accuracy and also the convergence of the OpenSees solutions towards the exact ones, the error bars of the ultimate lateral load are illustrated in Figs. 4.11 and 4.12 using the following expression

$$e(\%) = 100\left|\frac{F}{F_R} - 1\right|, \tag{4.6}$$

where F_R is the reference lateral load, defined as the ultimate lateral load of the

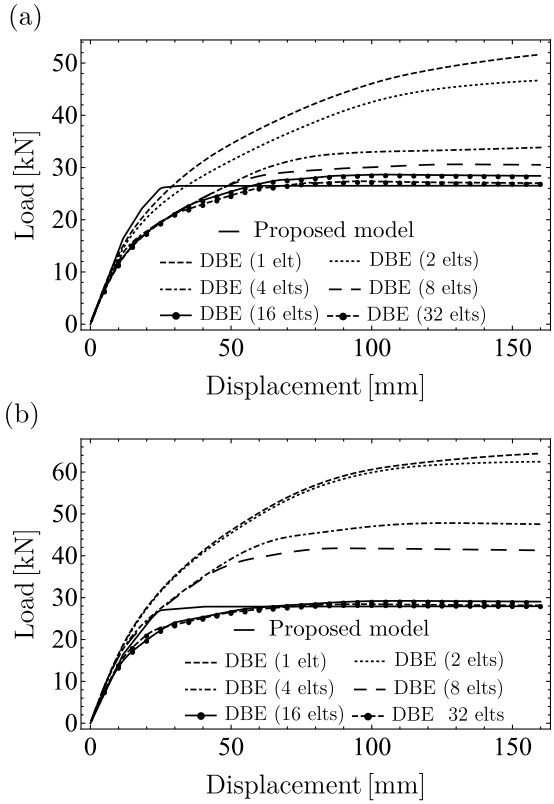

Figure 4.10: The load-displacement curves of DBE models with different number of sub-elements for (a) bare and (b) EB-FRP retrofitted frames.

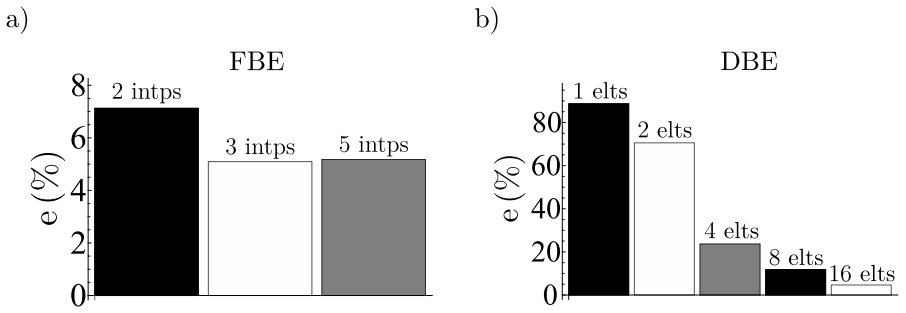

Figure 4.11: Ultimate lateral load error bars of FBE (a) and DBE (b) OpenSees models for bare frames.

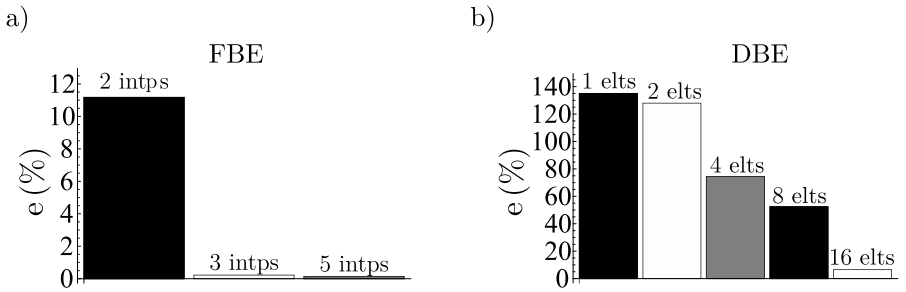

Figure 4.12: Ultimate lateral load error bars of FBE (a) and DBE (b) OpenSees models for EB-FRP retrofitted frames.

model with 7 integration points in FBE models and 32 sub-elements in DBE models.

As demonstrated in Fig. 4.11 and 4.12, regarding the computational cost, the precision of FBE responses are significantly higher than those of DBE. In case of FBE models, by merely assigning 3 integration points for the elements, the responses become adequately accurate. On the contrary, for FBE models, at least 16 sub-elements are necessary to achieve reliable responses, which significantly increases the computational cost.

4.4 Conclusions

The FEM procedure presented in Chapter 3, based on the beam element with multiple slope discontinuities, is modified here to account the effect of EB-FRP retrofitting of RC frames. The procedure is validated making use of the numerical application in Section 3.5.3, showing a two-story gravity-designed RC frame. Here, only the mid-spans of the beams are EB-FRP retrofitted. For the purpose of validation, the frame is modelled in OpenSees and the results are compared with those of the proposed model. The following conclusions are made:

1. Figure 4.7 demonstrated that the sectional analysis method, which is presented by Italian Guideline CNR-DT 200 R1 [76], is capable of estimating the axial force-bending moment activation domain of the bare and EB-FRP retrofitting RC sections.

2. The results of the pushover analysis, see Fig. 4.5, demonstrates the effect of retrofitting method on the overall lateral capacity of the frame. It is observed that by merely strengthening the mid-spans of the beam elements, not only the plastic hinges that are formed in the mid-spans are shifted to the beam/column joints, but also the evolution pattern of plastic hinges changes, see Fig. 4.4. It is also evident that the current retrofitting strategy slightly increased the overall capacity of the simple RC frame.

3. The results of the OpenSees simulations, see Fig. 4.8, validate the feasibility of the presented FEM procedure. It was shown that the presented FEM procedure, despite being constructed in the framework of concentrated plasticity, is an effective numerical tool to predict the overall lateral capacity of RC frames. In general, the latter is only achievable in distributed plasticity framework with high computational requirements, which are alleviated by the proposed FEM tool.

4. Figures 4.9 and 4.10 reveal that in order to obtain reliable responses using FBE and DBE models, respectively, sufficient number of integration points and sub-elements should be selected. In the former, by assigning 3 integration points and in the latter by discretizing the element into 16 sub-elements, see Figs. 4.11 and 4.12, the numerical errors become negligible. The proposed model, although being formulated on the basis of stiffness method, does not require any element discretization and gives acceptable

results, as proved by OpenSees models, in a reasonable computational time.

Chapter 5

Nonlinear Analysis of RC Frames Retrofitted by Shape Memory Alloys

5.1 Introduction

Due to the unique thermomechanical properties of Shape Memory Alloys, they have gained wide applicability in engineering and medicine and thus attract significant research interest [133]. The spetacular effects, notably pseudoelasticity and Shape Memory Effect (SME), result from reversible martensitic phase transformation in which the material is converted between two solid phases, namely austenite (parent phase), which is high-symmetric and is stable at high temperatures, and martensite (product phase), which is low-symmetric and is stable at low temperatures [165].

SME refers to the ability of SMA to revert its original configuration after the heat induction. Assume a stress-free crystal in austenite phase. By decreasing the temperature of the crystal, the martensite phase is initiated in a self-accommodated (or twinned) state, which contains different variants. As the external mechanical load is applied, oriented (or detwinned) martensite is obtained in which the martensite variants are rearranged into a unique direction. At this point, if the external mechanical load is released, the oriented martensite remains and upon heating converts to austenite and restores the original shape. This cyclic behaviour is presented in Fig. 5.1.

Now, suppose that SMA is heated above the finishing temperature of austen-

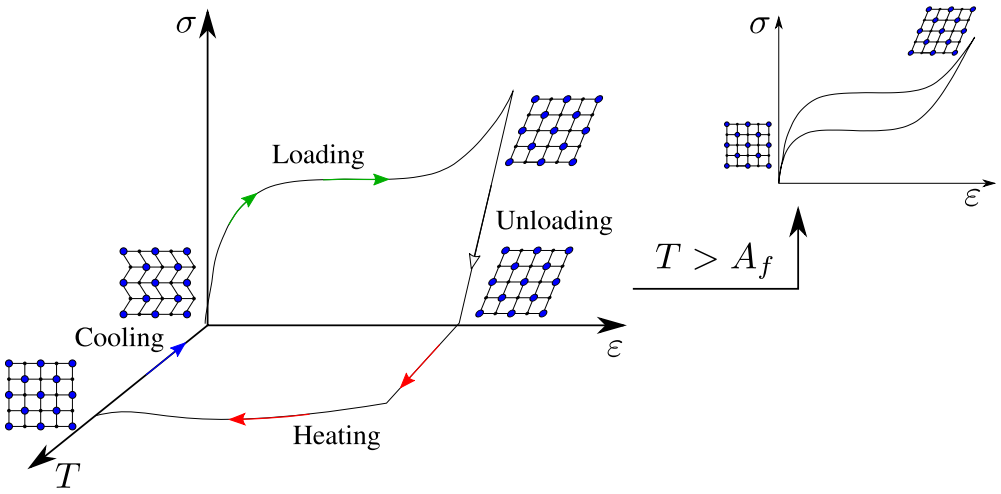

Figure 5.1: The illustration of shape memory effect (left) and pseudoelasticity (right) properties in shape memory alloys.

ite A_f, which is the temperature whereat the phase transformation from martensite to austenite finishes. In this case, by applying the external mechanical load, the material experiences direct transformation from austenite to oriented martensite. Similarly, upon unloading, direct transformation from oriented martensite to austenite occurs. This phenomenon is called the pseudoelasticty and is illustrated in Fig. 5.1.

Numerous constitutive models have been adopted to address various aspects of the complex behaviour of SMAs, from atomistic to the macroscopic scale. A detailed overview of the constitutive models of SMAs available in the literature is beyond the scope of this Chapter, the reader is referred to recent reviewers (e.g. Patoor et al. [136]; Lagoudas et al. [95]; Cisse at al. [42]).

This Chapter first presents a one-dimensional constitutive model of pseudoelasticity in SMA. The model is indeed a one-dimensional small strain version of the model developed by Stupkiewicz and Petryk [166]. Then, a gradient-enhancement is introduced into the model followed by themomechanical formulation and implementation into a finite element code. Using this model, the true response of a nickel-titanium (NiTi) wire is studied in uniaxial tension. In Section 5.4, the first introduced one-dimensional constitutive model is programmed into the FE code developed in Section 3 to investigate the effectiveness of SMA brace retrofitting technique in RC structures. For the numerical appli-

cation, the RC frame of Section 3.5.1 is modelled and the results are discussed. Finally, conclusions are drawn in Section 5.6.

The writer indicates that Sections 5.2 and 5.3 of this chapter are mostly taken from the paper by Rezaee Hajidehi and Stupkiewicz [148].

5.2 One-Dimensional Pseudoelasticity Model of SMA

The starting point here is a one-dimensional small-strain version of the three-dimensional general model of pseudoelasticity developed by Stupkiewicz and Petryk [166]. Despite the model is one-dimensional, in the notation ∇ and $\nabla\cdot$ are used to denote the gradient and divergence, respectively. The reason is to keep the structure of the model for the corresponding three-dimensional model to be developed in the future.

The total strain $\varepsilon = e(u)$, where $e(u) = \nabla u$ and u denotes the displacement, is decomposed into its elastic ε_e and inelastic (transformation) ε_t parts,

$$\varepsilon = \varepsilon_e + \varepsilon_t, \qquad \varepsilon_t = \eta\bar{\epsilon}_t, \qquad 0 \le \eta \le 1, \tag{5.1}$$

where η denotes the volume fraction of martensite, and $\bar{\epsilon}_t$ is a model parameter. Here, we rely on the assumption that, in the pseudoelastic regime, martensite is fully oriented, and $\bar{\epsilon}_t$ is its transformation strain, which is defined as the maximum transformation strain produced in a complete martensitic transformation.

The function specifying the Helmholtz free energy (per unit volume) in isothermal conditions is adopted in the following form,

$$\phi(\varepsilon,\eta) = \phi_0 + \Delta\phi_0\eta + \frac{1}{2}E(\varepsilon - \eta\bar{\epsilon}_t)^2 + \frac{1}{2}H\eta^2, \tag{5.2}$$

where ϕ_0 is the free energy of austenite in a stress-free state, $\Delta\phi_0$ is the chemical energy, E is the Young's modulus, and H is the parameter controlling the hardening or softening associated with increasing η. It is supposed here that H is non-negative, $H \ge 0$, because for $H < 0$ a softening response is obtained, as discussed in Section 5.3, and the problem becomes ill-posed.

The Helmholtz free energy functional $\Phi[u,\eta]$ is obtained by integrating ϕ over the body domain B,

$$\Phi[u,\eta] = \int_B \phi(e(u),\eta)\,\mathrm{dV}, \tag{5.3}$$

and the potential energy is defined as

$$\mathcal{E}[u,\eta] = \Phi[u,\eta] + \Omega[u], \tag{5.4}$$

where $\Omega[u]$ is the potential energy of external loads, which are assumed conservative.

In the incremental formulation, the rate-independent dissipation is governed by the following dissipation potential,

$$\Delta D(\Delta\eta) = f_c|\Delta\eta|, \qquad f_c > 0, \qquad \Delta\eta = \eta - \eta_n, \tag{5.5}$$

and its global counterpart,

$$\Delta\mathcal{D}[\eta] = \int_B \Delta D(\eta - \eta_n)\,\mathrm{dV}, \tag{5.6}$$

where f_c is the critical driving force, and η_n is the martensite volume fraction at the end of the previous step. Note that quantities without a subscript refer to the current time instant $t = t_{n+1}$.

The incremental solution, i.e. the fields of displacement u and volume fraction of martensite η at the current time step t_{n+1}, are determined by minimization of the global incremental potential $\Pi[u,\eta]$ (see Petryk [142]; Stupkiewicz and Petryk [166]),

$$\{u,\eta\} = \arg\min_{u,\eta}\ \Pi[u,\eta], \tag{5.7}$$

where

$$\Pi[u,\eta] = \mathcal{E}[u,\eta] - \mathcal{E}[u_n,\eta_n] + \Delta\mathcal{D}[\eta] + \mathcal{I}[\eta], \tag{5.8}$$

and u is implicitly assumed to satisfy the Dirichlet boundary condition. The last term in Eq. (5.8) enforces the physical constraint $0 \le \eta \le 1$ by employing the indicator function $\mathcal{I}[\eta]$,

$$\mathcal{I}[\eta] = \int_B I_{[0,1]}(\eta)\mathrm{dV}, \qquad \mathrm{I}_{[0,1]}(\eta) = \begin{cases} 0 & \text{if } 0 \le \eta \le 1, \\ +\infty & \text{otherwise.} \end{cases} \tag{5.9}$$

Because of the last two terms in the incremental potential (5.8), the minimization problem (5.7) is non-smooth.

Following the standard argument, minimization of $\Pi[u,\eta]$ with respect to the displacement field u, for a fixed field of η, yields a stable equilibrium of

the body, and the necessary condition for the minimum gives the equilibrium equation in a weak form. In the absence of body force, the standard equilibrium equation is obtained as,

$$\nabla \cdot \sigma = 0, \qquad \sigma = E(\varepsilon - \eta\bar{\epsilon}_t), \tag{5.10}$$

where σ is the stress. It is immediate to understand that in one-dimensional setting, the equilibrium equation implies that the stress is constant.

Since the free energy $\phi(\varepsilon, \eta)$ depends on η but not on its gradient, minimization of $\Pi[u, \eta]$ with respect to the field of η, for a fixed displacement field u, can be performed locally at each point. The corresponding local minimization problem amounts to minimizing the incremental energy density $\pi(\varepsilon, \eta)$ at fixed ε,

$$\begin{aligned} \eta &= \arg\min_{\eta} \pi(\varepsilon, \eta), \\ \text{with} \qquad \pi(\varepsilon, \eta) &= \phi(\varepsilon, \eta) - \phi(\varepsilon_n, \eta_n) + \Delta D(\eta - \eta_n) + I_{[0,1]}(\eta). \end{aligned} \tag{5.11}$$

It can be checked that the free energy function $\phi(\varepsilon, \eta)$ is convex in η when $H \geq -E\bar{\epsilon}_t^2$. The remaining two terms of $\pi(\varepsilon, \eta)$ are also convex, though non-smooth, see Fig. 5.2. Accordingly, the minimum exists and satisfies the inclusion $0 \in \partial\pi_\varepsilon(\eta)$, where $\pi_\varepsilon(\eta) = \pi(\varepsilon, \eta)$ for given ε, which can be rewritten in the following form,

$$f \in \partial\bar{D}(\eta), \qquad \bar{D}(\eta) = \Delta D(\eta - \eta_n) + I_{[0,1]}(\eta), \tag{5.12}$$

where f is the thermodynamic driving force,

$$f = -\frac{\partial\phi}{\partial\eta} = -\Delta\phi_0 + \sigma\bar{\epsilon}_t - H\eta, \tag{5.13}$$

and $\bar{D}(\eta)$ groups the non-smooth part of $\pi(\varepsilon, \eta)$. Here, $\partial(\cdot)$ denotes the subdifferential which is a generalization of the derivative to non-smooth functions (Rockafellar [149]). Figure 5.2 shows the graphs of the non-smooth function $\bar{D}(\eta)$ and its subdifferential $\partial\bar{D}(\eta)$, see also Stupkiewicz and Petryk [166].

When the transformation proceeds with non-zero $\Delta\eta$, and the bound constraints are not active, i.e. $0 < \eta < 1$, inclusion (5.11) yields the following transformation criterion,

$$f = \pm f_c \quad \Leftrightarrow \quad \sigma_t^{\pm} = \frac{\Delta\phi_0 \pm f_c + H\eta}{\bar{\epsilon}_t}, \tag{5.14}$$

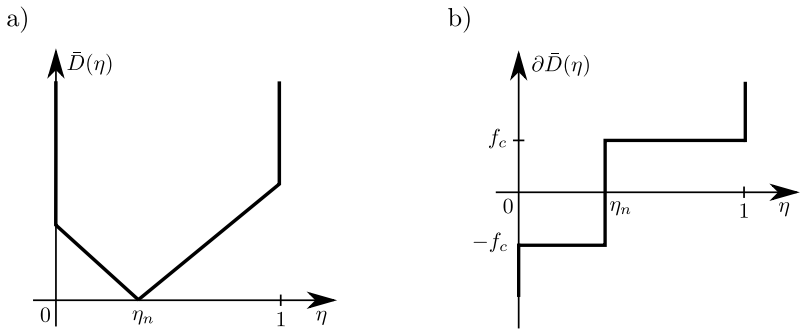

Figure 5.2: Graphs of non-smooth part $\bar{D}(\eta)$, Eq. (5.12), of the incremental potential $\pi(\varepsilon, \eta)$ (a) and its subdifferential (b).

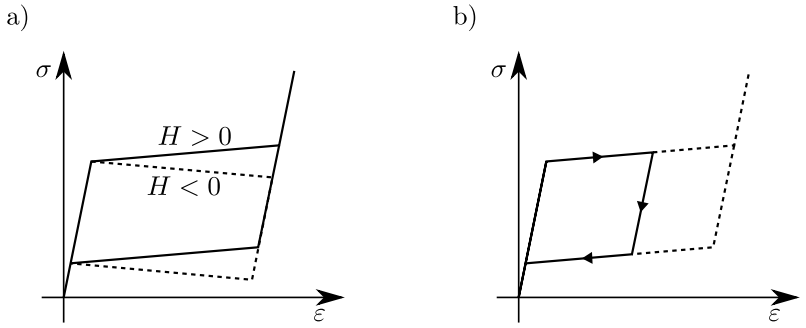

Figure 5.3: The stress-strain response resulting from the model in the case of complete (a) and incomplete (b) transformation.

where $\sigma_t^+(\sigma_t^-)$ is the transformation stress during forward (reverse) transformation with $\Delta\eta > 0$ ($\Delta\eta < 0$). The stress-strain response resulting from the present one-dimensional model is illustrated in Fig. 5.3, in which the controlling role of the parameter H over the stress-strain response of the model is apparent.

5.3 The True Response of SMA in Uniaxial Tension

It is commonly observed in the experiments that stress-induced pseudoelastic response of SMAs is accompanied by softening behaviour and strain localization. A typical example is the uniaxial tension of NiTi wires, strips and tubes (e.g. Shaw and Kyriakides [157]; Sittner et el. [160]; Zhang et al. [179]; Sedmák

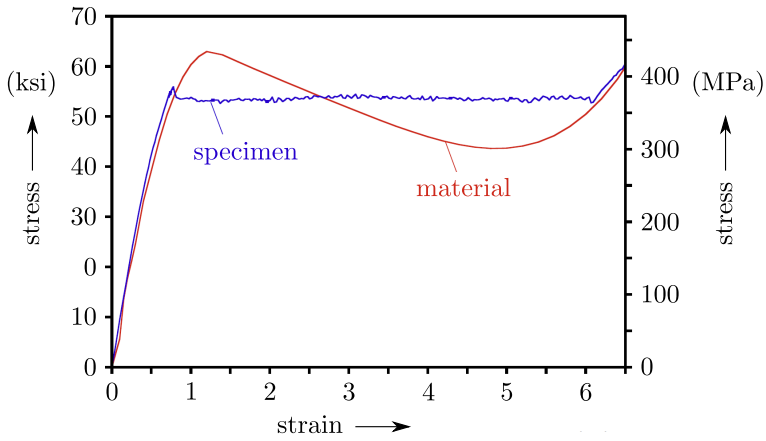

Figure 5.4: The typical mechanical response of SMA in the experiment of Hallai and Kyriakides [71]. The actual material response of NiTi has been revealed by extracting it from the overall response of uniformly deforming laminate composed of NiTi and steel sheets with hardening elasto-plastic response.

et al. [155]) in which transformation proceeds through nucleation and propagation of macroscopic transformation fronts so that the deformation pattern resembles Lüders bands, see Fig. 5.4.

At low loading rates, i.e. in nearly isothermal conditions, the fronts propagate at an approximately constant load, thus a stress plateau is observed on the apparent stress-strain curve. However, at high loading rates, the stress plateau is not observed as a consequence of thermal hardening. The latter also influences the number of transformation fronts, as shown in Fig. 5.5. A detailed study of the effect of loading rate on the transformation fronts and on stress hysteresis in NiTi strips has been reported by Zhang et al. [179].

Implementation of the softening behaviour into a constitutive model usually does not constitute a difficulty. However, solution of the boundary value problem is not immediate because the problem becomes ill-posed, which leads for instance to pathological mesh sensitivity. One way to regularize the problem is to enhance the model with non-local (Ahmadian et al. [1]) or gradient term (Chang et al. [39]; Duval et al. [56]; León Baldelli et al. [102]). This introduces a characteristic length into the model so that diffuse transformation fronts are formed and a sharp transition from the transformed to non-transformed zone is penalized.

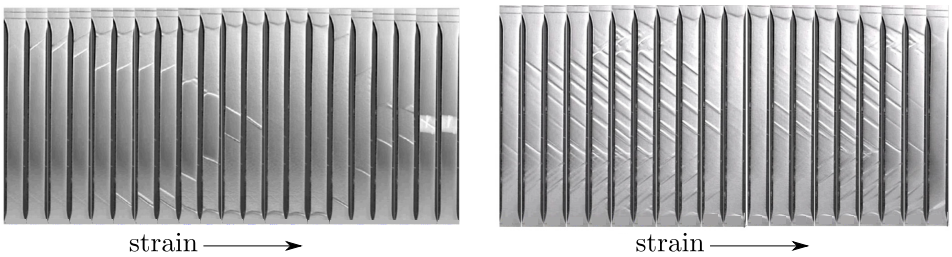

Figure 5.5: The transformation pattern in the experimental study of Zhang et al. [179] for a tensile test with low strain rate, i.e. $3.3 \times 10^{-4}\,\mathrm{s}^{-1}$, (left) and high strain rate, i.e. $3.3 \times 10^{-2}\,\mathrm{s}^{-1}$, (right).

Note that a kind of regularization, which has a clear physical basis, is introduced by including the thermomechanical coupling and heat conduction. However, this regularization may be insufficient in nearly isothermal conditions, for instance, in the case of propagation of an existing macroscopic transformation front at a vanishingly small speed.

Here, a gradient-enhancement is introduced into the model presented in Section 5.2. the main focus is a micromorphic regularization of the gradient-enhanced model and its energy-based incremental formulation. To this end, a new degree of freedom is introduced into the model that can be interpreted as a micromorphic counterpart of the volume fraction of martensite η. The micromorphic approach adopted here is similar to that of Mazière and Forest [117] that has been developed for modelling of softening-hardening plasticity leading to formation of Lüders bands in isotropic metals and alloys. The resulting micromorphic model is suitable for a direct finite element implementation based on the incremental energy minimization approach combined with the augmented Lagrangian treatment (see Stupkiewicz and Petryk [166]) of the resulting non-smooth minimization problem. Finally, a thermomechanically coupled model is formulated and implemented in a finite element code. Using this model, uniaxial tension of a NiTi wire is simulated, and the effect of loading rate on the localization pattern is studied.

Two models are discussed in this section. First, the gradient-enhanced version of the local model developed in Section 5.2 is formulated. Next, the micromorphic regularization of the gradient-enhanced model is presented by introducing a micromorphic variable. Finally, the most essential thermomechanical coupling terms are accounted for, thus leading to a coupled thermomechanical

model.

5.3.1 Gradient-Enhanced Model

A possible approach to circumvent the ill-conditioning resulting from the softening response, when $H < 0$ in Eq. (5.2), is to enhance the model with a gradient term. In the present context of pseudoelasticity in SMAs, it is natural to formulate the gradient contribution in terms of η, the volume fraction of martensite. The free energy function is thus assumed in the following form,

$$\phi_g(\varepsilon, \eta, \nabla\eta) = \phi(\varepsilon, \eta) + \frac{1}{2} G |\nabla\eta|^2. \tag{5.15}$$

The gradient term in Eq. (5.15) delivers regularization for the model and the G parameter, which is a positive parameter, controls the degree of regularization.

The Helmholtz free energy functional $\Phi_g[u, \eta]$ of the gradient-enhanced model and the corresponding potential energy $\mathcal{E}_g[u, \eta]$ are defined as

$$\Phi_g[u, \eta] = \int_B \phi_g(e(u), \eta, \nabla\eta)\, \mathrm{dV}, \qquad \mathcal{E}_{\mathrm{g}}[\mathrm{u}, \eta] = \Phi_{\mathrm{g}}[\mathrm{u}, \eta] + \Omega[\mathrm{u}]. \tag{5.16}$$

The global incremental potential $\Pi_g[u, \eta]$, which takes the following form,

$$\Pi_g[u, \eta] = \mathcal{E}_g[u, \eta] - \mathcal{E}_g[u_n, \eta_n] + \Delta\mathcal{D}[\eta] + \mathcal{I}[\eta], \tag{5.17}$$

is then minimized to yield the incremental solution in terms of the fields of u and η at instant t_{n+1},

$$\{u, \eta\} = \arg\min_{u,\eta} \ \Pi_g[u, \eta]. \tag{5.18}$$

As before, the minimization with respect to the displacement field u for fixed η, in the absence of body force, yields the standard equilibrium equation (5.10).

The free energy $\phi_g(\varepsilon, \eta, \nabla\eta)$ depends on the value of η and its gradient $\nabla\eta$. Therefore, the minimization of $\Pi_g[u, \eta]$ with respect to the field of η can not be performed locally as in the case of the local model, see Eqs. (5.11) and (5.12). However, a similar structure of the necessary condition for the minimum of $\Pi_g[u, \eta]$ with respect to η is obtained,

$$f_g \in \partial\bar{D}(\eta), \tag{5.19}$$

by introducing the thermodynamic driving force f_g,

$$f_g = -\frac{\delta\Phi_g}{\delta\eta} = f + G\nabla^2\eta, \tag{5.20}$$

where

$$\frac{\delta \Phi_g}{\delta \eta} = \frac{\partial \Phi_g}{\partial \eta} - \nabla \cdot \frac{\partial \Phi_g}{\partial \nabla \eta}, \tag{5.21}$$

is the classical functional derivative of Φ_g, f is the driving force in the local model, see Eq. (5.13), and ∇^2 denotes the Laplacian operator, i.e. the second spatial derivative in one-dimensional case. It should be noted that the differential inclusion (5.19) is accompanied by the homogeneous Neumann boundary condition, $\nabla_n \eta = 0$, on the boundary of the body domain B.

Assuming that the transformation proceeds with $\Delta\eta \neq 0$ and also $0 < \eta < 1$, the transformation stress in the gradient-enhanced model is obtained from the inclusion (5.19) in the following form,

$$f_g = \pm f_c \quad \Leftrightarrow \quad \sigma^{\pm}_{t,g} = \frac{\Delta\phi_0 \pm f_c + H\eta - G\nabla^2\eta}{\bar{\epsilon}_t}. \tag{5.22}$$

5.3.2 Micromorphic Model

Direct implementation of the gradient-enhanced model of the previous section is not straightforward because the transformation criterion (5.19), which governs the evolution of η, involves the Laplacian of η. To facilitate the finite element implementation, a micromorphic regularization of the gradient-enhanced model is performed here by introducing an additional variable $\bar{\eta}$, as a micromorphic counterpart of η, see Forest [64] for a general overview of the micromorphic regularization approach.

The free energy function is thus adopted in the following form,

$$\phi_\mu(\varepsilon, \eta, \bar{\eta}, \nabla\bar{\eta}) = \phi(\varepsilon, \eta) + \frac{1}{2}\chi(\eta - \bar{\eta})^2 + \frac{1}{2}G\left|\nabla\bar{\eta}\right|^2, \tag{5.23}$$

where, compared to $\phi_g(\varepsilon, \eta, \nabla\eta)$ in Eq. (5.15), the gradient term is expressed in terms of the new variable $\bar{\eta}$, and an additional term is introduced, which penalizes deviation of η from $\bar{\eta}$, with $\chi > 0$ being the corresponding model parameter.

The free energy functional $\Phi_\mu[u, \eta, \bar{\eta}]$ and the corresponding potential energy $\mathcal{E}_\mu[u, \eta, \bar{\eta}]$ are now defined, respectively, as,

$$\Phi_\mu[u, \eta, \bar{\eta}] = \int_B \phi_\mu(e(u), \eta, \bar{\eta}, \nabla\bar{\eta})\,\mathrm{dV}, \tag{5.24}$$

and

$$\mathcal{E}_\mu[u,\eta,\bar{\eta}] = \Phi_\mu[u,\eta,\bar{\eta}] + \Omega[u]. \tag{5.25}$$

Since a new degree of freedom is added to the problem, the minimization of the global incremental potential

$$\Pi_\mu[u,\eta,\bar{\eta}] = \mathcal{E}_\mu[u,\eta,\bar{\eta}] - \mathcal{E}_\mu[u_n,\eta_n,\bar{\eta}_n] + \Delta\mathcal{D}[\eta] + \mathcal{I}[\eta], \tag{5.26}$$

is now performed with respect to fields of u, η and $\bar{\eta}$

$$\{u,\eta,\bar{\eta}\} = \arg\min_{u,\eta,\bar{\eta}} \Pi_\mu[u,\eta,\bar{\eta}]. \tag{5.27}$$

Again, for fixed η and $\bar{\eta}$, the local equilibrium equation (5.10) is found by minimizing $\Pi_\mu[u,\eta,\bar{\eta}]$ with respect to the displacement field u.

As in the case of the local model, the free energy $\phi_\mu(\varepsilon,\eta,\bar{\eta},\nabla\bar{\eta})$ is merely dependent on η and not its gradient. As a result, the minimization of $\Pi_\mu[u,\eta,\bar{\eta}]$ with respect to η can be carried out locally. This is, in fact, the main reason for introducing the micromorphic regularization of the gradient-enhanced model. For fixed ε , $\bar{\eta}$ and $\nabla\bar{\eta}$, the local minimization problem reads

$$\eta = \arg\min_{\eta} \pi_\mu(\varepsilon,\eta,\bar{\eta},\nabla\bar{\eta}), \tag{5.28}$$

where

$$\pi_\mu(\varepsilon,\eta,\bar{\eta},\nabla\bar{\eta}) = \phi_\mu(\varepsilon,\eta,\bar{\eta},\nabla\bar{\eta}) - \phi_\mu(\varepsilon_n,\eta_n,\bar{\eta}_n,\nabla\bar{\eta}_n) + \Delta D(\eta-\eta_n) + I_{[0,1]}(\eta). \tag{5.29}$$

Convexity of $\phi_\mu(\varepsilon,\eta,\bar{\eta})$ and $\pi_\mu(\varepsilon,\eta,\bar{\eta},\nabla\bar{\eta})$ in η is ensured if $H \geq -E\bar{\epsilon}_t^2 - \chi$. The necessary condition for the minimum (5.28) is now

$$f_\mu \in \partial\bar{D}(\eta), \tag{5.30}$$

and is expressed in terms of the thermodynamic driving force f_μ,

$$f_\mu = -\frac{\partial\phi_\mu}{\partial\eta} = f - \chi(\eta-\bar{\eta}), \tag{5.31}$$

where f is given by Eq. (5.13). For $\Delta\eta \neq 0$ and $0 < \eta < 1$, inclusion (5.30) gives the following expression for the transformation stress,

$$f_\mu = \pm f_c \quad \Leftrightarrow \quad \sigma_{t,\mu}^{\pm} = \frac{\Delta\phi_0 \pm f_c + H\eta + \chi(\eta-\bar{\eta})}{\bar{\varepsilon}_t}. \tag{5.32}$$

Finally, minimization of $\Pi_\mu[\varepsilon, \eta, \bar{\eta}, \nabla\bar{\eta}]$ with respect to the fields of $\bar{\eta}$ yields the following necessary condition,

$$\frac{\delta\Pi_\mu}{\delta\bar{\eta}} = 0, \tag{5.33}$$

where $\frac{\delta\Pi_\mu}{\delta\bar{\eta}}$ is the functional derivative of Π_μ, see Eq. (5.21). Since Π_μ depends on $\bar{\eta}$ only through Φ_μ, thus

$$\frac{\delta\Pi_\mu}{\delta\bar{\eta}} = \frac{\delta\Phi_\mu}{\delta\bar{\eta}} = -\chi(\eta - \bar{\eta}) - G\nabla^2\bar{\eta} = 0. \tag{5.34}$$

The micromorphic variable $\bar{\eta}$ is thus governed by the following differential equation,

$$\bar{\eta} - \ell^2\nabla^2\bar{\eta} = \eta, \qquad \ell = \sqrt{\frac{G}{\chi}}, \tag{5.35}$$

where ℓ is internal length related to the averaging operation delivered by Eq. (5.35). The Holmholtz-type equation (5.35) is the same as the one frequently used for regularization of damage or softening plasticity within the so-called implicit-gradient approach (Peerlings et al. [140]; Mazière and Forest [117]).

Equation (5.35) is accompanied here by the homogeneous boundary condition, $\nabla_n\bar{\eta} = 0$ on the boundary of the domain B. The above Neumann type-boundary condition together with Eq. (5.35) implies that $\int_B \eta \mathrm{dV} = \int_\mathrm{B} \bar{\eta}\mathrm{dV}$. This property would not hold for a Dirichlet boundary condition, which might be used, for instance, to define a non-transforming boundary.

From Eq. (5.34) it follows that $\chi(\eta - \bar{\eta}) = -G\nabla^2\bar{\eta}$, so that the term $\chi(\eta - \bar{\eta})$ in the expression (5.32) for the transformation stress $\sigma^{\pm}_{t,\mu}$ can be replaced by $-G\nabla^2\bar{\eta}$. Now, when χ is sufficiently large, $\bar{\eta}$ gets close to η and therefore $\nabla^2\bar{\eta}$ gets close to $\nabla^2\eta$. It follows that, in the limit, the micromorphic model is equivalent to the gradient-enhanced model, and in particular $f_\mu \approx f_g$, and $\sigma^{\pm}_{t,\mu} \approx \sigma^{\pm}_{t,g}$. This property is demonstrated in a propagating phase transformation interface, i.e. the profiles of η and $\bar{\eta}$, shown in Fig. 5.6. Two different cases are investigated, one with a low value of χ and the other with a high value of χ. In the latter case, the two curves can be hardly distinguished, and they approximately coincide with the solution of the gradient-enhanced model (dashed lines in Fig. 5.6). The markers in Fig. 5.6 denote the finite element solutions. For a detailed discussion of the gradient-enhanced and micromorphic models and also the analytical solutions, the reader is referred to [148].

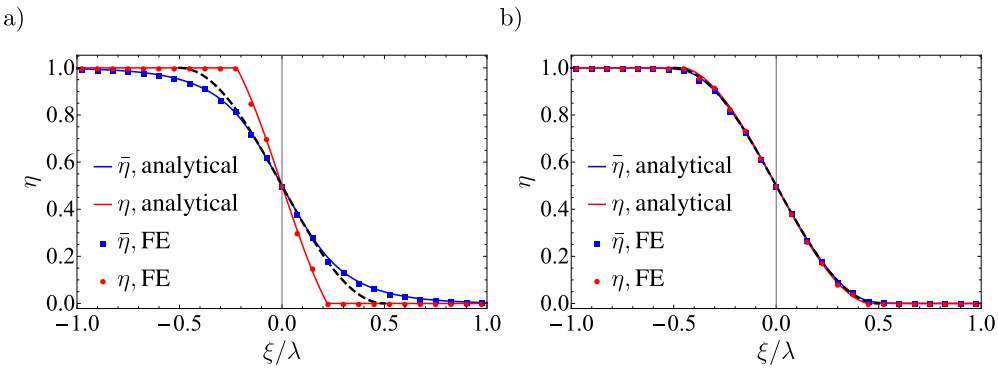

Figure 5.6: Phase transformation interface in the micromorphic model: profiles of η and $\bar{\eta}$ when χ is small (a) and when χ is large (b). The dashed lines correspond to the analytical solution for the gradient-enhances model. ξ/λ represents the horizontal position normalized by the thickness of the diffused interface (see [148]).

5.3.3 Thermomechanically Coupled Model

For extending the model to thermomechanically coupled one, the heat conduction and two most essential thermomechanical couplings are considered. Firstly, the dependence of the chemical energy $\Delta\phi_0$ on the temperature is accounted for, thus introducing dependence of the mechanical response on the temperature. Secondly, the latent heat of transformation, which is associated with the exothermic and endothermic nature of, respectively, forward and reverse transformations, and the dissipated energy are introduced into the heat equation as a source term, so that inhomogeneous deformation results in the temperature inhomogeneity and in heat conduction. Note that other couplings, including thermal expansion and temperature-dependence of material constants, which are secondary effects, are neglected in the present model.

The free energy density of a pure austenite phase in a stress-free condition, ϕ_0^a, and that of a pure martensite phase, ϕ_0^m, are defined as (Raniecki et al. [146])

$$\phi_0^a = \phi_0(T) + u_0^a - Ts_0^a, \qquad \phi_0^m = \phi_0(T) + u_0^m - Ts_0^m, \tag{5.36}$$

where u_0^a and u_0^m are the internal energy densities of, respectively, austenite and martensite phases in the reference state, i.e. in the stress-free condition at $T = T_0$, s_0^a and s_0^m are the entropies of, respectively, austenite and martensite phases in the reference state, and $\phi_0(T) = \rho c(T - T_0 - T\log(T/T_0))$, where T

and T_0 are the current and reference temperatures, respectively, and ρc is the specific heat per unit volume.

The chemical energy, $\Delta\phi_0$, that appears in Eq. (5.2) is then obtained as a linear function of temperature,

$$\Delta\phi_0(T) = \phi_0^m - \phi_0^a = -\Delta u^* + \Delta s^* T = \Delta s^*(T - T_t), \tag{5.37}$$

where $\Delta u^* = u_0^a - u_0^m > 0$, $\Delta s^* = s_0^a - s_0^m > 0$, and $T_t = \frac{\Delta u^*}{\Delta s^*}$ is the transformation (equilibrium) temperature. It follows that the chemical energy $\Delta\phi_0$ increases with increasing temperature, for instance, during forward transformation ($\dot{\eta} > 0$), which is exothermic. In non-isothermal conditions, the transformation stress will thus increase (decrease) during forward (reverse) transformation, see Eqs. (5.13), (5.22) and (5.32).

The local heat source results from the latent heat of transformation and mechanical dissipation. Specifically, the volumetric heat source $\dot{q}_v$ is expressed as,

$$\dot{q}_v = \Delta s^* T \dot{\eta} + f_c|\dot{\eta}|, \tag{5.38}$$

where a superposed dot denotes the time derivative. The first term, which corresponds to the latent heat of transformation, controls the exothermic and endothermic reactions of the forward (with $\dot{\eta} > 0$) and reverse (with $\dot{\eta} < 0$) transformations, respectively. Finally, the local heat equation takes the form,

$$\rho c = \dot{T} = \dot{q}_v + \kappa \nabla^2 T, \tag{5.39}$$

where κ is the thermal conductivity.

5.3.4 Uniaxial Tensile Response of a NiTi Wire

5.3.4.1 Finite element implementation

The coupled thermomechanical problem at hand is governed by the minimization problem (5.27) (the mechanical part) and by the heat equation (5.39) (the thermal part). As discussed in Section 5.3.2, the incremental potential (5.26) is non-smooth in the local variable η, however the corresponding minimization can be performed locally, e.g. at each Gauss point in the finite element implementation. Here, following Stupkiewicz and Petryk [166], the augmented Lagrangian method is used to transform the non-smooth constrained minimization in terms of η to a smooth constrained saddle-point problem in terms of η

and a single Lagrange multiplier that treats both the non-smooth dissipation function and the bound constraints on η. For details the reader is referred to Stupkiewicz and Petryk [166].

The complete problem involves three global fields (u, $\bar{\eta}$, T). In the finite element discretization, the displacement field u is approximated using piecewise-quadratic shape functions, while $\bar{\eta}$ and T are approximated using piecewise-linear shape functions. The resulting discrete finite element equations are solved in a monolithic manner using the Newton method. Computer implementation has been performed using the AceGen/AceFEM system (Korelc [89]; Korelc and Wriggers [90]). In particular, the automatic differentiation (AD) technique implemented in AceGen has been used to automatically derive the exact algorithmic tangent.

5.3.4.2 Problem description

The uniaxial response of a NiTi wire under tension is studied as an application of the model developed. The main focus of this numerical example is to show the suitability of the proposed micromorphic formulation to describe nucleation and propagation of macroscopic transformation fronts. Having this modelling tool, the effect of the loading rate on the force-displacement response, transfromation pattern and temperature field is also studied. Material parameters have been adopted such that the model predictions are qualitatively comparable to the experimental results of Zhang et al. [179]. It should be noted here that the aim of the numerical example presented here is not to reproduce the exact results of Zhang et al. [179] but to simulate them in a qualitative manner. This is because the present one-dimensional model is a significant simplification compared to the experimental setup of Zhang et al. [179].

The one-dimensional wire model is sketched in Fig. 5.7. The total elongation of the wire is prescribed according to $\delta(t) = L\bar{\varepsilon}(t)$, where $L = 30$ mm is the length of the wire, and the average strain rate $\dot{\bar{\varepsilon}}$ is assumed constant during loading and unloading. To trigger the strain localization in the wire, the temperature of the wire at both ends is fixed and equal to the initial temperature $T_0 = 296$ K. Material parameters $E = 35$ GPa, $H = -2.2$ MPa, $f_c = 6.8$ MPa, $\bar{\epsilon}_t = 0.049$, $T_t = 244$ K, $\Delta s^* = 0.24$ MPa/K have been calibrated such that the isothermal response of the model approximates the experimental one (Zhang et al. [179]) reasonably well. Parameters $\rho = 6500$ kg/m^3, $c = 440$ J/(kg K) and $\kappa = 18$ W/(m K) assume the values typical for NiTi (e.g. Armattoe et al. [8]). The gradient-related parameters, namely $G = 0.014$ Pa m^2 and $\chi = 116$

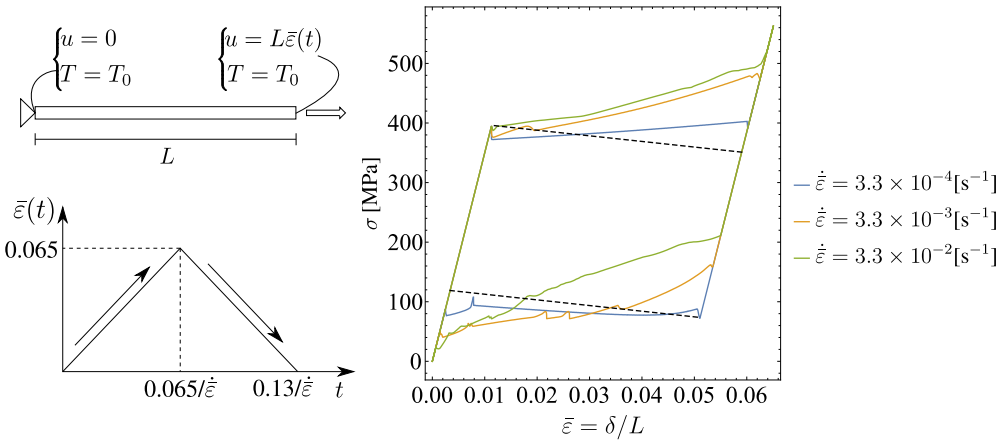

Figure 5.7: Uniaxial tension of a NiTi wire: problem setup and the predicted stress-average strain response corresponding to three representative average strain rates. The dashed line depicts the isothermal, homogeneous softening response.

MPa have been adopted such that sufficient regularization is obtained and that the model produces macroscopic transformation fronts with a reasonable thickness λ (here $\lambda = 0.25$ mm has been taken). A relatively fine finite element mesh of 600 elements has been used in the computations so that the element size $h = 0.05$ mm is sufficiently small with respect to the interface thickness, $\lambda = 5h$.

5.3.4.3 Results and Discussion

Although the computations have been carried out for eleven strain rates, the results obtained for three representative strain rates, namely $\dot{\bar{\varepsilon}} = 3.3 \times 10^{-4}$ s^{-1}, $\dot{\bar{\varepsilon}} = 3.3 \times 10^{-3}$ s^{-1} and $\dot{\bar{\varepsilon}} = 3.3 \times 10^{-2}$ s^{-1} are discussed in detail. Figure 5.7 compares the corresponding stress-strain curves. The elastic branches at the point at which the transformation initiates are identical for all curves. For the case with the lowest strain rate ($\dot{\bar{\varepsilon}} = 3.3 \times 10^{-4}$ s^{-1}), the thermal effect is not much pronounced, and the stress-strain curve is close to the isothermal case, particularly during loading. For higher loading rates, the stress plateau is no longer observed during loading and significant hardening is predicted as a result of the increase in temperature during forward transformation. The effect of loading rate on the unloading branch is more complex. This is due to the inhomogeneity of temperature and development of complex transformation

patterns (see [148]).

The detailed results of individual simulations are depicted in Fig. 5.8. The first, second and third columns show the stress-strain curves, the transformation patterns and the temperature fields. The dashed curves in the stress-strain diagrams represent the experimental results obtained by Zhang et al. [179]. For the transformation pattern in the middle column, the vertical axis represents the position on the wire, the horizontal axis represents the normalized time, and the color intensity represents the volume fraction of martensite. Similarly, for the temperature field, the color represents the relative temperature $\theta = T - T_0$ as a function of position and time.

The predicted effect of the loading rate on the stress-strain response shows a good agreement with the experiment. At higher loading rates, the stress predicted during reverse transformation is visibly lower than in the experiment so that the area of the hysteresis loop is overpredicted. A possible reason for the discrepancy is that in the model the transformation is completed upon load removal while in the experiment it is not necessarily completed. The present simple constitutive model is not able to capture this feature.

The middle column in Fig. 5.8 illustrates the effect of loading rate on the pattern and evolution of austenite and martensite domains. The general feature is that the number of domains increases with increasing loading rate. It can be seen that the transformation pattern and the number of domains during forward and reverse transformations are different. This is due to the prior history and non-uniform temperature at the beginning of the unloading stage.

By examaining in detail the density plots of austenite and martensite patterns of all eleven computations conducted in this study, an exponential relationship between the number of domains and the average strain rate can be derived. In addition, it was found out that the average stress hysteresis, which is calculated as the area of the hysteresis loop divided by the transformation strain $\bar{\epsilon}_t$, exhibits the maximum at the strain rate of about 2×10^{-3} s^{-1}. For space reasons, the plots of these results are not shown here, the reader is referred to [148].

Summarizing, despite its simplicity, the present model is capable of reproducing several thermomechanical effects that accompany uniaxial tension of NiTi in a wide range of strain rates. In particular, the proposed micromorphic model proves efficient in modelling nucleation and evolution of complex transformation patterns induced by a softening mechanical response.

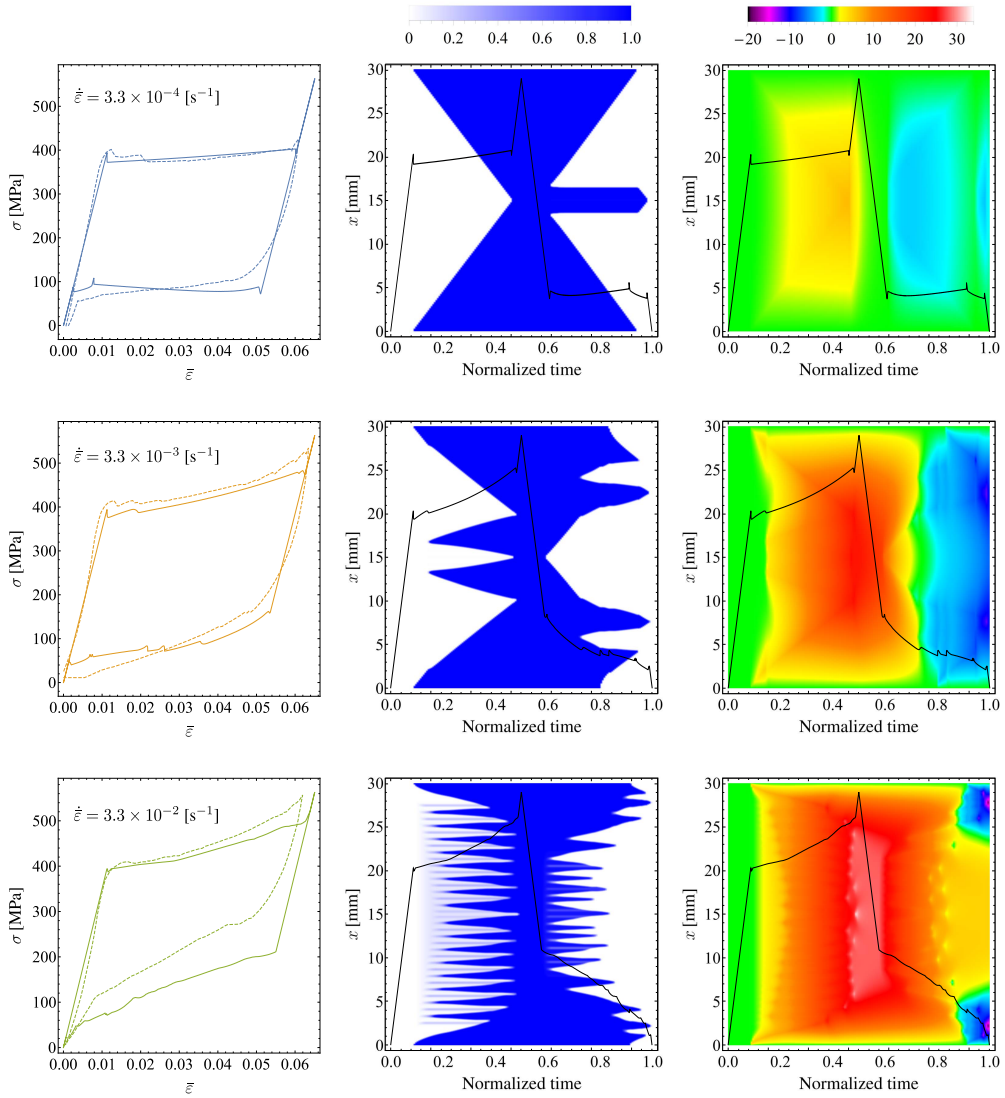

Figure 5.8: Detailed results of representative average strain rates: stress-strain response (left), transformation pattern represented by η (middle), relative temperature field (right). The predicted stress-strain response (solid lines) is compared to the experimental results of Zhang et al. [179] (dashed lines). The solid lines superimposed on the counter plots in the middle and right columns depict the stress as a function of the normalized time. Further discussion of these results is provided in [148].

5.4 SMA in Civil Structures

5.4.1 Introduction To Passive Structural Control

The re-centring capability and damping capacity of SMA have made these materials an attractive retrofitting choice for civil structures. These features, which are in fact associated with the unique properties of SMA, namely SME and pseudoelasticity, come from the capacity of the material that can transform mechanical energy into thermal energy, which allows to control the vibration of the structure and absorb seismic forces [133]. The method of controlling the structures using the re-centring and damping properties of SMA is called passive control. More expensive control strategies by SMA, i.e. active and semi-active techniques, rely on an external source that supplies energy to the controlling devices. The applications of different SMA controlling strategies in civil structures have been reviewed by many authors (e.g. Desroches and Smith [48]; Alam et al. [2]; Janke et al. [83]; Song et al. [162]; Auricchio et al. [11]), see also Dong et al. [53] for an overview on the applications of SMA in bridges.

5.4.2 SMA Bracing Systems

By taking the advantages of the re-centring and damping properties of SMA, not only a large amount of the energy of the structure during earthquake excitations can be dissipated, but also the structural elements are forced to restore their initial state after the excitations, thereby the relative displacements and, as a result, stresses in structural elements are reduced to a large extent. One of the main applications of the passive control SMA devices is in the form of SMA braces, which have been widely used in retrofitting existing RC and steel structures (e.g. Dolce et al. [51]; Cardone et al. [34]; Dolce et al. [52]). Experimental findings show that, although the ordinary steel bracing system provides high energy dissipation to structures, the re-centring capability of SMA braces, which permits the structure to restore its initial configuration even after large inelastic deformations, has made them excellent candidates for seismic retrofitting of framed structures. Figure 5.9 demonstrates the combination of these two characteristics, namely energy dissipation and re-centring, in an idealized constitutive behaviour of SMA. It should be noted that the great versatility of SMA allows to obtain different functionality based on the particular engineering or research purposes, i.e. from largely dissipating to fully re-centring, by changing the elements of the material at the time of manufacturing.

The operation of SMA braces is simple and is based on the martensitic phase

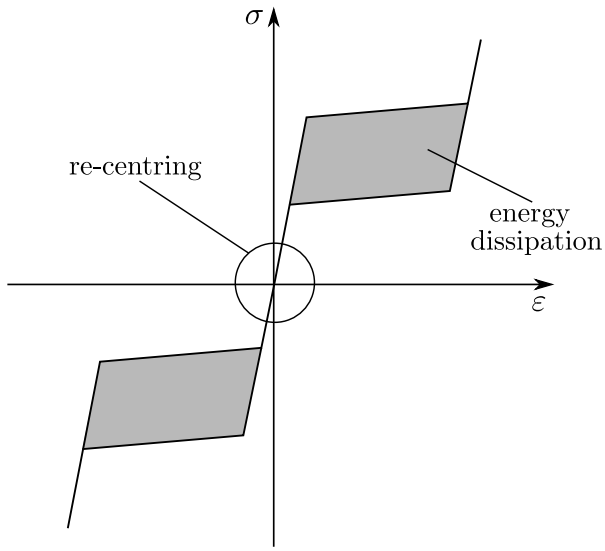

Figure 5.9: The combination of re-centring and energy dissipation in the idealized behaviour of SMA.

transformation. When the frame structure is subjected to seismic actions, SMA braces are activated and use the mechanical energy of horizontal motions for forward phase transformation. During the unloading process, the mechanical load is released and the reverse phase transformation (from martensite phase to austenite phase) is induced, which enforces the structure to recover its initial configuration.

One of the first applications of SMA braces in civil structures was reported by Ohi [130], where steel structures were retrofitted by SMA braces. The results demonstrated that under cyclic loading, SMA braces are able to recover their original shapes even after large strain of 5%.

5.4.3 Previous Researches on SMA Bracing Systems

The most common types of SMA bracing systems utilized for retrofitting framed structures, either are constructed using SMA thin wires, i.e. self-centring SMA devices, or are formed using large diameter SMA bars, i.e. Buckling-Restrained Braces (BRBs). In the former type, steel braces are equipped with SMA wires, so that a hybrid device is constructed in which a combination of high energy

dissipation (steel part) and re-centring capability (SMA wire part) is achieved. These devices are constructed in such a way that the SMA wire is always loaded in tension regardless of whether the brace is in tension or in compression. In the latter type, the SMA bars are equipped with rigid members to prevent the from buckling during compression allowing them to yield in both tension and compression.

Dolce et al. [52] investigated the effectiveness of different bracing systems, showing different energy dissipating and re-centring capacities, on low-ductile RC frames. The kernel components of the SMA braces consisted of pre-tensioned NiTi wires that were installed differently in three different configurations in order to provide different combinations of re-centring and energy dissipating capacities. The 1/3 scale bare and retrofitted RC frames were tested using shake table simulator and the results were compared to each other. The results demonstrated that the SMA braces are able to provide structural performances at least comparable with those obtained by steel braces. In addition, by taking the advantages of the re-centring capability of the SMA braces, no substitution of the bracing system is needed even after a strong earthquake.

Another type of hysteretic damper SMA bracing system was proposed by Tamai and Kitagawa [171]. The brace was made up of SMA and ordinary steel braces, which were anchored together using couplers, and was fastened to the frame by tension bolts. The system was designed in such a way that buckling was prevented even for high slenderness ratios and was capable of exhibiting significant fatigue toughness and energy dissipation under cyclic loading tests. Similar experimental studies aimed at exposing the potential of SMA bracing systems are carried out adopting different designs and arrangements of SMA braces (e.g. Han et al. [72]; Cardone et al. [34]; Dolce et al. [52]; Zhu and Zhang [181]).

As the application of SMA bracing systems in retrofitting framed structures has gained considerable interests due to their feasibility and effectiveness, many researchers have proposed theoretical and numerical models to understand in detail the behaviour and benefits of using such systems. Auricchio et al. [11] explored the possibility of implementing large diameter NiTi bars as a bracing system for three- and six-story steel structures. Two different bracing systems were considered, i.e. buckling-restrained steel and SMA braces. For the latter, a uniaxial constitutive model proposed by Auricchio and Sacco [12], for the pseudoelasticity of SMA in small strain regime, was considered. The results indicated a significant reduction of the residual drifts for the case with SMA bracing system, which ensured the structural re-centring. Similar studies were

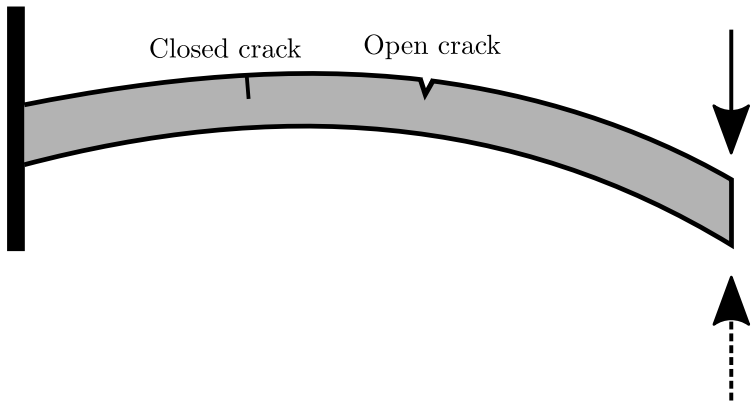

Figure 5.10: A cantilever beam with one open and one closed cracks. The solid arrow shows the direction of loading and the dashed arrow shows the direction of unloading.

conducted in [120] and [121] for low- and mid-rise steel framed structures, using the same constitutive behaviour for SMA braces as in the study of Auricchio et al. [11]. Both studies reported smaller maximum inter-story and residual drifts.

5.5 Application of SMA Braces in RC Framed Structures

The re-centring capability of the SMA braces during unloading allows the possibility of crack closure effect, which is an important phenomenon because of its strong influence on the cyclic response of structures. Note that the term "crack" is used here instead of plastic hinge so that the physical description of the situation will not be obscured. During the unloading stage, the reverse phase transformation of SMA braces initiates, which enforces the framed structure to regain its initial configuration. As a result, some of the open cracks generated in the beam/column elements tend to close. When the crack closure occurs in a generic section, since the fracture surfaces are in complete contact with each other, the punctual reduction of stiffness caused by concentrated damage is eliminated and the beam/column behaves as an uncracked element without slope discontinuities. This situation is schematically illustrated in Fig. 5.10 for a cantilever beam in which one open and one closed crack are detected as a result of loading-unloading cycle.

To account for the effect of switching crack, which by definition exhibits an

abrupt change between the open and closed conditions, the flexural stiffness of the beam in Eq. (3.1) is modified as (see Caddemi et al. [30]),

$$E(x)I(x) = E_0 I_0\Big(1 - \sum_{i=1}^{n} b_i \gamma_i \delta(x - x_i)\Big), \qquad b_i = \begin{cases} 1 & \text{open crack} \\ 0 & \text{closed crack} \end{cases} \tag{5.40}$$

where b_i represents the state of the crack in section i.

The incipient condition of crack closure in a cracked section, i.e. the state of b_i parameter at section i, is determined by the sign of the bending moment. To this end, the values of bending moments in the cracked section i are constantly monitored during the cyclic loading, so that the exact instant at which the bending moment sign changes can be captured. When a crack encounters in section i at instant t_n, the sign of the bending moment at that instant is used as an indicator of the crack presence. During the analysis, if the sign of the bending moment changes, the crack switches from an open state to a closed state, see Bovsunovsky and Surace [25] for an overview of the crack closure effect on the response of different structural elements. The crack closure condition at cracked section i can be written in the following form,

$$sign(M(x_i, t_n)) \neq sign(M(x_i, t_m)), \tag{5.41}$$

where t_m represents the instant at which the crack state of section i is being investigated. Similarly, the crack opening condition takes,

$$sign(M(x_i, t_n)) = sign(M(x_i, t_m)). \tag{5.42}$$

In what follows, the application of SMA braces in RC framed structures is discussed. The flag-shaped constitutive model of pseudoelastic SMA developed by Stupkiewicz and Petryk [166] is characterized by different parameters so that the constitutive model can be readily incorporated into the FEM procedure proposed in Chapter 3. The FEM procedure is thus improved in order to run cyclic analysis on RC frames and is also modified by incorporating the crack state function so that the crack closure effect is taken into consideration during the unloading phase of the analysis.

For the numerical application, steel and SMA braces are designed and used to retrofit the RC frame structure presented in Section 3.5.1. Finally, the results are compared and discussed.

Param.	$\sigma_{\mathrm{S}}^{\mathrm{F}}$ [MPa]	$\sigma_{\mathrm{F}}^{\mathrm{F}}$ [MPa]	$\sigma_{\mathrm{S}}^{\mathrm{R}}$ [MPa]	$\sigma_{\mathrm{F}}^{\mathrm{R}}$ [MPa]	E^{SMA} [GPa]	$\bar{\epsilon}_t$
Value	410	540	370	240	35	4%

Table 5.1: Material parameters of SMA braces for the numerical application.

5.5.1 Adopted Constitutive Model

Here, the constitutive model of pseudoelastic SMA developed by Stupkiewicz and Petryk [166] and presented in Section 5.2 is characterized by four parameters indicating the starting and finishing stresses of forward and reverse transformations, see Fig. 5.11(a). Theses characteristic parameters are as follows: the starting stress of forward transformation, $\sigma_{\mathrm{S}}^{\mathrm{F}}$, the finishing stress of forward transformation, $\sigma_{\mathrm{F}}^{\mathrm{F}}$, the starting stress of reverse transformation, $\sigma_{\mathrm{S}}^{\mathrm{R}}$, and the finishing stress of reverse transformation, $\sigma_{\mathrm{F}}^{\mathrm{R}}$. The model assumes the same modulus of elasticity E^{SMA} in fully austenitic and fully martensitic states (for the sake of not confusing the moduli of elasticity of the materials, the modulus of elasticity E in Eq. (5.2) is renamed as E^{SMA} in this part of the thesis). Table 5.1 provides the material parameters of SMA braces, which are set according to the experimental observations (see e.g. [179] and [47]). It should be pointed out that the material parameters of SMA braces are obtained by calibrating the parameters that are associated with the pseudoelastic model presented in Section 5.2, see Eq. (5.2).

For the steel braces, elasto-plastic constitutive law with linear hardening is considered, see Fig. 5.11(b). Material parameters $E^{\mathrm{steel}} = 200$ GPa, $\sigma_y = 250$ MPa and strain hardening ratio $b = 9\%$ are adopted. To prevent the breakdown of steel braces during the analysis, a wide range of inelastic deformation (very ductile behaviour), i.e. $\varepsilon_u = 15\,\varepsilon_y$, is assumed.

It should be noted that in this study the steel and SMA braces are assumed as large diameter bars that can yield under compressive loads without buckling. However, in the simple numerical example below, only one tensile brace is considered. The primary reason for this is to focus on the main goal of this study, which is to highlight the advantages of SMA braces over steel braces in cyclic loading. To do this, the constitutive models of steel and SMA braces are incorporated into the proposed FEM procedure (see Chapter 3.4) so that the effect of these retrofitting braces on the performance of RC frames can be evaluated.

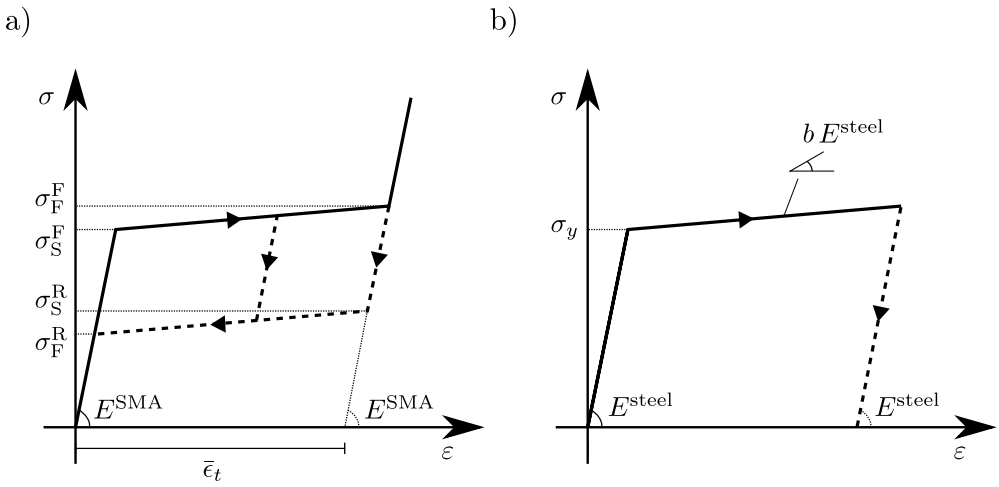

Figure 5.11: Stress-strain behaviour of the SMA braces (a) and steel braces (b).

5.5.2 Numerical Example

In this numerical example, the RC frame presented in Section 3.5.1 is modified by placing one brace element in tension. The brace element is pin-connected at either ends so that only the axial deformations are allowed to develop. At first, the steel braced frame is designed in such a way to increase the ultimate lateral load of the frame to a certain degree, as well as to ensure the yielding of the brace element before the formation of plastic hinges in the beam-column elements. The layout of the braced RC frame is sketched in Fig. 5.12.

The SMA braced frame should be designed in such a manner to be comparable with steel braced frame. For this purpose, the SMA brace is designed to exhibit the same elastic stiffness as the steel brace and also to yield (start martensitic transformation) at the same load level of steel brace. According to these two considerations, the following relations hold,

$$\frac{A^{\mathrm{SMA}}}{A^{\mathrm{steel}}} = \frac{\sigma_y}{\sigma_{\mathrm{S}}^{\mathrm{F}}} \rightarrow A^{\mathrm{SMA}} = \frac{\sigma_y}{\sigma_{\mathrm{S}}^{\mathrm{F}}} A^{\mathrm{steel}}, \tag{5.43}$$

$$\boldsymbol{K}^{\mathrm{SMA}} = \boldsymbol{K}^{\mathrm{steel}} \rightarrow L^{\mathrm{SMA}} = \frac{E^{\mathrm{SMA}} A^{\mathrm{SMA}}}{E^{\mathrm{steel}} A^{\mathrm{steel}}} L^{\mathrm{steel}}, \tag{5.44}$$

where A and L represent the cross-sectional area and length of the brace and $\boldsymbol{K}$ is the axial stiffness of the brace.

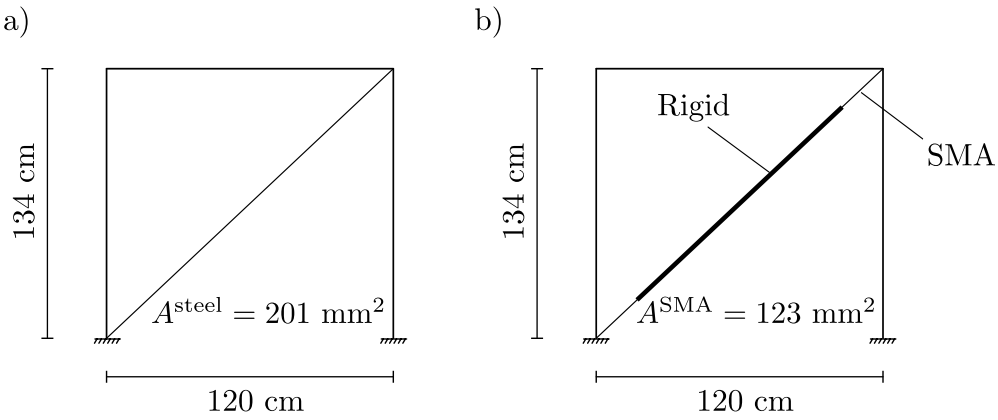

Figure 5.12: The layout of the model in the numerical example: the steel braced frame (a) and the SMA braced frame (b).

By using Eqs. 5.43 and 5.44, the required length $L^{\text{SMA}} = 18$ cm and cross-sectional area $A^{\text{SMA}} = 123$ mm^2 are calculated for the SMA brace. Since the required length of the SMA brace is obtained less than the one of the steel brace, it is assumed that the SMA brace consists of two SMA segments connected to each other by a rigid connector (see e.g. [121] and [9]).

The nonlinear analysis of the frames consists of one cycle of loading and unloading. For both cases (steel and SMA braced frames), a target displacement $\delta_t = 1.34$ cm of the control node (the intersection node of the beam and the left column) is set as the limit for the loading stage of the analysis. This target displacement corresponds to the lateral load level at which the phase transformation of the SMA brace completes. Once the target displacement is reached, the incremental lateral load changes its direction and the unloading stage begins, as illustrated in Fig. 5.13.

To check the validity of the results, the frame is modelled and analysed in OpenSees and the results are compared with results of the FEM procedure. The OpenSees simulations are performed using force-based elements for beam and columns. Concrete02 material and Steel02 material are used for concrete and steel reinforcements, respectively. The steel and SMA braces are modelled through Stee01 material with hardening ratio $b = 9\%$, and SelfCentring material, respectively.

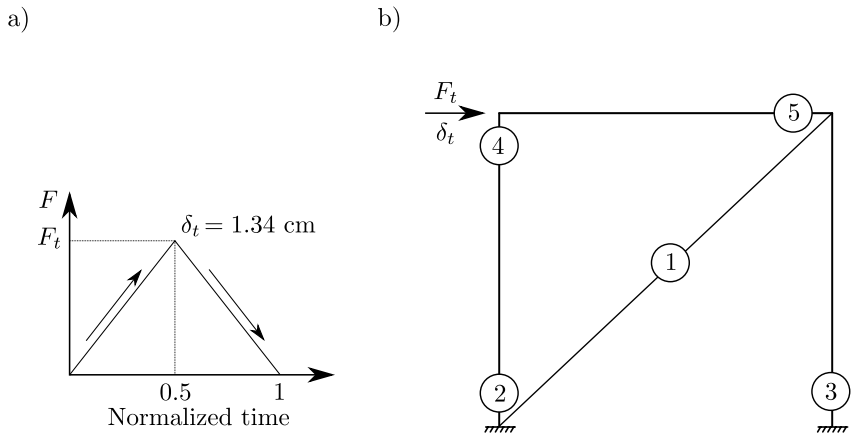

Figure 5.13: The force-normalized time diagram of the loading-unloading (a) and the evolution of plasticity in the frame (b). $\delta = 1.34$ cm corresponds to the load at which the loading stage finishes and unloading stage begins.

5.5.3 Results and Discussion

The evolution of plasticity in the frames during nonlinear analysis is Shown in Fig. 5.13 (b). Since the material and geometric properties of the SMA brace are defined so that both frames have the same natural period, the plasticity evolution turns out to be the same for both frames. It is demonstrated that, as the brace elements were designed, the first plasticity appears in the braces followed by the evolution of plastic hinges in the beam/column elements. It should be noted here that for the SMA brace, the term "plasticity" refers to the initiation of the phase transformation.

The loading-unloading force-displacement curves of the frames are depicted in Fig. 5.14. As mentioned earlier, the force-displacement curves nearly coincide with each other during the loading stage, both giving a lateral force of $F_t = 74$ kN for $\delta_t = 1.34$ cm. During the unloading stage, both curves follow the same path up to the point where the reverse phase transformation in SMA brace initiates. Indeed, the key difference between the SMA brace and traditional steel brace lies in the reverse phase transformation of SMA brace, which enforces the SMA braced frame to recover its original configuration. While in the case of steel braced frame, the unloading branch always follows the same path, which consequently leads to a higher energy dissipation. These characteristics, namely re-centring and energy dissipation, are also observable in the

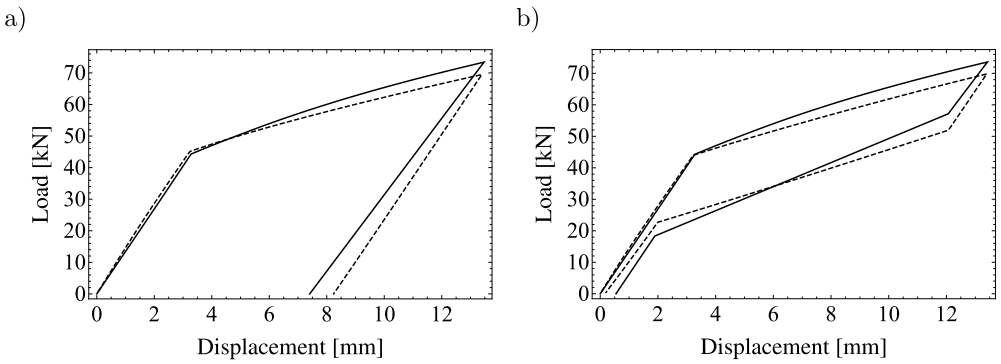

Figure 5.14: Loading-unloading force-displacement curves of steel braced frame (a) and SMA braced frame (b). The dashed lines depict the fiber analysis results obtained from OpenSees.

stress-strain diagrams of the braces, see Fig. 5.15. These results show a good agreement with the fiber analysis results obtained from OpenSees.

Figure 5.16 provides the dissipated energy, calculated as the area enclosed in the loading-unloading force-displacement curves in Fig. 5.15, as well as the residual displacement of the control node. Large permanent displacement is seen for steel braced frame, while thanks to the re-centring capability of the SMA brace, almost no permanent displacement is visible for the SMA braced frame. On the other hand, due to the wide loading-unloading loop of the steel brace, a higher amount of energy is dissipated by the steel braced frame compared to the SMA braced frame.

5.6 Conclusions

The purpose of this chapter of the thesis is to study the behaviour of shape memory alloys and their application in RC frames. The starting point here is the small strain one-dimensional model of pseudoelasticity in SMA developed by Stupkiewicz and Petryk [166].

In the first part of this chapter, a micromorhpic framework has been developed for modelling of formation and propagation of Lüders bands and strain localization that occurs in the actual response of SMAs exhibiting softening. The resulting micromorphic model is suitable for a direct finite element implementation. The displacement field and the micromorphic counterpart of the

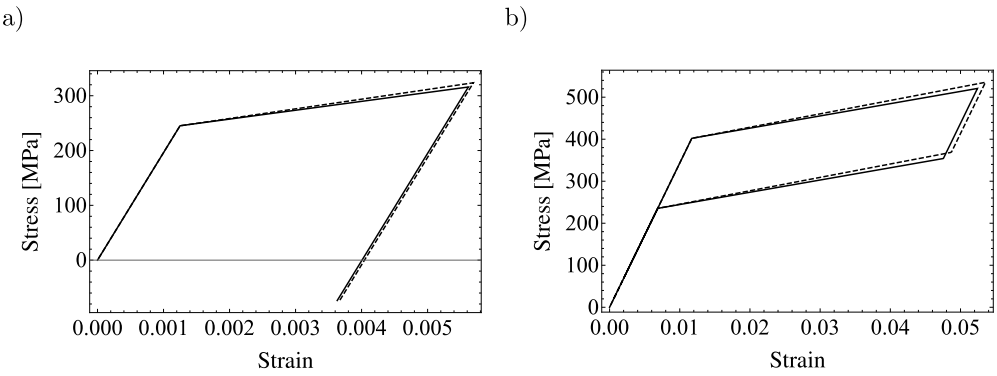

Figure 5.15: Stress-strain curves of steel brace (a) and SMA brace (b). The dashed lines depict the fiber analysis results obtained from OpenSees.

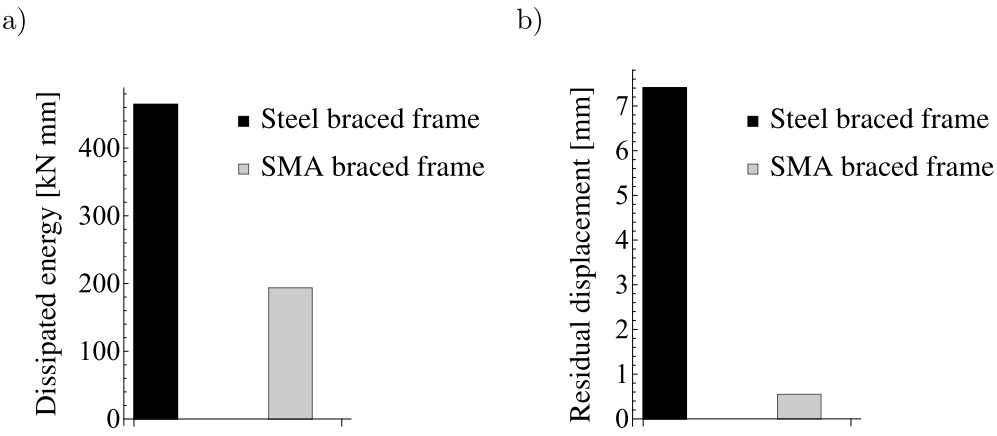

Figure 5.16: The amount of dissipated energy (a) and the residual displacement (b) of the braced frames.

volume fraction of martensite constitute the global unknowns that are governed by respective global equations which express mechanical equilibrium and averaging of the local volume fraction of martensite. A coupled thermomechanical model has also been developed and used for a finite element study of the effect of loading rate on the pseudoelastic response and transformation pattern in a NiTi wire. Despite the simplicity of the constitutive model, its predictions show a good agreement with the experiment.

In the second part of this chapter, the application of SMA braces in retrofitting reinforced concrete frames is investigated. To this end, the pseudoelastic SMA model of Stupkiewicz and Petryk [166] is incorporated into the proposed FEM procedure (see Chapter 3) and the resulting numerical tool is utilized for evaluating the effect of SMA brace on the performance of a simple RC frame. The model is also rerun using traditional steel brace and the results are compared with the results of SMA braced frame. It was demonstrated that the SMA brace can successfully reduce the residual displacements that occur during loading, as a result of the re-centring capability of such materials. The difference between the amounts of dissipated energies during loading-unloading cycle reveals the superiority of steel braced frame in absorbing the energy of the horizontal action. However, this weakness of SMA braces can be circumvented by using steel segments in SMA bracing system. In addition, as mentioned earlier, the damping capacity of the SMA braces can be increased at the time of manufacture based on the expected functionality.

Chapter 6

Final Remarks

6.1 General Conclusions

In many countries, reinforced concrete structures are traditionally constructed prior to the development of seismic design codes and are prone to severe structural damages when subjected to earthquake ground motions. In addition to social and financial losses associated with extensive earthquake damages of these structures, some of these structures represent important cultural heritages that have to be preserved. This necessitates the need for retrofitting or strengthening such structures in order to comply with modern seismic standards, thus to extend their service life.

To effectively plan the retrofitting process of existing structures, nonlinear analysis should be carried out, which allows to identify the critical zones of existing structures using distributed or lumped plasticity approaches. Having an efficient numerical tool, it is also possible to evaluate the performance and reliability of the retrofitting techniques employed.

As for the primary objective of this thesis, an original finite element tool for nonlinear analysis of reinforced concrete framed structures has been developed, based on Euler-Bernoulli hypothesis with the potential of capturing multiple slope discontinuities (plastic hinges) appearing at any position along the beam element. The developed numerical tool does not suffer from the computational difficulties arising due to plastic hinge formation, such as mesh refinement, increase of DOFs, and using higher order shape functions. In the framework of distributed plasticity, the proposed FEM model can be regarded as a model with Smart Displacement Based (SDB) beam elements with the ability of updating displacement shape functions during the nonlinear analysis.

Three numerical applications were attempted in Chapter 3 to demonstrate the efficiency of the developed numerical tool. In the first numerical example (see Section 3.5.1), the results of an experimental test were reproduced with the aim of validating the predictions of the numerical tool. In the second and third examples (see Sections 3.5.2 and 3.5.3, respectively), two special but practical cases, i.e. an RC frame with an inclined column, and a gravity-designed RC frame, respectively, were discussed in order to show that the typical response of the framed structures may be inhibited by an alternation in the geometry and steel reinforcements distribution of the structural elements.

The secondary objective of this thesis was to determine the reliability of different retrofitting techniques employed on RC frames by the use of the developed numerical tool. Two modern retrofitting techniques were considered, namely externally bonded reinforced polymer composites as additional reinforcement (see Chapter 4) and shape memory alloy braces (see Chapter 5).

For the former, the developed numerical tool was extended to account the effect of EB-FRP composites on the ultimate capacity of RC sections and consequently on the overall response of the RC frame. It was demonstrated that through this extension, the above effect is taken into consideration by the numerical tool and the results are in a good agreement with the fiber analysis results.

Two studies with different scales were conducted in Chapter 5, both using the same one-dimensional model of pseudoelasticity in SMA. First, a gradient-enhanced model of pseudoelasticity in SMAs was developed with the ability to simulate the true behaviour of SMAs, notably NiTi wire, in tension. In the second study, the application of SMA braces in RC frames was investigated. The retrofitting technique employed here consisted of strengthening a simple RC frame with one SMA brace to observe the behaviour of the retrofitted frame in loading-unloading condition. The one-dimensional pseudoelastic model of SMA was incorporated into the developed numerical tool. With this improvement of the developed numerical tool, the re-centring capability of SMA braces can be modelled and its effect on the response of RC frames under loading-unloading condition can be observed.

In overall, the presented FEM tool, although based on concentrated plasticity, is able to provide a rather good estimation of the structural response of RC frames. Its flexibility enables the user to supplement different retrofitting strategies and evaluate the effectiveness of such strategies on RC frames.

6.2 Future Developments

This thesis represents the first attempt to develop FEM numerical tool based on concentrated plasticity elements with the possibility of having multiple slope discontinuities. After the positive reply obtained from the numerical applications presented in this thesis, the numerical tool proved to be suitable to be extended to other types of damages such as those caused by shear forces, besides being completed by the inclusion of axial discontinuities.

The current numerical tool is formulated for nonlinear static analysis and in this study it only dealt with two-dimensional problems. The extension of the numerical tool to dynamic problems and three-dimensional simulations is straightforward and will be another future direction to pursue.

The incorporation of other retrofitting techniques, e.g. the use of SMA bars in RC beams, into the numerical tool or investigating more complex and special RC structures, such as industrial RC frames, could also be considered as another future applications in this area.

Last but not least, the concept of weak hinge, in which the sharp discontinuity in a point is regularized and is introduced in a finite zone in the vicinity of the plastic section of the element, offers another possible direction for future research.

Bibliography

[1] H. Ahmadian, S. H. Ardakani, and S. Mohammadi. Strain-rate sensitivity of unstable localized phase transformation phenomenon in shape memory alloys using a non-local model. *Int. J. Solids Struct.*, 63, 2015.

[2] M. S. Alam, M. A. Youssef, and M. Nehdi. Utilizing shape memory alloys to enhance the performance and safety of civil infrastructure: a review. *Can. J. Civil Eng.*, 34(9):1075–1086, 2007.

[3] B. N. Alemdar and D. W. White. Displacement, flexibility, and mixed beam–column finite element formulations for distributed plasticity analysis. *J. Struct. Eng.*, 131(12):1811–1819, 2005.

[4] A. Alhasawi, P. Heng, M. Hjiaj, S. Guezouli, and J.-M. Battini. Co-rotational planar beam element with generalized elasto-plastic hinges. *Eng. Struct.*, 151:188–205, 2017.

[5] S. Altin, Ö. Anil, and M. E. Kara. Strengthening of RC nonductile frames with RC infills: An experimental study. *Cement Concrete Comp.*, 30(7):612–621, 2008.

[6] Ö. Anil and S. Altin. An experimental study on reinforced concrete partially infilled frames. *Eng. Struct.*, 29(3):449–460, 2007.

[7] H. Aoyama and T. Sugano. A generalized inelastic analysis of reinforced concrete structures based on the tests of members. *Recent Researches of Structural Mechanics-Contributions in Honor of the 60-th Birthday of Prof. Y. Tsuboi, Uno Shoten, Tokyo, Japan*, 1968.

[8] K. M. Armattoe, C. Bouby, M. Haboussi, and T. Ben Zineb. Modeling of latent heat effects on phase transformation in shape memory alloy thin structures. *Int. J. Solids Struct.*, 88:283–295, 2016.

[9] B. Asgarian and S. Moradi. Seismic response of steel braced frames with shape memory alloy braces. *J. Constr. Steel Res.*, 67(1):65–74, 2011.

[10] M. R. Attalla, G. G. Deierlein, and W. McGuire. Spread of plasticity: quasi-plastic-hinge approach. *J. Struct. Eng.*, 120(8):2451–2473, 1994.

[11] F. Auricchio, D. Fugazza, and R. Desroches. Earthquake performance of steel frames with nitinol braces. *J. EarthQ. Eng.*, 10(spec01):45–66, 2006.

[12] F. Auricchio and E. Sacco. A one-dimensional model for superelastic shape-memory alloys with different elastic properties between austenite and martensite. *Int. J. Nonlin. Mech.*, 32(6):1101–1114, 1997.

[13] S. Bae and O. Bayrak. Plastic hinge length of reinforced concrete columns. *ACI Struct. J.*, 105(3):290, 2008.

[14] F. Bagarello. Multiplication of distributions in one dimension: possible approaches and applications to δ -function and its derivatives. *J. Math. Anal. Appl.*, 196(3):885 – 901, 1995.

[15] B. Bagheri, E. S. Firoozabad, and M. Yahyaei. Comparative study of the static and dynamic analysis of multi-storey irregular building. *International Journal of Civil, Environmental, Structural, Construction and Architectural Engineering*, 6(11):1847–1851, 2012.

[16] J.-M. Battini and C. Pacoste. Plastic instability of beam structures using co-rotational elements. *Comput. Method Appl. M.*, 191(51):5811–5831, 2002.

[17] B. Belletti, C. Damoni, and A. Gasperi. Modeling approaches suitable for pushover analyses of RC structural wall buildings. *Eng. Struct.*, 57:327–338, 2013.

[18] J. Besson, G. Cailletaud, J.-L. Chaboche, and S. Forest. *Non-linear mechanics of materials*, volume 167. Springer Science & Business Media, 2009.

[19] A. Biglari, P. Harrison, and N. Bićanić. Quasi-hinge beam element implemented within the hybrid force-based method. *Comput. Struct.*, 137:31–46, 2014.

[20] A. H. M. M. Billah and M. S. Alam. Seismic performance of concrete columns reinforced with hybrid shape memory alloy (SMA) and fiber reinforced polymer (FRP) bars. *Constr. Build. Mater.*, 28(1):730–742, 2012.

[21] B. Biondi and S. Caddemi. Closed form solutions of euler–bernoulli beams with singularities. *Int. J. Solids Struct.*, 42(9):3027–3044, 2005.

[22] B. Biondi and S. Caddemi. Euler–bernoulli beams with multiple singularities in the flexural stiffness. *Eur. J. Mech. A-Solid.*, 26(5):789–809, 2007.

[23] B. Borzi, R. Pinho, and H. Crowley. Simplified pushover-based vulnerability analysis for large-scale assessment ofRC buildings. *Eng. Struct.*, 30(3):804–820, 2008.

[24] S. N. Bousias, T. B. Panagiotakos, and M. N. Fardis. Modelling of RC members under cyclic biaxial flexure and axial force. *J. EarthQ. Eng.*, 6(02):213–238, 2002.

[25] A. Bovsunovsky and C. Surace. Non-linearities in the vibrations of elastic structures with a closing crack: a state of the art review. *Mech. Syst. Signal Pr.*, 62:129–148, 2015.

[26] J. M. Bracci, S. K. Kunnath, and A. M. Reinhorn. Seismic performance and retrofit evaluation of reinforced concrete structures. *J. Struct. Eng.*, 123(1):3–10, 1997.

[27] F. Brancaleoni, V. Ciampi, and R. Di Antonio. Rate-type models for non linear hysteretic structural behavior. In *EUROMECH colloquium*, Palermo, Italy, 1983.

[28] B. Bresler. Design criteria for reinforced columns under axial load and biaxial bending. *ACI J*, 57:481–490, 1960.

[29] G. Buda and S. Caddemi. Identification of concentrated damages in euler-bernoulli beams under static loads. *J. Eng. Mech.*, 133(8):942–956, 2007.

[30] S. Caddemi, I. Caliò, and M. Marletta. The non-linear dynamic response of the Euler–Bernoulli beam with an arbitrary number of switching cracks. *Int. J. Nonlin. Mech.*, 45(7):714–726, 2010.

[31] A. Calabrese, J. P. Almeida, and R. Pinho. Numerical issues in distributed inelasticity modeling of RC frame elements for seismic analysis. *J. Struct. Eng.*, 14(S1):38–68, 2010.

[32] G. Camata, E. Spacone, and R. Zarnic. Experimental and nonlinear finite element studies of RC beams strengthened with FRP plates. *Compos. Part B-Eng*, 38(2):277–288, 2007.

[33] G. Campione, L. Cavaleri, F. Di Trapani, G. Macaluso, and G. Scaduto. Biaxial deformation and ductility domains for engineered rectangular RC cross-sections: A parametric study highlighting the positive roles of axial load, geometry and materials. *Eng. Struct.*, 107:116–134, 2016.

[34] D. Cardone, M. Dolce, F. C. Ponzo, and E. Coelho. Experimental behaviour of R/C frames retrofitted with dissipating and re-centring braces. *J. EarthQ. Eng.*, 8(03):361–396, 2004.

[35] I. Carol and J. Murcia. Nonlinear time-dependent analysis of planar frames using an 'exact' formulation–I. Theory. *Comput. Struct.*, 33(1):79–87, 1989.

[36] I. Carol and J. Murcia. Nonlinear time-dependent analysis of planar frames using an 'exact' formulation–II. computer implementation for RC structures and examples. *Comput. Struct.*, 33(1):89–102, 1989.

[37] L. Cavaleri and F. Di Trapani. Cyclic response of masonry infilled RC frames: Experimental results and simplified modeling. *Soil Dyn. EarthQ. Eng.*, 65:224–242, 2014.

[38] M. J. Chajes, T. A. Thomson Jr, T. F. Januszka, and W. W. Finch Jr. Flexural strengthening of concrete beams using externally bonded composite materials. *Constr. Build. Mater.*, 8(3):191–201, 1994.

[39] B.-C. Chang, J. Shaw, and M. A. Iadicola. Thermodynamics of shape memory alloy wire: Modeling, experiments, and application. *Continuum Mech. Thermodyn.*, 18:83–118, 2006.

[40] J. F. Chen and J. Teng. Anchorage strength models for FRP and steel plates bonded to concrete. *J. Struct. Eng.*, 127(7):784–791, 2001.

[41] V. Ciampi and L. Carlesimo. A nonlinear beam element for seismic analysis of structures. In *8th European Conference on Earthquake Engineering*, volume 3, pages 6–3, 1986.

[42] C. Cisse, W. Zaki, and T. B. Zineb. A review of constitutive models and modeling techniques for shape memory alloys. *Int. J. Plast.*, 76:244–284, 2016.

[43] R. Clough and S. Johnston. Effect of stiffiness degradation on earthquake ductility requirments. *Transactions of Japan Earthquake Engineering Symposium, Tokyo*, pages 195–198, 1966.

[44] J. Coleman and E. Spacone. Localization issues in force-based frame elements. *J. Struct. Eng.*, 127(11):1257–1265, 2001.

[45] M. D. Davidster. Analysis of reinforced concrete columns of arbitrary geometry subjected to axial load and biaxial bending: a computer program for exact analysis. *ACI Concrete International: Design and Construction*, 8:56–61, 1986.

[46] J. C. De La Llera and A. K. Chopra. A simplified model for analysis and design of asymmetric-plan buildings. *EarthQ. Eng. Struct. Dyn.*, 24(4):573–594, 1995.

[47] R. DesRoches, J. McCormick, and M. Delemont. Cyclic properties of superelastic shape memory alloy wires and bars. *J. Struct. Eng.*, 130(1):38–46, 2004.

[48] R. DesRoches and B. Smith. Shape memory alloys in seismic resistant design and retrofit: a critical review of their potential and limitations. *J. EarthQ. Eng.*, 8(03):415–429, 2004.

[49] M. Di Ludovico, G. P. Lignola, A. Prota, and E. Cosenza. Nonlinear analysis of cross sections under axial load and biaxial bending. *ACI Struct. J.*, 107(4):390, 2010.

[50] T.-N. Doan-Ngoc, X.-L. Dang, Q.-T. Chu, R. J. Balling, and C. Ngo-Huu. Second-order plastic-hinge analysis of planar steel frames using corotational beam-column element. *J. Constr. Steel Res.*, 121:413–426, 2016.

[51] M. Dolce, D. Cardone, and R. Marnetto. Implementation and testing of passive control devices based on shape memory alloys. *EarthQ. Eng. Struct. Dyn.*, 29(7):945–968, 2000.

[52] M. Dolce, D. Cardone, F. C. Ponzo, and C. Valente. Shaking table tests on reinforced concrete frames without and with passive control systems. *EarthQ. Eng. Struct. Dyn.*, 34(14):1687–1717, 2005.

[53] J. Dong, C. S. Cai, and A. M. Okeil. Overview of potential and existing applications of shape memory alloys in bridges. *J. Bridge Eng.*, 16(2):305–315, 2010.

[54] C. Dönmez and M. A. Sözen. Numerical model for biaxial earthquake response of reinforced concrete. *Comput-Aided Civ. Inf.*, 22(4):238–253, 2007.

[55] J. F. Doyle. *Static and dynamic analysis of structures: with an emphasis on mechanics and computer matrix methods*, volume 6. Springer Science & Business Media, 2012.

[56] A. Duval, M. Haboussi, and T. Ben Zineb. Modelling of localization and propagation of phase transformation in superelastic SMA by a gradient nonlocal approach. *Int. J. Solids Struct.*, 48:1879–1893, 2011.

[57] M. T. El-Mihilmy and J. W. Tedesco. Analysis of reinforced concrete beams strengthened with FRP laminates. *J. Struct. Eng.*, 126(6):684–691, 2000.

[58] A. S. Elnashai. Advanced inelastic static (pushover) analysis for earthquake applications. *Struct. Eng. Mech.*, 12(1):51–70, 2001.

[59] I. Erdem, U. Akyuz, U. Ersoy, and G. Ozcebe. An experimental study on two different strengthening techniques for RC frames. *Eng. Struct.*, 28(13):1843–1851, 2006.

[60] A. Eslami, A. Dalalbashi, and H. R. Ronagh. On the effect of plastic hinge relocation in RC buildings using CFRP. *Compos. Part B-Eng*, 52:350–361, 2013.

[61] R. Fenwick, B. Davidson, and A. McBride. The influence of slabs on elongation in ductile seismic resistant concrete frames. In *Proceedings for NZNSEE technical conference, Rotorua, March*, pages 36–43, 1995.

[62] R. C. Fenwick and L. M. Megget. Elongation and load deflection characteristics of reinforced concrete members containing plastic hinges. *Bulletin of the New Zealand National Society for Earthquake Engineering*, 26(1):28–41, 1993.

[63] F. C. Filippou and V. V. Popov, Egor Pand Bertero. Effects of bond deterioration on hysteretic behavior of reinforced concrete joints. *Ph.D. Dissertation*, 1983.

[64] S. Forest. Nonlinear regularization operators as derived from the micromorphic approach to gradient elasticity, viscoplasticity and damage. *Proc. R. Soc. A*, 472:20150755, 2016.

[65] M. Fossetti and M. Papia. Dimensionless analysis of RC rectangular sections under axial load and biaxial bending. *Eng. Struct.*, 44:34–45, 2012.

[66] K. E. Galal and A. Ghobarah. Flexural and shear hysteretic behaviour of reinforced concrete columns with variable axial load. *Eng. Struct.*, 25(11):1353–1367, 2003.

[67] B. Gencturk, K. Hossain, and S. Lahourpour. Life cycle sustainability assessment of RC buildings in seismic regions. *Eng. Struct.*, 110:347–362, 2016.

[68] M. F. Giberson. *The response of nonlinear multi-story structures subjected to earthquake excitation.* PhD thesis, California Institute of Technology, 1967.

[69] J. F. Hajjar and B. C. Gourley. A cyclic nonlinear model for concrete-filled tubes. I: Formulation. *J. Struct. Eng.*, 123(6):736–744, 1997.

[70] J. F. Hajjar, B. C. Gourley, and M. C. Olson. A cyclic nonlinear model for concrete-filled tubes. II: Verification. *J. Struct. Eng.*, 123(6):745–754, 1997.

[71] J. F. Hallai and S. Kyriakides. Underlying material response for Lüders-like instabilities. *Int. J. Plast.*, 47:1–12, 2013.

[72] Y. L. Han, Q. S. Li, A. Q. Li, A. Y. T. Leung, and P. H. Lin. Structural vibration control by shape memory alloy damper. *EarthQ. Eng. Struct. Dyn.*, 32(3):483–494, 2003.

[73] S. I. Hilmy and J. F. Abel. Material and geometric nonlinear dynamic analysis of steel frames using computer graphics. *Comput. Struct.*, 21(4):825–840, 1985.

[74] Indian Standard Code of Practice for Plain and Reinforced Concrete. *Bureau of Indian Standards, New Delhi*, IS:456-2000.

[75] Italian Building Code. Norme Tecniche per le Costruzioni. *Gazzetta Ufficiale della Republica Italiana, Rome*, 2008.

[76] Italian Guideline CNR-DT 200 R1. Guide for the Design and Construction of Externally Bonded FRP Systems for Strengthening Existing Structures–National Research Council of Italy. *Advisory Committee on Technical Regulations for Constructions, Rome*, 2013.

[77] C. K. Iu. Inelastic finite element analysis of composite beams on the basis of the plastic hinge approach. *Eng. Struct.*, 30(10):2912–2922, 2008.

[78] B. A. Izzuddin and A. S. Elnashai. Adaptive space frame analysis: part II, a distributed plasticity approach. *P. I. Civil Eng-Str. B.*, 99(3):317–3326.

[79] B. A. Izzuddin and A. S. Elnashai. Adaptive space frame analysis: part I, a plastic hinge approach. *P. I. Civil Eng-Str. B.*, 99(3):303–316, 1993.

[80] B. A. Izzuddin and A. S. Elnashai. Eulerian formulation for large-displacement analysis of space frames. *J. Eng. Mech.*, 119(3):549–569, 1993.

[81] B. A. Izzuddin, C. G. Karayannis, and A. S. Elnashai. Advanced nonlinear formulation for reinforced concrete beam-columns. *J. Struct. Eng.*, 120(10):2913–2934, 1994.

[82] B. A. Izzuddin, A. A. F. M. Siyam, and D. L. Smith. An efficient beam–column formulation for 3D reinforced concrete frames. *Comput. Struct.*, 80(7):659–676, 2002.

[83] L. Janke, C. Czaderski, M. Motavalli, and J. Ruth. Applications of shape memory alloys in civil engineering structures - overview, limits and new ideas. *Mater. Struct.*, 38(5):578–592, 2005.

[84] D. Kachlakev and D. McCurry. Behavior of full-scale reinforced concrete beams retrofitted for shear and flexural with FRP laminates. *Compos. Part B-Eng*, 31(6):445–452, 2000.

[85] C. G. Karayannis, B. A. Izzuddin, and A. S. Elnashai. Application of adaptive analysis to reinforced concrete frames. *J. Struct. Eng.*, 120(10):2935–2957, 1994.

[86] D. C. Kent and R. Park. Flexural members with confined concrete. *J. Struct. Div-ASCE*, 1971.

[87] K. D. Kim and M. D. Engelhardt. Beam-column element for nonlinear seismic analysis of steel frames. *J. Struct. Eng.*, 126(8):916–925, 2000.

[88] S.-E. Kim, M.-K. Kim, and W.-F. Chen. Improved refined plastic hinge analysis accounting for strain reversal. *Eng. Struct.*, 22(1):15–25, 2000.

[89] J. Korelc. Automation of primal and sensitivity analysis of transient coupled problems. *Comput. Mech.*, 44:631–649, 2009.

[90] J. Korelc and P. Wriggers. *Automation of finite element methods*. Springer International Publishing, Switzerland, 2016.

[91] H. Krawinkler and G. P. K. Seneviratna. Pros and cons of a pushover analysis of seismic performance evaluation. *Eng. Struct.*, 20(4-6):452–464, 1998.

[92] S. Krishnan and J. F. Hall. Modeling steel frame buildings in three dimensions. I: Panel zone and plastic hinge beam elements. *J. Eng. Mech.*, 132(4):345–358, 2006.

[93] S. Krishnan and J. F. Hall. Modeling steel frame buildings in three dimensions. II: Elastofiber beam element and examples. *J. Eng. Mech.*, 132(4):359–374, 2006.

[94] H.-G. Kwak and J.-H. Kwak. An improved design formula for a biaxially loaded slender RC column. *Eng. Struct.*, 32(1):226–237, 2010.

[95] D. C. Lagoudas, P. B. Entchev, P. Popov, E. Patoor, L. C. Brinson, and X. Gao. Shape memory alloys, Part II: Modeling of polycrystals. *Mech. Mater.*, 38:430–462, 2006.

[96] S.-S. Lai, G. T. Will, and S. Otani. Model for inelastic biaxial bending of concrete members. *J. Struct. Eng.*, 110(11):2563–2584, 1984.

[97] A. Landesmann. Plastic-hinge approach for inelastic analysis of steel–concrete framed structures. *J. Constr. Steel Res.*, 66(3):323–334, 2010.

[98] C. Y. Lau, S. L. Chan, and A. K. W. So. Biaxial bending design of arbitrarily shaped reinforced concrete column. *Struct. J.*, 90(3):269–278, 1993.

[99] K. Le Nguyen, M. Brun, A. Limam, E. Ferrier, and L. Michel. Pushover experiment and numerical analyses on CFRP-retrofit concrete shear walls with different aspect ratios. *Compos. Struct.*, 113:403–418, 2014.

[100] J.-Y. Lee and F. Watanabe. Predicting the longitudinal axial strain in the plastic hinge regions of reinforced concrete beams subjected to reversed cyclic loading. *Eng. Struct.*, 25(7):927–939, 2003.

[101] J. Lemaitre and J.-L. Chaboche. *Mechanics of solid materials*. Cambridge university press, 1994.

[102] A. A. León Baldelli, C. Maurini, and K. Pham. A gradient approach for the macroscopic modeling of superelasticity in softening shape memory alloys. *Int. J. Solids Struct.*, 52:45–55, 2015.

[103] L.-J. Leu and J.-C. Cheng. Flexibility based formulation for nonlinear analysis of reinforced concrete frames considering the effects of finite length inelastic zones. *J. Chin. Inst. Eng.*, 23(1):97–108, 2000.

[104] L.-J. Leu and C.-H. Tsou. Second-order analysis of planar steel frames considering the effect of spread of plasticity. *Struct. Eng. Mech.*, 11(4):423–442, 2001.

[105] L.-J. Leu, J. P. Yang, M.-H. Tsai, and Y.-B. Yang. Explicit inelastic stiffness for beam elements with uniform and nonuniform cross sections. *J. Struct. Eng.*, 134(4):608–618, 2008.

[106] S. Li, Z. Zuo, C. Zhai, and L. Xie. Comparison of static pushover and dynamic analyses using RC building shaking table experiment. *Eng. Struct.*, 136:430–440, 2017.

[107] J. Y. R. Liew, H. Chen, N. E. Shanmugam, and W. F. Chen. Improved nonlinear plastic hinge analysis of space frame structures. *Eng. Struct.*, 22(10):1324–1338, 2000.

[108] J. Y. R. Liew, D. W. White, and W. Chen. Second-order refined plastic-hinge analysis for frame design. part II. *J. Struct. Eng.*, 119(11):3217–3236, 1993.

[109] J. Y. R. Liew, D. W. White, and W.-F. Chen. Second-order refined plastic-hinge analysis for frame design. part I. *J. Struct. Eng.*, 119(11):3196–3216, 1993.

[110] S.-W. Liu, Y.-P. Liu, and S.-L. Chan. Direct analysis by an arbitrarily-located-plastic-hinge element–part 1: Planar analysis. *J. Constr. Steel Res.*, 103:303–315, 2014.

[111] Y.-S. Liu and G.-Q. Li. A nonlinear analysis method of steel frames using element with internal plastic hinges. *Adv. Steel Constr.*, 4(4):341–352, 2008.

[112] M. R. Maheri, S. S. Mahini, and S. A. Hadighe. Seismic assessment of FRP-retrofitted RC frames using pushover analysis considering strain softening of concrete. In *Advances in FRP Composites in Civil Engineering: Proceedings of the 5th International Conference on FRP Composites in Civil Engineering (CICE 2010), Sep 27–29, 2010, Beijing, China*, pages 841–844. Springer Berlin Heidelberg, 2011.

[113] S. Mahini and H. Ronagh. A new method for improving ductility in existing RC ordinary moment resisting frames using FRPs. *Asian Journal of Civil Engineering (Building and Housing)*, 8(6):581–595, 2007.

[114] S. S. Mahini and H. R. Ronagh. Strength and ductility of FRP web-bonded RC beams for the assessment of retrofitted beam–column joints. *Compos. Struct.*, 92(6):1325–1332, 2010.

[115] J. Matthews, J. Mander, and D. Bull. Prediction of beam elongation in structural concrete members using a rainflow method. In *New Zealand Society of Earthquake Engineering Conference*, 2004.

[116] R. Mayo, A. Nanni, W. Gold, and M. Barker. Strengthening of bridge G270 with externally-bonded CFRP reinforcement. In *SP-188, American Concrete Institute, Proc., 4th International Symposium on FRP for Reinforcement of Concrete Structures (FRPRCS4), Baltimore, MD, Nov*, pages 429–440, 1999.

[117] M. Mazière and S. Forest. Strain gradient plasticity modeling and finite element simulation of Lüders band formation and propagation. *Continuum Mech. Thermodyn.*, 27:83–104, 2015.

[118] F. Mazza. A distributed plasticity model to simulate the biaxial behaviour in the nonlinear analysis of spatial framed structures. *Comput. Struct.*, 135:141–154, 2014.

[119] S. Mazzoni, F. McKenna, M. H. Scott, G. L. Fenves, et al. Opensees command language manual. *Pacific Earthquake Engineering Research (PEER) Center*, 2006.

[120] J. McCormick, R. DesRoches, D. Fugazza, and F. Auricchio. Seismic vibration control using superelastic shape memory alloys. *J. Eng. Mater-T. ASME*, 128(3):294–301, 2006.

[121] J. McCormick, R. DesRoches, D. Fugazza, and F. Auricchio. Seismic assessment of concentrically braced steel frames with shape memory alloy braces. *J. Struct. Eng.*, 133(6):862–870, 2007.

[122] U. Meier. Strengthening of structures using carbon fibre/epoxy composites. *Constr. Build. Mater.*, 9(6):341–351, 1995.

[123] M. Menegotto and P. Pinto. Method of analysis for cyclically loaded rc frames including changes in geometry and non-elastic behaviour of elements under combined normal force and bending. In *IABSE Congress Reports of the Working Commission*, volume 13, 1973.

[124] C. Meyer, M. S. Roufaiel, and S. G. Arzoumanidis. Analysis of damaged concrete frames for cyclic loads. *EarthQ. Eng. Struct. Dyn.*, 11(2):207–228, 1983.

[125] O. A. Mohamed and R. Khattab. Bond-slip modelling of FRP sheets externally bonded to concrete beam. *Procedia Engineer.*, 161:833–838, 2016.

[126] M. G. Mullas and F. C. Filippou. Analytical procedures in the study of seismic response of reinforced concrete frames. *Eng. Struct.*, 12(1):37–48, 1990.

[127] A. M. Mwafy and A. S. Elnashai. Static pushover versus dynamic collapse analysis of RC buildings. *Eng. Struct.*, 23(5):407–424, 2001.

[128] A. Neuenhofer and F. Filippou. Evaluation of nonlinear frame finite-element models. *J. Struct. Eng.*, 123(7):958–966, 1997.

[129] A. Niroomandi, A. Maheri, M. R. Maheri, and S. Mahini. Seismic performance of ordinary RC frames retrofitted at joints by FRP sheets. *Eng. Struct.*, 32(8):2326–2336, 2010.

[130] K. Ohi. Pseudo-dynamic earthquake response tests and cyclic loading tests on steel frames including pseudo-elastic elements. In *Proc., NSF–JSPS, US–Japan Seminar on Advanced Stability and Seismicity Concepts for Performance-Based Design of Steel and Composite Structures*, 2001.

[131] L. Ombres. Flexural analysis of reinforced concrete beams strengthened with a cement based high strength composite material. *Compos. Struct.*, 94(1):143–155, 2011.

[132] S. Otani. Inelastic analysis of R/C frame structures. *J. Struct. Div-ASCE*, 100(Proc. Paper 10686), 1974.

[133] K. Otsuka and C. M. Wayman. *Shape Memory Materials*. Cambridge University Press, Cambridge, 1999.

[134] B. Pantò, D. Rapicavoli, S. Caddemi, and I. Caliò. A smart displacement based (SDB) beam element with distributed plasticity. *Appl. Math. Model.*, 44:336–356, 2017.

[135] R. Park and T. Paulay. *Reinforced concrete structures*. John Wiley & Sons, 1975.

[136] E. Patoor, D. C. Lagoudas, P. B. Entchev, L. C. Brinson, and X. Gao. Shape memory alloys, Part I: General properties and modeling of single crystals. *Mech. Mater.*, 38:391–429, 2006.

[137] G. Paul and P. Agarwal. Experimental verification of seismic evaluation of RC frame building designed as per previous is codes before and after retrofitting by using steel bracing. *Asian Journal of Civil Engineering (Building and Housing)*, 13(2):165–179, 2012.

[138] T. Paulay and M. N. Priestley. Seismic design of reinforced concrete and masonry buildings. 1992.

[139] A. Pecker. *Advanced earthquake engineering analysis*. Springer, Udine, 2007.

[140] R. H. J. Peerlings, R. de Borst, W. A. M. Brekelmans, and J. H. P. de Vree. Gradient enhanced damage for quasi-brittle materials. *Int. J. Numer. Meth. Eng.*, 39:3391–3403, 1996.

[141] M. Petrangeli, P. E. Pinto, and V. Ciampi. Fiber element for cyclic bending and shear of rc structures. 0i: Theory. *J. Eng. Mech.*, 125(9):994–1001, 1999.

[142] H. Petryk. Incremental energy minimization in dissipative solids. *Compt. Rendus. Mec.*, 331:469–474, 2003.

[143] G. H. Powell and P. F.-S. Chen. 3D beam-column element with generalized plastic hinges. *J. Struct. Eng.*, 112(7):627–641, 1986.

[144] C. P. Providakis. Pushover analysis of base-isolated steel–concrete composite structures under near-fault excitations. *Soil Dyn. EarthQ. Eng.*, 28(4):293–304, 2008.

[145] M. Y. Rafiq and C. Southcombe. Genetic algorithms in optimal design and detailing of reinforced concrete biaxial columns supported by a declarative approach for capacity checking. *Comput. Struct.*, 69(4):443–457, 1998.

[146] B. Raniecki, C. Lexcellent, and K. Tanaka. Thermodynamic models of pseudoelastic behaviour of shape memory alloys. *Arch. Mech.*, 44:261–284, 1992.

[147] M. Rezaee Hajidehi, A. Spada, and G. Giambanco. The multiple slope discontinuity beam element for nonlinear analysis of rc framed structures. *Meccanica*, 2018.

[148] M. Rezaee Hajidehi and S. Stupkiewicz. Gradient-enhanced model and its micromorphic regularization for simulation of Lüders-like bands in shape memory alloys. *Int. J. Solids. Struct.*, 2017.

[149] R. T. Rockafellar. *Convex Analysis*. Princeton University Press, Princeton, New Jersey, 1970.

[150] H. Rodrigues, A. Arêde, H. Varum, and A. Costa. Damage evolution in reinforced concrete columns subjected to biaxial loading. *B. EarthQ. Eng.*, 11(5):1517–1540, 2013.

[151] X. Romão, A. Costa, and R. Delgado. New model for the inelastic biaxial bending of reinforced concrete columns. In *13th World Conference on Earthquake Engineering*, 2004.

[152] H. R. Ronagh and A. Eslami. Flexural retrofitting of RC buildings using GFRP/CFRP–A comparative study. *Compos. Part B-Eng*, 46:188–196, 2013.

[153] L. Rosati, F. Marmo, and R. Serpieri. Enhanced solution strategies for the ultimate strength analysis of composite steel–concrete sections subject to axial force and biaxial bending. *Comput. Method Appl. M.*, 197(9):1033–1055, 2008.

[154] H. A. Safarizki, S. A. Kristiawan, and A. Basuki. Evaluation of the use of steel bracing to improve seismic performance of reinforced concrete building. *Procedia Engineer.*, 54:447–456, 2013.

[155] P. Sedmák, J. Pilch, L. Heller, J. Kopeček, J. Wright, P. Sedlák, M. Frost, and P. Šittner. Grain-resolved analysis of localized deformation in nickel-titanium wire under tensile load. *Science*, 353:559–562, 2016.

[156] M. G. Sfakianakis. Biaxial bending with axial force of reinforced, composite and repaired concrete sections of arbitrary shape by fiber model and computer graphics. *Adv. Eng. Softw.*, 33(4):227–242, 2002.

[157] J. A. Shaw and S. Kyriakides. On the nucleation and propagation of phase transformation fronts in a NiTi alloy. *Acta. Mater.*, 45:683–700, 1997.

[158] S. A. Sheikh and S. S. Khoury. Confined concrete columns with stubs. *ACI Struct. J.*, 90:414–414, 1993.

[159] J. C. Simo and R. L. Taylor. Consistent tangent operators for rate-independent elastoplasticity. *Comput. Method Appl. M.*, 48(1):101–118, 1985.

[160] P. Sittner, Y. Liu, and V. Novák. On the origin of Lüders-like deformation of NiTi shape memory alloys. *Int. J. Solids Struct.*, 53:1719–1746, 2005.

[161] D. Soleimani, E. P. Popov, and V. V. Bertero. Nonlinear beam model for R/C frame analysis. In *Electronic computation*, pages 483–509. ASCE, 1979.

[162] G. Song, N. Ma, and H. N. Li. Applications of shape memory alloys in civil structures. *Eng. Struct.*, 28(9):1266–1274, 2006.

[163] E. Spacone, V. Ciampi, and F. C. Filippou. Mixed formulation of nonlinear beam finite element. *Comput. Struct.*, 58(1):71–83, 1996.

[164] E. Spacone, F. C. Filippou, and F. F. Taucer. Fibre beam-column model for non-linear analysis of R/C frames: Part I. Formulation. *EarthQ. Eng. Struct. Dyn.*, 25(7):711–726, 1996.

[165] S. Stupkiewicz. *Micromechanics of contact and interphase layers*, volume 30. Springer Science & Business Media, 2007.

[166] S. Stupkiewicz and H. Petryk. A robust model of pseudoelasticity in shape memory alloys. *Int. J. Numer. Meth. Eng.*, 93:747–769, 2013.

[167] F. Sutcu, T. Takeuchi, and R. Matsui. Seismic retrofit design method for RC buildings using buckling-restrained braces and steel frames. *J. Constr. Steel Res.*, 101:304–313, 2014.

[168] T. Takeda, M. A. Sozen, and N. N. Nielsen. Reinforced concrete response to simulated earthquakes. *Journal of the Structural Division. Proceeding to the American Society of Civil Enginerrs*, 96(12):2557–2573, 1970.

[169] H. Takizawa. Non-linear models for simulating the dynamic damaging process of low-rise reinforced concrete buildings during severe earthquakes. *EarthQ. Eng. Struct. Dyn.*, 4(1):73–94, 1975.

[170] H. TAKIZAWA. Notes on some basic problems in inelastic analysis of planar R/C structures (part i). *Transactions of the Architectural Institute of Japan*, 240:51–62, 1976.

[171] H. Tamai and Y. Kitagawa. Pseudoelastic behavior of shape memory alloy wire and its application to seismic resistance member for building. *Comp. Mater. Sci.*, 25(1):218–227, 2002.

[172] F. F. Taucer, E. Spacone, and F. C. Filippou. *A fiber beam-column element for seismic response analysis of reinforced concrete structures*, volume 91. Earthquake Engineering Research Center, College of Engineering, University of California Berkekey, California, 1991.

[173] M. Tazarv and M. S. Saiidi. Reinforcing NiTi superelastic SMA for concrete structures. *J. Struct. Eng.*, 141(8):04014197, 2014.

[174] Y. Ueda, S. M. H. Rashed, and K. Nakacho. New efficient and accurate method of nonlinear analysis of offshore tubular frames (the idealized structural unit method). *J. Energ. Resour-ASME*, 107(2):204–211, 1985.

[175] V. Van Cao and H. R. Ronagh. Reducing the seismic damage of reinforced concrete frames using FRP confinement. *Compos. Struct.*, 118:403–415, 2014.

[176] D. W. White. Plastic-hinge methods for advanced analysis of steel frames. *J. Constr. Steel Res.*, 24(2):121–152, 1993.

[177] E. L. Wilson. *Three-dimensional static and dynamic analysis of structures*. Computers and structures, 2002.

[178] C. A. Zeris and S. A. Mahin. Analysis of reinforced concrete beam-columns under uniaxial excitation. *J. Struct. Eng.*, 114(4):804–820, 1988.

[179] X. Zhang, P. Feng, Y. He, T. Yu, and Q. P. Sun. Experimental study on rate dependence of macroscopic domain and stress hysteresis in NiTi shape memory alloy strips. *Int. J. Mech. Sci.*, 52:1660–1670, 2010.

[180] X.-M. Zhao, Y.-F. Wu, and A. Y. T. Leung. Analyses of plastic hinge regions in reinforced concrete beams under monotonic loading. *Eng. Struct.*, 34:466–482, 2012.

[181] S. Zhu and Y. Zhang. Seismic behaviour of self-centring braced frame buildings with reusable hysteretic damping brace. *EarthQ. Eng. Struct. Dyn.*, 36(10):1329–1346, 2007.

[182] O. C. Zienkiewicz and R. L. Taylor. *The Finite Element Method: Solid Mechanics, 2, 5th edition*. Butterworth-Heinemann, Oxford, UK, 2000.

[183] O. C. Zienkiewicz and R. L. Taylor. *The Finite Element Method: The Basis, vol. 2, 5th edition*. Butterworth-Heinemann, Oxford, UK, 2000.

[184] X. Zou, J.-G. Teng, L. De Lorenzis, and S. Xia. Optimal performance-based design of FRP jackets for seismic retrofit of reinforced concrete frames. *Compos. Part B-Eng*, 38(5):584–597, 2007.

[185] A. H. Zubydan and A. I. ElSabbagh. Monotonic and cyclic behavior of concrete-filled steel-tube beam-columns considering local buckling effect. *Thin Wall. Struct.*, 49(4):465–481, 2011.

Acknowledgements

I started my Ph.D. in January 2015 at the department of DICAM (il Dipartimento di Ingegneria Civile, Ambientale, Aerospaziale, dei Materiali) of university of Palermo. Now, almost three years have passed in the blink of an eye and aside from many new things that I have learned, this period have taught me that good intentions are worth nothing without persistence. Although, a Ph.D dissertation is an individual activity, I could not have achieved it without the help, inspiration, contribution and encouragements of many people who have crossed my path.

First of all, I would like to appreciate my supervisors, Prof. Giuseppe Giambanco and Prof. Stanislaw Stupkiewicz for their constant guidance and unconditional supports during my stay in Palermo and Warsaw, without which the completion of this work would not have been possible.

I wish to express my sincerest gratitude to Dr. Antonino Spada and Dr. Giovanni Minafò for their technical discussions and assistance, which have aided me a lot to improve the quality if this thesis, ans also being great friends.

I would like to use this opportunity to thank all my colleagues and friends at the university of Palermo, who have made my three years of stay unforgettable, especially: Giuseppe, Francesco, Emma, Pietro, Gioacchino, Natalia, Gabriele, Marco, Francesco, Salvatore, Alberto and Majid. Another special thanks go to my Iranian friends in Palermo for their friendship and solidarity, without them my adaptation would have been much more difficult, especially: Mansour, Arash, Masoud, Saeed, Mahafarin, Hooman, Reza and Maryam.

Most importantly, I extend my gratitude to my family for their continuous love and support without any complaint or regret, which enabled me to survive this challenge.

Mohsen Rezaee Hajidehi,
Palermo, 20/12/2017